

Copyright

by

Krishna Vikas Gudipati

2009

**The Dissertation Committee for Krishna Vikas Gudipati Certifies that this is the  
approved version of the following dissertation:**

**Deformation Monitoring using Scanning Synthetic Aperture Radar  
Interferometry**

**Committee:**

---

Sean M. Buckley, Supervisor

---

Byron D. Tapley

---

Bob E. Schutz

---

Clark R. Wilson

---

Howard A. Zebker

**Deformation Monitoring using Scanning Synthetic Aperture Radar  
Interferometry**

**by**

**Krishna Vikas Gudipati, B. Tech.; M. S.**

**Dissertation**

Presented to the Faculty of the Graduate School of

The University of Texas at Austin

in Partial Fulfillment

of the Requirements

for the Degree of

**Doctor of Philosophy**

**The University of Texas at Austin**

**May 2009**

## **Dedication**

To my lovely wife, Akansha  
who has provided caring and steady support

To my parents, Shantaram and Nagasree, and sister, Jyotsna  
who inspired a strong interest towards science

and

To the memory of my grandmother, Rambai amma  
without whose blessings it would not have been possible



## **Acknowledgements**

I express my most sincere gratitude to my supervisor, Dr. Sean Buckley, who has patiently guided me through the entire course of my Ph.D. My interest in radar interferometry was inspired by a seminar he presented at CSR while I was working on my master's degree. I am grateful to him for showing faith in me and accepting me as his first graduate student. I am fortunate that I made the right decision in choosing to work with him. I thoroughly enjoyed the countless open discussions we had on various topics of radar interferometry research; he was very supportive in my pursuance of ScanSAR interferometry research and gave me a nudge in the right direction wherever I needed guidance. Also, I have enjoyed the numerous informal talks I had with him concerning the culture and traditions of India and the U.S. Dr. Buckley: I appreciate your patience and your willingness to go that extra mile to know your students well.

I express thanks to Dr. Clark Wilson, my committee member and professor at the Jackson School of Geosciences, under whose guidance I completed my master's degree. Dr. Wilson, along with Dr. Fred Taylor from the Institute for Geophysics, was instrumental in constructively shaping the early stages of my graduate schooling. My field trip to Antarctica with Dr. Taylor and Dr. Cliff Frohlich where we conducted GPS surveys to measure crustal deformations was an eye-opener to the marvels of the planet we live on. I thank Dr. Wilson for introducing me to Dr. Buckley and for initiating me into the field of radar remote sensing.

A very special thanks to my friend and fellow graduate student Dochul Yang, for without his collaboration I would not have been able to complete this research in a timely manner. I shared the majority of my time as graduate student with Dochul, and I have had innumerable discussions on various research related issues with him. I am extremely grateful to him for sharing the SBAS computer code he wrote with me. Also, we worked collaboratively in developing the code for PS analysis. It was a pleasure having him as a colleague, and I will always value his friendship.

I express my gratitude to all my committee members for their valuable comments and suggestions. Thanks to Dr. Howard Zebker, professor at Stanford University, for his willingness to serve on my committee. I would like to thank Dr. Riccardo Lanari, senior researcher at the Institute for Electromagnetic Sensing of the Environment (IREA) in Italy, for providing a brief but vital assistance in helping me write the computer code for the modified SPECAN algorithm. Also, I would like to express thanks to all the faculty and staff of the Department of Aerospace Engineering who have contributed to my learning.

Thanks to all my extended family members who have made my stay in the U.S. a pleasure. I would like to thank my cousins and their spouses: Vasannaya and Jaya, Kalyan and Gayatri, Vinay and Sameera. A special thanks to a special cousin, Venu, who never grew tired of hosting me while I made those countless trips to Dallas. Thanks Kalyan and Venu for teaching me the game of tennis and getting me hooked on American football. Although I was far away from home, you guys never let me feel that way. Thanks for being such a wonderful family and for your support. I will be forever indebted to you.

Thanks also to my friends in Austin: Ganesh, Rawoof, Saurabh, Naveen, Aswini, Nivedita, Srikanth S., Sneha, Shalu, and Ankur for sharing many wonderful moments

over the course of past few years. I am particularly grateful to Naveen and Rawoof for being the best of the friends and for providing moral and emotional support. Also, I am thankful to Jenny and Katie for helping me correct the English in my dissertation.

Finally, I express my most devout gratitude to my parents and wife Akansha. Thank you Daddy and amma: for being ever-so-patient with me for the past eight years during my graduate school. I owe you everything for motivating me to do what I wanted to do and for making me realize the importance of education. Akansha: I am really grateful that you came into my life. I deeply appreciate the love and the caring support that you provided when I needed it the most.

# **Deformation Monitoring using Scanning Synthetic Aperture Radar Interferometry**

Publication No. \_\_\_\_\_

Krishna Vikas Gudipati, Ph. D.

The University of Texas at Austin, 2009

Supervisor: Sean M. Buckley

This dissertation provides the first demonstration of scanning synthetic aperture radar (ScanSAR) advanced interferometry processing for measuring surface deformation. ScanSAR data are synthesized from ERS-1/2 stripmap SAR images over known deformation in Phoenix, Arizona. The strategy is to construct a burst pattern similar to Envisat ScanSAR data and to create a realistic variable-burst synchronization scenario in which any image pair has at least 50% burst overlap.

The Small Baseline Subsets technique is applied to the synthesized data to demonstrate ScanSAR time series analysis for a scenario generally conducive for interferometry. The same processing approach is employed with the stripmap data to validate the results. The differences in ScanSAR and stripmap velocities have a mean and standard deviation of  $0.02 \pm 0.02$  cm/year. 96.3% and 99.1% of the velocity differences are within  $\pm 0.1$  cm/year and  $\pm 0.2$  cm/year, respectively. The RMS deviations between the

ScanSAR and stripmap displacement estimates are  $0.40 \pm 0.30$  cm. 68.5% and 94.6% of the differences are within  $\pm 0.5$  cm and  $\pm 1.0$  cm, respectively.

The Permanent Scatterer (PS) technique also is adapted and applied to the synthesized data to demonstrate the presence of PS in ScanSAR data. The atmospheric and nonlinear motion phase derived from a PS analysis of stripmap data are removed from the ScanSAR interferograms. Even for this idealized scenario, the final PS identification yields fewer ScanSAR PS ( $10 \text{ PS/km}^2$ ) than the stripmap PS results ( $312 \text{ PS/km}^2$  or  $15.6 \text{ PS/km}^2$  at the ScanSAR pixel resolution). Based on the calculated likelihood of finding multiple stripmap PS within a ScanSAR pixel, it is concluded that the ScanSAR single scatterer PS model is flawed.

A model is introduced that considers multiple PS within a ScanSAR pixel. The search for two PS per pixel yields  $120 \text{ PS/km}^2$ . The ScanSAR and stripmap PS velocity differences mean is zero and standard deviation is 0.02 cm/year. However, while the differences between the ScanSAR and stripmap PS DEM error estimates are zero-mean, they have a 7-meter standard deviation. One possible explanation for this relatively large deviation is the differencing of the wrong ScanSAR and stripmap PS as the result of a misalignment between the ScanSAR and stripmap images.

## Table of Contents

List of Tables .....	xiii
List of Figures .....	xiv
<b>CHAPTER ONE</b>	<b>1</b>
INTRODUCTION .....	1
1.1 BACKGROUND .....	1
1.2 MOTIVATION .....	3
1.3 OBJECTIVES .....	9
1.4 APPROACH .....	9
1.5 CONTRIBUTIONS .....	11
1.6 OUTLINE .....	13
<b>CHAPTER TWO</b>	<b>15</b>
BACKGROUND .....	15
2.1 SYNTHETIC APERTURE RADAR.....	15
2.2 SYNTHETIC APERTURE RADAR INTERFEROMETRY.....	33
2.3 SUMMARY .....	44
<b>CHAPTER THREE</b>	<b>45</b>
SCANSAR IMAGING AND BURST MODE DATA PROCESSING .....	45
3.1 BURST MODE AND SCANSAR MODE DATA.....	45
3.2 BURST MODE DATA SIGNAL PROPERTIES .....	52
3.3 BURST MODE DATA PROCESSING .....	59
3.4 SUMMARY .....	72

## **CHAPTER FOUR**

**73**

DIFFERENTIAL INTERFEROMETRY AND DEFORMATION TIME SERIES GENERATION USING SCANSAR DATA.....	73
4.1 BACKGROUND ON SCANSAR INTERFEROMETRY .....	74
4.2 EFFECT OF BURST OVERLAP ON PHASE COHERENCE .....	77
4.3 INSAR AND SBAS ANALYSIS USING SCANSAR DATA .....	96
4.4 DEFORMATION TIME SERIES RESULTS AND VALIDATION.....	109
4.5 CONCLUSIONS.....	116

## **CHAPTER FIVE**

**118**

PERSISTENT SCATTERER ANALYSIS USING SCANSAR DATA.....	118
5.1 BACKGROUND .....	118
5.2 ADAPTED PERMANENT SCATTERER TECHNIQUE APPLIED TO STRIPMAP DATA.....	122
5.3 ADAPTED PERMANENT SCATTERER TECHNIQUE AND SINGLE SCATTERER MODEL APPLIED TO SCANSAR DATA .....	139
5.4 ADAPTED PERMANENT SCATTERER TECHNIQUE AND MULTIPLE SCATTERER MODEL APPLIED TO SCANSAR DATA .....	144
5.5 CONCLUSIONS.....	172

## **CHAPTER SIX**

**174**

CONCLUSIONS AND FUTURE WORK.....	174
6.1 CONCLUSIONS.....	174
6.2 TOPICS FOR FUTURE WORK .....	178

<b>APPENDIX A</b>	<b>182</b>
Chirp-Z Transform.....	182
<b>APPENDIX B</b>	<b>185</b>
List of SAR Data and Interferograms Used.....	185
<b>REFERENCES</b>	<b>190</b>
<b>VITA</b>	<b>197</b>



## **List of Tables**

Table 1.1:	Envisat ASAR Phoenix image dates for one orbit exact repeat cycle. ....	6
Table 3.1:	Burst parameters for various subswaths of Envisat WSM (compared to Envisat and ERS stripmap modes).....	52
Table B.1:	SAR images used for SBAS and PS InSAR time series techniques.....	185
Table B.2:	Interferograms formed as part of the SBAS time series analysis. ....	186

## List of Figures

Figure 1.1: Envisat ASAR coverage over Phoenix, Arizona from adjacent descending orbit tracks for a 35-day period between 11 May 2009 and 15 June 2009. The stripmap coverage is shown in red and the ScanSAR coverage is shown in blue. ....	7
Figure 2.1: A squinted SAR imaging geometry. ....	17
Figure 2.2: Flowchart describing the basic steps of the Range-Doppler algorithm. ....	20
Figure 2.3: A sketch of the variation of slant range and squint angle to a target as it is imaged through time.....	24
Figure 2.4: A 2-D projection of the slant range plane onto the vertical plane defined by azimuth and height (Adapted from Cumming and Wong [2005]). (A) Relative position of the target within the radar beam as the satellite travels from left to right. (B) Variation in the received signal strength with azimuth. (C) Linear variation of Doppler frequency in azimuth. ....	25
Figure 2.5: A 2-D sketch describing interferometry geometry. Satellites at positions $S_{p1}$ and $S_{p2}$ are assumed to be flying into the page, imaging to their right. Points $S_{p1}$ , $S_{p2}$ , $P_{RS}$ , and $P_0$ are all in the same plane. ....	35
Figure 3.1: A ScanSAR data acquisition scheme. The SAR sensor images 5 subswaths, returning to the same subswath after one burst cycle duration. Parameters such as the burst duration, the inter-burst gap, and the subswath width, can vary from one subswath to another. ....	47
Figure 3.2: A comparison of stripmap and burst mode imaging geometry, azimuth signal strength, and Doppler history for a single target. ....	50

Figure 3.3: Block diagram of the SPECAN algorithm (Adapted from Cumming and Wong [2005]).....	61
Figure 3.4: A sketch showing 2-D projection of sensor-target imaging geometry for a single burst. The shaded area indicates the set of satellite to target lines of sight projected into the vertical plane containing the satellite track.....	63
Figure 3.5: Block diagram of the Modified SPECAN algorithm (adapted from Lanari et al. [1998]). .....	67
Figure 4.1: Repeat-pass imaging geometry in burst mode SAR. (B) Burst Doppler response of a target relative to the full-aperture Doppler bandwidth. ....	75
Figure 4.2: InSAR phase map obtained from a stripmap interferogram spanning the time between March 15, 1999 and December 20, 1999. The figure shown bounds the land subsidence features in the cities of Peoria and Glendale in the Phoenix metropolitan area. The perpendicular baseline is 150 meters.....	80
Figure 4.3: ScanSAR InSAR phase maps for various burst overlap cases. Burst mode data was simulated from the same pair of stripmap SAR data scenes considered earlier in Figure 4.2. ....	82
Figure 4.4: Profiles through InSAR phase maps shown in Figure 4.3. Unwrapped phase is calculated along the east-west direction (AA'). ....	83
Figure 4.5: InSAR phase map over Hector Mine, California obtained from a stripmap interferogram spanning the time between September 15, 1999 and October 20, 1999. The perpendicular baseline is 20 meters. Co-seismic deformation associated with the October 19, 1999 earthquake is measured. ....	85

Figure 4.6: ScanSAR InSAR phase maps for various burst overlap cases. Burst mode data was simulated from the same pair of stripmap SAR data scenes considered earlier in Figure 4.5. ....	86
Figure 4.7: Profiles through InSAR phase maps shown in Figure 4.6. Unwrapped phase is calculated along the east-west direction (AA') shown in Figure 4.5. ....	87
Figure 4.8: InSAR phase map over Yellowstone, Wyoming obtained from a stripmap interferogram spanning the time between June 28, 1993 and August 30, 1995. The perpendicular baseline is 190 meters. ....	88
Figure 4.9: ScanSAR InSAR phase maps for various burst overlap cases. Burst mode data was simulated from the same pair of stripmap SAR data scenes considered earlier in Figure 4.8. ....	89
Figure 4.10: Profiles through InSAR phase maps shown in Figure 4.9. Unwrapped phase is calculated along the east-west direction (AA') shown in Figure 4.8. ....	90
Figure 4.11: InSAR phase map over central London, UK obtained from a stripmap interferogram spanning the time between September 1, 1995 and November 3, 2000 and having a perpendicular baseline of 20 meters.. The figure shown is a small subset encompassing the land subsidence feature caused by tunnel excavation. ....	91
Figure 4.12: ScanSAR InSAR phase maps for various burst overlap cases. Burst mode data was simulated from the same pair of stripmap SAR data scenes considered earlier in Figure 4.11. ....	92

Figure 4.13: Profiles through InSAR phase maps shown in Figure 4.12. Unwrapped phase is calculated along the east-west direction (LL') shown in Figure 4.11.....	93
Figure 4.14: Stripmap and simulated ScanSAR InSAR phase map over Houston Texas obtained from stripmap ERS-2 SAR images acquired on December 26, 1995 and December 30, 1997. The perpendicular baseline is 240 meters. ....	94
Figure 4.15: Block diagram of the SBAS technique (Adapted from Berardino et al. [2002]).....	97
Figure 4.16: Comparison of azimuth-filtered and non-filtered ScanSAR InSAR phase maps. ....	105
Figure 4.17: Profiles through ScanSAR InSAR phase maps shown in Figure 4.16. The unwrapped phase through azimuth filtered interferograms (blue) is compared with non-filtered phase (red). ....	106
Figure 4.18: Ground displacement rate in the radar line-of-sight direction measured over the Phoenix metropolitan area. This velocity map was obtained from the application of the SBAS technique to a database of ScanSAR interferograms (variable burst overlap case). Locations indicated by letters A, B, and C, correspond to subsidence features in the cities of Peoria, Glendale, and Scottsdale, respectively. Pixels which are decorrelated are in grayscale (radar intensity). ....	109

Figure 4.19: Land subsidence time series generated from the SBAS technique applied to ScanSAR data. Deformation corresponding to a single pixel located in subsidence features at Peoria (A1 and A2), Glendale (B1 and B2), and Scottsdale (C1 and C2) are shown. ScanSAR SBAS results from the 100% burst overlap case and the variable burst overlap case are compared with stripmap SBAS results. ....	111
Figure 4.20: Measures of accuracy in ScanSAR SBAS results with respect to stripmap SBAS results. (A1-A2) Mean ground subsidence velocities estimated from ScanSAR data. (B1-B2) Difference between ScanSAR and stripmap velocities. (C1-C2) RMS error in ScanSAR displacements with respect to stripmap displacements. The extent of the map is indicated by a black bounding box shown in Figure 4.8. ....	113
Figure 5.1: Distribution of temporal and perpendicular baselines of interferograms formed with respect to the December 30, 1996 reference image. ....	123
Figure 5.2: Block diagram of the PS technique used in this research. ....	134
Figure 5.3: (A) Location of PS targets identified in the final estimation step using a multi-image phase coherence threshold of 0.75. (B) PS target line-of-sight deformation velocities. ....	136
Figure 5.4: DEM error-corrected deformation time series for a PS target located in (A) Peoria and (B) Glendale subsidence features. The time series was computed from stripmap data assuming a single PS target per pixel. Note that the nonlinear deformation trends are added after the removal of the DEM error component. ....	138

Figure 5.5: Location of PS targets identified in ScanSAR data with the usual PS technique with (A) multi-image phase coherence $> 0.65$ and (B) multi-image phase coherence $> 0.75$ . The single PS target per pixel model fails to detect PS targets with reasonable PS density that is required for the estimation of residual phase maps. ....	143
Figure 5.6: Percentage of stripmap PS targets that map into ScanSAR pixels with multiple PS targets. More than 75% of PS targets identified in the stripmap data would be present in ScanSAR pixels with more than one PS target. A multiple PS target model is needed to recover them. ....	145
Figure 5.7: (A) Three-dimensional SAR viewing geometry for a single resolution cell. (B) Repeat-pass InSAR imaging geometry.....	147
Figure 5.8: PS targets identified in ScanSAR data using two PS targets per pixel model. All pixels with multi-image phase coherence $> 0.75$ are considered PS targets. ....	164
Figure 5.9: ScanSAR PS line-of-sight velocity maps for pixels identified with two PS targets per pixel using (A) a multi-image phase coherence $> 0.75$ (B) a multi-image phase coherence $> 0.65$ .....	165
Figure 5.10: Histogram showing differences between ScanSAR and stripmap PS velocity estimates for (A) a multi-image phase coherence $> 0.75$ (B) a multi-image phase coherence $> 0.65$ . ....	168
Figure 5.11: Histogram showing difference between ScanSAR and stripmap PS DEM error estimates for (A) a multi-image phase coherence $> 0.75$ (B) a multi-image phase coherence $> 0.65$ . ....	169

# **CHAPTER ONE**

## **INTRODUCTION**

This research evaluates the use of scanning synthetic aperture radar (ScanSAR) for radar interferometry (InSAR) time series analysis of land subsidence. This chapter provides a brief background of SAR, radar interferometry, and InSAR time series analysis and explains the motivation for considering ScanSAR interferometry. The objectives, approach, and unique contributions of this research are described. An outline for the rest of the dissertation also is given.

### **1.1 BACKGROUND**

Synthetic aperture radar (SAR) is an active range measuring sensor system that transmits microwave pulses and records the echoes reflected from the ground surface [Curlander and McDonough, 1991]. A SAR image is a collection of radar backscatter responses from numerous targets on the surface that are illuminated by the transmitted SAR signal. SAR image data contains information about the backscatter response and the phase associated with the two-way propagation of the radar signal.

InSAR provides a means for measuring surface deformation. SAR satellites have repeating ground tracks and are able to image the surface from the same viewing geometry on each exact repeat cycle of the orbit. A pair of SAR images acquired from the same orbit track can be used for InSAR analysis. An interferogram is, in essence, the difference of the radar signal propagation phases of a pair of aligned SAR images. Differential InSAR analysis uses the information contained in the interferogram to



determine surface deformation with centimeter level accuracy over large spatial scales. Numerous studies have shown the utility of InSAR for detecting deformation associated with various geophysical phenomena, e.g., co-seismic fault movements [Massonnet et al., 1993; Zebker et al., 1994], land subsidence [Galloway et al., 1998], glacier motion [Goldstein et al., 1993], and volcano deformation [Massonnet et al., 1995; Zebker et al., 1996]. However, these InSAR analyses are limited by two major error sources: decorrelation and atmospheric effects. Decorrelation can be thought of as a loss of information due to a change in target backscatter properties between the two SAR images [Zebker and Villasenor, 1992]. Atmospheric effects are caused by differences in the phase delay as the radar signal propagates through a variable atmosphere at each of the two SAR acquisition times [Zebker et al., 1997]. A more detailed discussion of SAR signal properties, InSAR, and InSAR error sources is provided in Chapter Two.

Improved access to satellite SAR data has led to advanced InSAR processing approaches aimed at monitoring deformation over time and mitigating InSAR error sources. Satellite missions such as ERS-1, ERS-2, JERS, and Radarsat-1 began operations during the 1990s and resulted in an increased availability of SAR data. Access to regular acquisitions of stripmap data made InSAR a popular tool for researchers interested in measuring surface deformation. Consequently, in the late 1990s, the focus of InSAR studies shifted from the analysis of a single interferogram to the use of many interferograms to observe the evolution of deformation over time. Methods were developed that utilize multiple interferograms, e.g., stacking [Amelung et al., 1999] to detect sub-centimeter deformation and database inversion [Usai, 2001; Schmidt and Bürgmann, 2003] to generate deformation time series.

Advanced processing methods were developed to overcome InSAR error sources so as to measure millimeter per year deformation rates over several years of InSAR

measurements. Permanent Scatterer InSAR [Ferretti et al., 2000], the full-resolution Small Baseline Subsets (SBAS) approach [Lanari et al., 2004; Berardino et al., 2002], and a persistent scatterer method introduced by Hooper et al. [2004] mitigate decorrelation effects by identifying and tracking dominant scatterers that are not affected by decorrelation even over time scales of several years. These methods estimate and remove atmospheric noise artifacts to improve the accuracy of the deformation measurements. However, such advanced processing approaches require access to tens of SAR images acquired over the study site of interest.

The ScanSAR imaging mode is increasingly being used to address the demand for SAR data. The current generation of satellite SAR missions such as Envisat, ALOS, Radarsat-2, and TerraSAR-X operate sophisticated SAR sensors with a number of operating modes. For example, the ScanSAR mode provides greater spatial coverage at the expense of coarser spatial resolution. However, the effectiveness of ScanSAR for InSAR and InSAR time series analysis remains a virtually unexplored area of research.

## **1.2 MOTIVATION**

This section provides the motivation for considering ScanSAR interferometry on a routine basis for measuring land surface deformation.

Although various long-term monitoring techniques exist, an insufficient amount of SAR data is a limiting factor in understanding and relating the observations and derived time series to geological and anthropological processes. When operating in the stripmap mode, the repeating ground tracks of the satellites provide an opportunity for the sensor to image a study site from the same viewing geometry once every repeat cycle. Repeat-pass periods of SAR satellites are on the order of one month, e.g., ERS-1, ERS-2, and Envisat are 35 days, Radarsat-1 is 24 days, and JERS is 44 days. For example, if the

Envisat ASAR images a study site on every repeat pass, it is possible to obtain a time series of images describing the temporal evolution of a certain deforming feature on the ground, sampled at every 35 days. Moreover, SAR sensors are able to image the same study site from ascending and descending satellite tracks, with each track having the same repeat-pass period. Therefore, SAR coverage can be improved by a factor of two by acquiring images on both the ascending and the descending orbits. However, SAR images acquired from the ascending pass cannot be combined with images acquired from the descending pass for performing interferometry. If the Envisat ASAR sensor operating in stripmap mode images the study site on every single revisit, i.e. on every ascending and descending repeat pass, then it is possible to construct two independent time series of images, each sampled at 35-day intervals. This scenario represents the maximum possible SAR coverage using the stripmap mode on Envisat. However, the ideal scenario of acquiring a stripmap image on every possible opportunity is adversely affected by various mission constraints, such as acquiring data in different imaging modes, and results in a drop in data coverage.

With many of the current SAR satellites carrying advanced imaging capabilities, ScanSAR mode acquisitions are replacing the conventional stripmap mode acquisitions for portions of a SAR mission. For example, ALOS PALSAR generally acquires ScanSAR data on descending passes and stripmap data on ascending passes. Consequently, less stripmap SAR data is available for the purpose of InSAR time series generation. It is evident that as more SAR sensors begin to image in the ScanSAR mode instead of stripmap mode, there will be temporal gaps in the stripmap data acquisitions. For example, if the Envisat ASAR sensor does not acquire a stripmap image on one of its repeat passes, then the gap between two stripmap acquisitions, on either side of the missed acquisition, would be 70 days. Constructing time series with these larger sampling

intervals is not ideal for detecting seasonal deformation trends. In order to maintain the inherent time sampling provided by the repeat pass orbit, it is important to utilize all the available SAR data, including ScanSAR data. From this perspective, it is vital to investigate the usage of ScanSAR data for InSAR time series generation.

ScanSAR imaging can reduce the revisit time of the satellite to a particular study site and provide more frequent SAR coverage. When imaging in the ScanSAR mode, a SAR sensor is able to image a wide swath consisting of a number of subswaths. The sensor is able to do this by electronically steering the antenna through a set of predetermined angles. For example, an Envisat ASAR ScanSAR image consists of 5 subswaths and is 400 km wide, whereas the ASAR stripmap swath width is 100 km [Desnos et al., 2000]. Since a SAR sensor in ScanSAR mode acquires data from a large swath of land, it can image an area of interest from not only the exact stripmap repeat orbit track, but also from adjacent orbit tracks. For example, in the case of Envisat ASAR, in the 35-day exact repeat period between 11 May 2009 and 15 June 2009, the Phoenix area could be imaged 7 times using the ScanSAR mode from various adjacent descending orbit tracks, compared to only 1 possible descending orbit track acquisition from the stripmap mode (Table 1.1 and Figure 1.1). The ScanSAR revisit dates are not uniformly distributed and are either 3 days or 10 days (Table 1.1).

It should be noted that interferograms cannot be formed from ScanSAR images acquired from adjacent tracks. Consequently, the shortest possible time spanned by an interferogram formed using ScanSAR data still will be equal to the satellite orbit exact repeat period. For example, for the Envisat ASAR sensor, the shortest time spanned by an interferogram will be 35 days. Deformation time series generated using ScanSAR data separately from adjacent tracks may be merged together to obtain a combined “multiple-track” time series with a denser overall temporal sampling. However, this approach

requires some assumptions about the temporal and spatial characteristics of the observed deformation. Overall, the advantage of having a multi-fold increase in SAR data coverage through ScanSAR mode is appealing. To this end, a detailed investigation of the feasibility of performing ScanSAR interferometry on a routine basis is needed. However, there are very few studies in the literature showing interferometry results using ScanSAR data. Most of the previous research concerning ScanSAR interferometry involved the investigation of individual ScanSAR interferograms and very little research in the direction of ScanSAR InSAR time series analysis.

Table 1.1: Envisat ASAR Phoenix image dates for one orbit exact repeat cycle.

<b>Scene Number</b>	<b>Imaging Mode (Product Name)</b>	<b>Orbit Number</b>	<b>Track Number</b>	<b>Date YYYY MM DD</b>
1	Stripmap (IS2)	37627	2499	2009 05 11
2	Stripmap (IS2)	38128	2499	2009 06 15
3	ScanSAR (WSM)	37627	499	2009 05 11
4	ScanSAR (WSM)	37770	141	2009 05 21
5	ScanSAR (WSM)	37813	184	2009 05 24
6	ScanSAR (WSM)	37856	227	2009 05 27
7	ScanSAR (WSM)	37899	270	2009 05 30
8	ScanSAR (WSM)	38042	413	2009 06 09
9	ScanSAR (WSM)	38085	456	2009 06 12
10	ScanSAR (WSM)	38128	499	2009 06 15

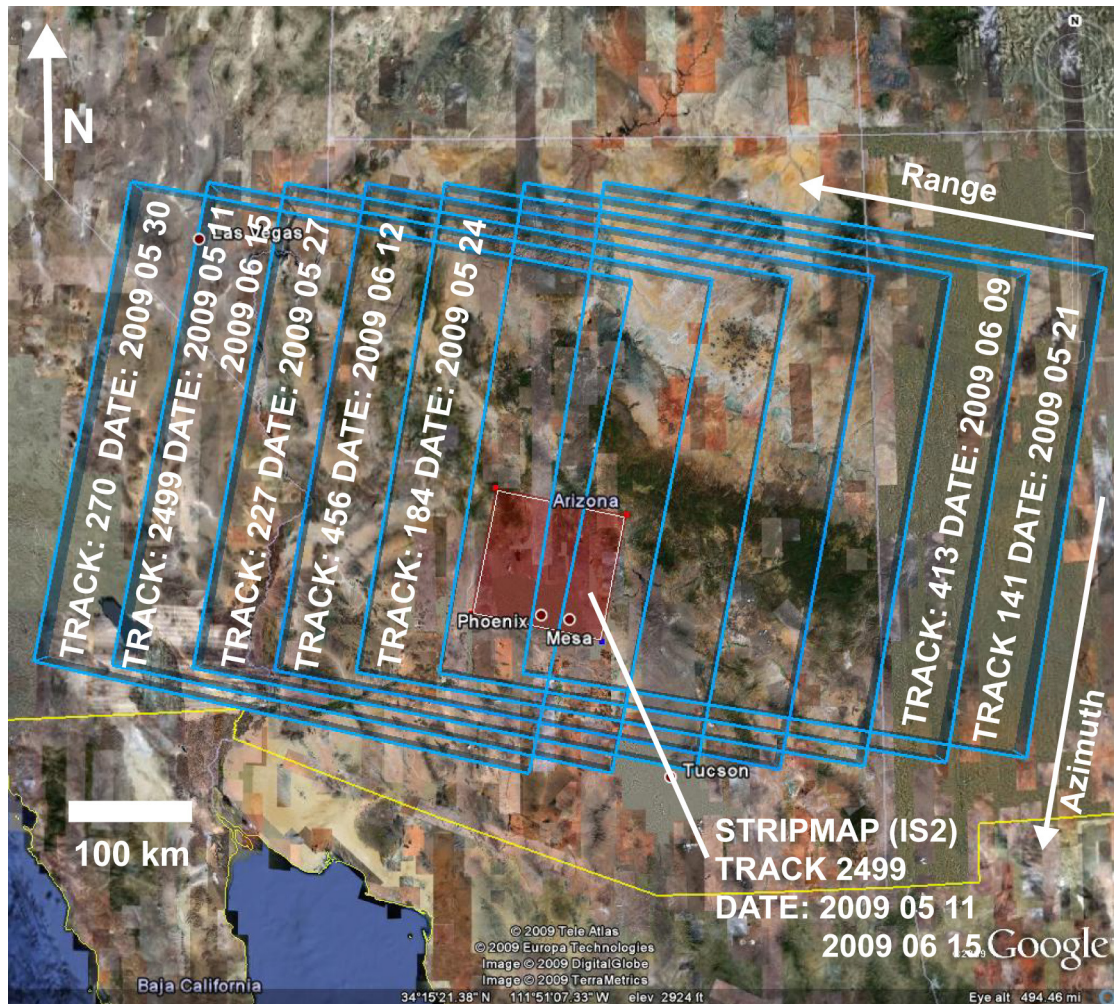


Figure 1.1: Envisat ASAR coverage over Phoenix, Arizona from adjacent descending orbit tracks for a 35-day period between 11 May 2009 and 15 June 2009. The stripmap coverage is shown in red and the ScanSAR coverage is shown in blue.

It is important to fully understand the advantages and drawbacks of ScanSAR interferometry before committing to increased ScanSAR coverage at the expense of lost stripmap data coverage. The two most important questions to be answered are:

(1) Is it possible to measure deformation phenomena of interest with ScanSAR interferometry?

(2) What is the quantifiable loss in deformation measurement quality in switching from stripmap interferometry to ScanSAR interferometry?

The effect of the various constraints and limitations of ScanSAR interferometry on InSAR time generation must be taken into account in answering the aforementioned questions. Unlike stripmap raw data, which is a continuous strip of data from a single swath, ScanSAR raw data is discontinuous. For example, an Envisat ASAR ScanSAR image (Figure 1.1) is a composite of 5 subswaths. Data from each subswath of the ScanSAR mode consists of a train of small data subsets called bursts. Interferometry using two ScanSAR images is only feasible when there is sufficient burst overlap between the two images, i.e., the bursts of the two ScanSAR images are sufficiently aligned [Guarnieri and Prati, 1996]. Also, ScanSAR images have significantly less resolution compared to stripmap data [Guarnieri et al., 2003]. A detailed explanation of burst overlap and resolution of ScanSAR mode images is provided in Chapter Three.

Despite its current limited use, ScanSAR imaging will play an important role in future InSAR analyses. For example, the proposed US Deformation, Ecosystem Structure and Dynamics of Ice (DESDynI) InSAR mission may rely on ScanSAR imaging to meet the high demand for worldwide deformation measurements (<http://desdyni.jpl.nasa.gov>). In light of future SAR missions and modifications to existing SAR mission imaging strategies, a detailed study of ScanSAR interferometry for long term ground motion monitoring will provide significant input to mission planning and InSAR research.

### **1.3 OBJECTIVES**

There are two research objectives of this work. First, I demonstrate the use of ScanSAR data in InSAR time series analysis. This is done by generating an InSAR time series using the SBAS technique applied to burst mode SAR data (ScanSAR data simulated from stripmap SAR data). This approach is applicable when the InSAR baselines and the study site are conducive for interferometry. The outcome of this objective is a characterization of the results one might expect to obtain when using coarser resolution ScanSAR data instead of stripmap SAR data in an InSAR time series analysis of land subsidence.

Second, I demonstrate the use of ScanSAR data in a persistent scatterer InSAR approach. This is done by adapting the Permanent Scatterer InSAR algorithm to process burst mode SAR data. This approach is applicable for a study site where there is significant decorrelation and only the motion of dominant scatterers is measureable. The outcome of this objective is a characterization of the extent to which persistent scatterers can be identified in ScanSAR data. As part of this work, I consider the possibility of mitigating the loss of resolution in using ScanSAR data instead of stripmap SAR data by modeling multiple persistent scatterers within one ScanSAR resolution cell.

### **1.4 APPROACH**

The viability of performing InSAR analysis using ScanSAR data on a regular basis is evaluated through a set of experiments. Reduction in resolution leads to an increase in measurement noise, i.e. ScanSAR data are noisier than stripmap data. The experiments designed for this research support the study and quantification of the noise levels in ScanSAR data in comparison to stripmap data. Advanced processing techniques



developed using stripmap data for long-term deformation monitoring are extended to ScanSAR data.

Simulated ScanSAR data are generated by “bursting” actual stripmap data. Burst mode SAR data are simulated from ERS-1/2 stripmap SAR data by intentionally omitting raw data lines from stripmap data files. I use simulated ScanSAR data for two reasons. First, a large database of ScanSAR images having favorable burst alignments does not exist. Most of the early ScanSAR acquisitions were meant for radiometric purposes rather than for interferometry [Holzner and Bamler, 2002]. Until recently, no attempts were made to ensure that there was sufficient burst overlap between repeat pass ScanSAR images to enable interferometry. For this reason, it is nearly impossible to put together a database of actual ScanSAR images suitable for InSAR applications. Second, generating ScanSAR data from stripmap data will allow for a direct comparison of the ScanSAR and stripmap InSAR time series results. The simulated ScanSAR data is equivalent to data acquired from a sensor operating in the ScanSAR mode with a single subswath that is spatially coincident with the stripmap SAR images. It will be possible to perform a pixel-to-pixel comparison of the time series deformation maps generated from the application of identical processing techniques to ScanSAR data and stripmap data.

The characteristics of the burst mode data simulated from ERS-1/2 stripmap data are very similar to the Envisat ASAR ScanSAR mode burst pattern. Various burst mode parameters are chosen in such a way that they reflect a realistic ScanSAR scenario. Also, I consider burst overlap scenarios that are realistically possible from Envisat ASAR ScanSAR mode [Rosich et al., 2007].

I utilize ERS-1/2 stripmap data over Phoenix, Arizona metropolitan area for this research. The choice of this study site was motivated by three reasons. First, a large database of stripmap ERS-1/2 SAR images collected over Phoenix area through the

1990s was available. The database has a good distribution of SAR images spanning a 9-year period between 1992 and 2000. Second, the arid region of the Phoenix area exhibits generally good InSAR phase coherence. Phase signatures caused by urban land subsidence can be clearly observed and measured. In addition to the coherent urban environment, the study site has pockets of grass covered land surfaces, such as golf courses, which decorrelate over time. The presence of both coherent and decorrelating regions within the same study site provides for a realistic example for InSAR land subsidence studies. Third, historic and ongoing subsidence in the Phoenix metropolitan area has been observed with stripmap InSAR [Buckley, 2000; Gudipati et al., 2004]. In previous research studies, various Phoenix subsidence features were analyzed using advanced InSAR processing techniques. Seasonal uplift and subsidence superimposed on a long-term subsidence trend has been observed. These studies form a benchmark for comparison and validation of results obtained from the simulated burst mode data. Familiarity with the study site and the knowledge of the locations of active subsidence make Phoenix an ideal test site.

## **1.5 CONTRIBUTIONS**

The research objectives were successfully achieved through the implementation and adaptation of existing algorithms and several unique research contributions. A burst mode SAR data processor based on the modified SPECAN algorithm [Lanari et al., 1998] was implemented. The algorithm, which utilizes the chirp-Z transform, allows for a variable output azimuth pixel spacing of the processed images. An azimuth common band filtering operation [Guarnieri and Prati, 1996] was implemented to remove phase noise associated with the non-overlapping portions of two ScanSAR bursts being combined for InSAR analysis. The SBAS and PS InSAR techniques were adapted for

ScanSAR interferometry from software originally developed by fellow PhD student Dochul Yang. A Kaiser filter [Mora et al., 2003] was designed to perform temporal filtering of time series data to separate nonlinear phase from atmospheric noise. Software pertaining to this filtering step was incorporated into the SBAS and PS algorithms. Computer code was written to perform a weighted least squares based integration of gradients on a sparse network of points. Furthermore, software was developed to perform a congruence operation that corrects small unwrapping errors after the weighted least squares integration of gradients of phase [Pritt, 1997].

There are three unique contributions of this research, which demonstrates the use of ScanSAR interferometry as a tool for land surface deformation monitoring:

First, ScanSAR SBAS InSAR time series analysis was performed. This work is the first instance where ScanSAR data has been utilized for InSAR time series generation using the SBAS technique. In a previous study, Casu et al. [2007] demonstrated that the SBAS technique can be applied to low resolution SAR data obtained from long strips of stripmap data. In their work, Casu et al. [2007] generate low resolution SAR data from stripmap images by intentionally degrading the resolution through the use of a low-pass filter and decimating by a factor of 5. In this work, I consider a thorough and detailed investigation of ScanSAR data by simulating a burst mode data pattern that is similar to the Envisat ScanSAR mode data. A time series of deformation maps indicating the evolution of land subsidence was obtained from ScanSAR interferograms.

Second, a feasibility study of ScanSAR PS InSAR analysis was performed. Guarnieri [2000] is the only known prior study where the survival of permanent scatterers in ScanSAR data was investigated. Guarnieri [2000] estimates the probability of detecting permanent scatterers in ScanSAR data by analyzing the reflectivity of the scatterers identified in stripmap data and by mapping “known” scatterers from stripmap

data into ScanSAR data. In this research, I apply an adapted Permanent Scatterer method directly to ScanSAR interferograms without using any a priori information of scatterers identified in stripmap data. Unlike in Guarnieri [2000], where the reflectivity of the scatterers was used, I detect ScanSAR permanent scatterers by their phase stability.

Third, a ScanSAR multiple persistent scatterer model was developed. For better detection of persistent scatterer pixels in ScanSAR data, I propose the use of a multiple persistent scatterer model where more than one dominant scatterer is present within a ScanSAR resolution cell. Ferretti et al. [2005] introduced the concept of multiple-scatterer or “higher order” permanent scatterer analysis by investigating the presence of multiple scatterers at different range locations within a stripmap resolution cell. Unlike Ferretti et al. [2005], the multiple scatterer model I propose as part of this research assumes that all the persistent scatterers present within the resolution cell are at the same range. Targets may be located at different sub-pixel azimuth locations but under the condition that they all are at the same slant range. In other words, the targets are located on a spherical surface whose radius is equal to the slant range to the resolution cell but confined within the boundaries of the resolution cell. Also, I apply a multiple permanent scatterer model to ScanSAR data instead of stripmap data. Due to the larger size of the ScanSAR resolution cells compared to stripmap resolution cells, it is highly likely that there will be multiple scatterers in a single ScanSAR resolution cell.

## **1.6 OUTLINE**

The rest of this document is organized in the following manner: Chapter Two presents an overview of SAR fundamentals, SAR data processing steps, a derivation of interferometric phase, and a concise discussion of InSAR error sources. Chapter Three gives an explanation of the ScanSAR data acquisition geometry, burst mode data

characteristics, burst mode data processing techniques, and the concept of burst overlap. The methodology and results pertaining to the objectives are presented in Chapter Four and Chapter Five, respectively. Results presented in Chapter Four demonstrate that ScanSAR data acquired in a realistic imaging scenario can be used to produce a deformation time series comparable to stripmap InSAR results using the SBAS advanced InSAR technique. In Chapter Five, results are shown for a modified persistent scatterer algorithm where multiple targets within a single resolution cell are modeled. A summary of conclusions and ideas for future work are presented in Chapter Six.

## **CHAPTER TWO**

### **BACKGROUND**

This chapter gives a detailed overview of SAR imaging principles, SAR signal processing, and radar interferometry (InSAR). The intention is to give the reader an overall background of the InSAR technique and its scientific application relevant to this research.

#### **2.1 SYNTHETIC APERTURE RADAR**

##### **2.1.1 SAR History**

SAR sensors have been in use for nearly half a century. The invention of SAR in 1951 is generally attributed to Carl Wiley at Goodyear Aircraft Company, Arizona [Curlander and McDonough, 1991]. He noted that the along track resolution of radar images can be improved by applying a Doppler frequency analysis. Early SAR systems developed in the 1950s and 1960s were primarily for military purposes. The first SAR system that was declassified by the Department of Defense in the late 1960s was built by the Environmental Research Institute of Michigan (ERIM) [Curlander and McDonough, 1991]. One of the early spaceborne civilian operational SAR systems was the SEASAT-A launched in 1978. SEASAT-A was used for oceanic observations, polar ice monitoring and land mapping. Following SEASAT, NASA soon flew a number of Shuttle Imaging Radar missions (SIR-A, SIR-B, SIR-C, X-SAR) from the early 1980s through the mid-1990s. The SIR missions imaged the Earth's surface using various frequencies and polarizations. In addition to the earth-observation-based missions, planetary missions to

Venus, like Pioneer launched in 1978 and Magellan launched in 1990, had SAR instruments onboard [Curlander and McDonough, 1991]. During the 1990s, SAR missions launched by space agencies across the globe, such as Radarsat-1 by the Canadian Space Agency, ERS-1, ERS-2 and Envisat by the European Space Agency and JERS-1 by the National Space Development Agency of Japan, have provided tremendous amounts of radar data for numerous scientific applications.

### 2.1.2 SAR Imaging Geometry

A typical satellite SAR system has a side-looking sensor that images the surface in a direction that is approximately perpendicular to the satellite velocity (Figure 2.1). A SAR sensor repeatedly sends and records radar pulses at a constant time interval called the pulse repetition interval (PRI). A SAR system can be designed to operate in different imaging modes, such as stripmap, ScanSAR, and spotlight modes. The two modes relevant to this study are the stripmap mode and ScanSAR mode. The stripmap mode is the conventional and most common mode of SAR imaging. From the perspective of explaining SAR and InSAR principles, a stripmap mode of data acquisition is assumed for the remainder of this chapter. ScanSAR mode operation and geometry are discussed in Chapter Three.

SAR sensors image the earth's surface by transmitting electromagnetic signals called pulses. As mentioned in Chapter One, radar pulses transmitted by a SAR antenna operating in stripmap mode illuminate a swath of land of constant width (Figure 2.1). The area illuminated by the beam is the radar beam footprint. The angle between the radar beam center line and its projection in the plane perpendicular to the satellite velocity is the squint angle  $\theta_{sq}$ . The angle between the radar beam center line and the vertical at the satellite location is the look angle  $\theta_l$ .

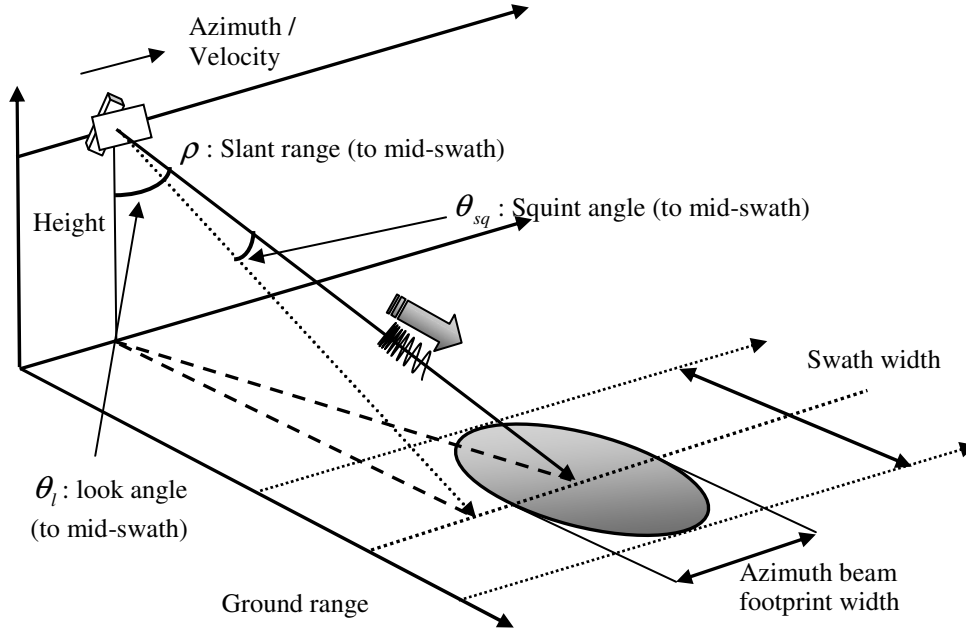


Figure 2.1: A squinted SAR imaging geometry.

SAR raw data is a collection of radar return echoes that have a finite duration. Radar echoes reflecting from targets in the radar footprint are scattered back to the sensor and are detected using a replica of the original transmitted signal. The SAR antenna detects and samples the energy and the phase of the returning radar echo. The range between the sensor and a target determines the round-trip travel time of the returning pulse. As the satellite moves in its orbit, the SAR sensor transmits and records additional pulses from different along track positions. The two distances, sensor-target range and along track position of the satellite, form the two dimensions of a SAR image. The range between the sensor and the imaged target is also called slant range  $\rho$ , while the along track direction is called azimuth. The ground range is the projection of the slant range on to the ground surface. The size of the footprint depends on the range to the target, the radar antenna beam pattern, and the geometry arising from Earth's curvilinear surface.



The *swath width* is the footprint extent in the ground range direction, while the *azimuth beam width* is the footprint length in azimuth direction.

For a simple radar system that measures range as the two-way travel time of a reflected rectangular pulse, the range resolution  $\Delta\rho_r$  is equivalent to half of the pulse duration times the velocity of the pulse:

$$\Delta\rho_r = \frac{c\tau_r}{2} \quad (2.1)$$

Consequently, to obtain fine resolution using simple rectangular pulses, the pulse duration should be very short. However, to get reasonable signal-to-noise ratio (SNR) in identifying the returning pulse, the length of the pulse would have to be very long. These two conflicting criteria limit the resolution of simple radars [Hanssen, 2001]. In SAR imaging, fine slant range resolution is obtained by transmitting a linear, frequency-modulated pulse, or chirp pulse, instead of a single-frequency pulse. The following two sections explain SAR range and azimuth signal properties and resolutions.

The ability of SAR to precisely resolve azimuth location of various scattering targets within a footprint makes it a powerful tool when compared to simple radar systems. For example, a real aperture radar cannot resolve the azimuth location of the various targets imaged by a single pulse. In such a case, the azimuth resolution is equal to the azimuth length of the radar footprint. The azimuth beam footprint width  $W_{ABFP}$  can be calculated as [Cumming and Wong, 2005]:

$$W_{ABFP} = \frac{0.866\lambda}{L_a} \rho \quad (2.2)$$

where  $\lambda$  is the radar signal wavelength,  $L_a$  is length of the SAR antenna in the azimuth direction, and  $\rho$  is the slant range to the target. From Equation 2.2, it is clear that the resolving ability of the radar can be improved by making  $W_{ABFP}$  small. One way of improving the azimuth resolution is by increasing the length of the antenna  $L_a$ . In SAR systems, high resolution in the azimuth direction is obtained by using the movement of the satellite to synthesize a large aperture antenna.

### 2.1.3 SAR Processing

Signal processing techniques are employed to compress the raw data contained in the recorded radar echoes into a processed SAR image. The response or return energy of each target that is imaged by the sensor is spread in the two dimensions of range and azimuth. The range extent of the uncompressed target response is equal to the length of the transmitted signal. The azimuth extent of the uncompressed target response is equal to the duration for which that target is within the radar beam footprint. High resolution in the range and azimuth directions is achieved by gathering the two-dimensional uncompressed response using the so-called pulse compression techniques. The Range-Doppler algorithm is one such technique that uses the matched filtering process to perform the pulse compression.

The Range-Doppler algorithm is a widely used SAR processing algorithm that was developed originally to process SEASAT SAR data [Bennett and Cumming, 1979]. It is a commonly utilized method when processing datasets with low squint angles, such as SAR data from ERS-1 and ERS-2. Although SAR data is two-dimensional wherein the range phase and azimuth phase are coupled, SAR processing for the low-squint geometry can be split into a sequence of one-dimensional processing steps (Figure 2.2). The Range Cell Migration Correction (RCMC) performed through range interpolations helps in

making azimuth processing independent of range compression. Separate matched filtering operations are used to compress the raw SAR data into a processed image. SAR signal properties and their compressed responses discussed in the next four sections form the basis for the Range-Doppler processor.

#### 2.1.4 Range Signal

A SAR chirp pulse signal  $s_t(t)$  of unit amplitude, pulse duration  $\tau_r$ , and transmitted at time  $t = 0$ , can be written as:

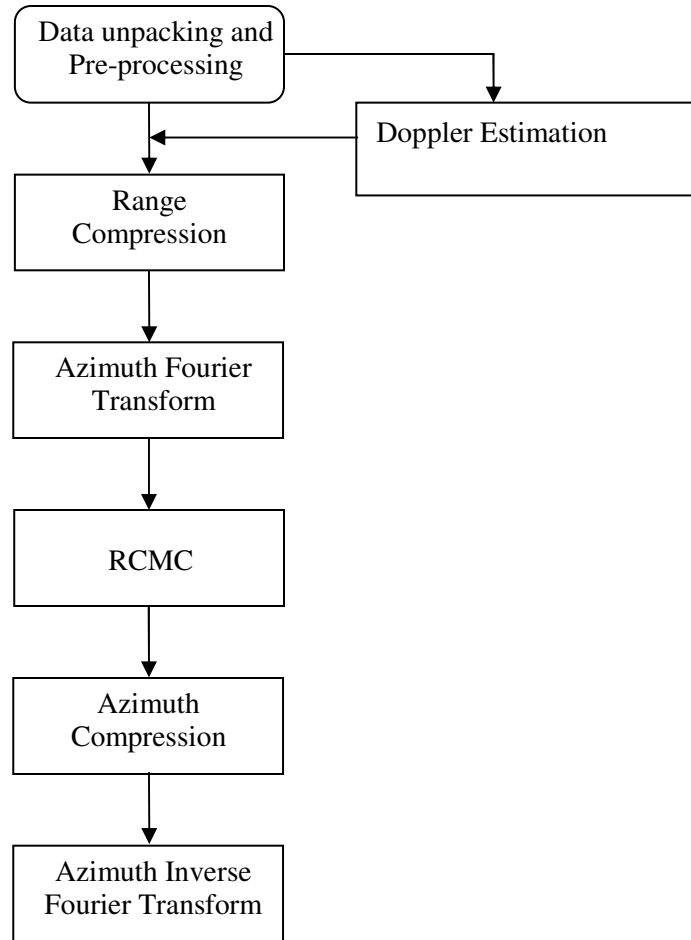


Figure 2.2: Flowchart describing the basic steps of the Range-Doppler algorithm.

$$s_t(t) = \exp \left\{ j2\pi \left[ f_0 t + \frac{K_r}{2} t^2 \right] \right\} \text{rect} \left[ \frac{t}{\tau_r} \right] \quad (2.3)$$

where  $f_0$  is the center frequency of the radar signal,  $K_r$  is the chirp slope (i.e., the rate of change of frequency), and  $\text{rect}[t/\tau_r]$  is the standard rectangular function indicating time  $t$  varies from  $-\tau_r/2$  to  $\tau_r/2$ . It is evident that the instantaneous frequency of the transmitted signal varies linearly with time and the variation in phase is quadratic.

The received signal  $s_r(t)$  can be modeled as the delayed transmitted signal:

$$s_r(t) = s_t(t - t_\rho) = \exp \left\{ j2\pi \left[ f_0(t - t_\rho) + \frac{K_r}{2} (t - t_\rho)^2 \right] \right\} \text{rect} \left[ \frac{t - t_\rho}{\tau_r} \right] \quad (2.4)$$

where  $t_\rho = 2\rho/c$  is the two-way travel time to the target,  $\rho$  is the instantaneous slant range to the target, and  $c$  is the speed of light. After *basebanding*, an operation that removes the original carrier signal, the return signal can be expressed as:

$$s_r(t) = \exp \left\{ -j \frac{4\pi f_0 \rho}{c} \right\} \exp \left\{ j\pi K_r \left( t - \frac{2\rho}{c} \right)^2 \right\} \text{rect} \left[ \frac{t - t_\rho}{\tau_r} \right] \quad (2.5)$$

The received radar signal (Equation 2.5) is compressed using a matched filter operation. The range-compressed response  $s_{cr}(t)$  is the convolution of the received signal  $s_r(t)$  with the unit impulse response of the matched filter  $h_r(t)$  [Cumming and Wong, 2005]:

$$s_{cr}(t) = s_r(t) * h_r(t) \quad (2.6)$$

where

$$h_r(t) = \exp\{-j\pi K_r t^2\} \text{rect}\left[\frac{t}{\tau_r}\right] \quad (2.7)$$

The convolution operation is conveniently implemented in the frequency domain using the Fourier Transform.

The range-compressed response can be written as:

$$s_{cr}(t) \cong K_r \tau_r \text{sinc}\left[\pi K_r \tau_r (t - t_\rho)\right] \exp\left\{-j\frac{4\pi}{\lambda} \rho\right\} \quad (2.8)$$

where  $\text{sinc}(x) \equiv \sin(\pi x)/\pi x$ . The range resolution  $\Delta\rho_r$  after range compression matched filtering is the width of the sinc function in Equation 2.8, which is also inversely proportional to the range bandwidth  $B_{WR}$  of the transmitted chirp pulse:

$$\Delta\rho_r = \frac{c}{2B_{WR}} \quad (2.9)$$

where  $B_{WR} = |K_r| \tau_r$ . For ERS-1 and ERS-2, the slant range resolution without matched filtering is 6 km. However, when the pulse is compressed with a matched filter, the slant range resolution is 8 meters.

Before discussing the resolution of a SAR image in the azimuth direction, it is important to understand the concept of Doppler frequency in SAR signal.

### 2.1.5 Doppler History and Azimuth Signal

The motion of the satellite allows the sensor to image a target from various azimuth positions and thereby, various azimuth angles (Figure 2.3). These angles are called the instantaneous squint angles. One of these angles is the beam center squint angle, i.e., the instantaneous squint angle when the target is in the beam center. The motion of the satellite creates relative motion between the sensor and the imaged target, leading to a Doppler shift in the frequencies of the received signal. The observed Doppler shift is proportional to the projection of the satellite velocity vector in the sensor-target direction [Cumming and Wong, 2005]:

$$f_{di} = \frac{2V \sin \theta_{isq}}{\lambda} \quad (2.10)$$

where  $f_{di}$  is the instantaneous Doppler frequency,  $V$  is the satellite along track velocity,  $\theta_{isq}$  is the instantaneous squint angle, and  $\lambda$  is the wavelength of the radar signal. The Doppler frequency is a function of the instantaneous squint angle and varies with the satellite azimuth position. The Doppler centroid  $f_{DC}$  is defined as the Doppler frequency when the target is in the center of the radar beam:

$$f_{DC} = \frac{2V \sin \theta_{sq}}{\lambda} \quad (2.11)$$

In addition to the variation in the Doppler frequency, the received signal strength also varies with the relative position of the target within the radar footprint. The strength of the signal is a function of the target location within the antenna beam pattern. The return signal is strongest when the target is in the beam center and the signal strength decreases in a nonlinear way away from the beam center (Figure 2.4 (A)). The variation of the return signal strength as a function of azimuth time is nonlinear but symmetrical about the radar beam center time (Figure 2.4 (B)). The Doppler frequency variation can be approximated as a linear function of azimuth time (Figure 2.4 (C)).

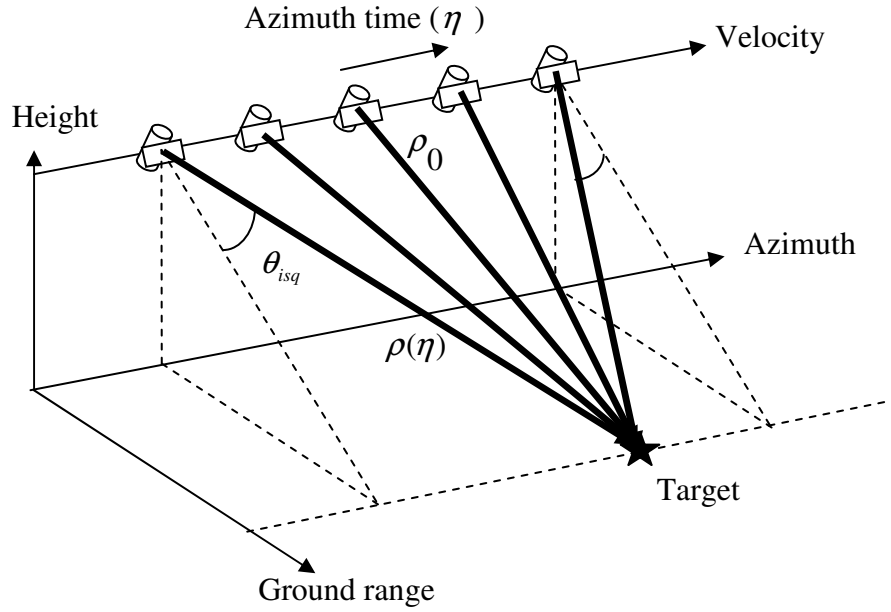


Figure 2.3: A sketch of the variation of slant range and squint angle to a target as it is imaged through time.

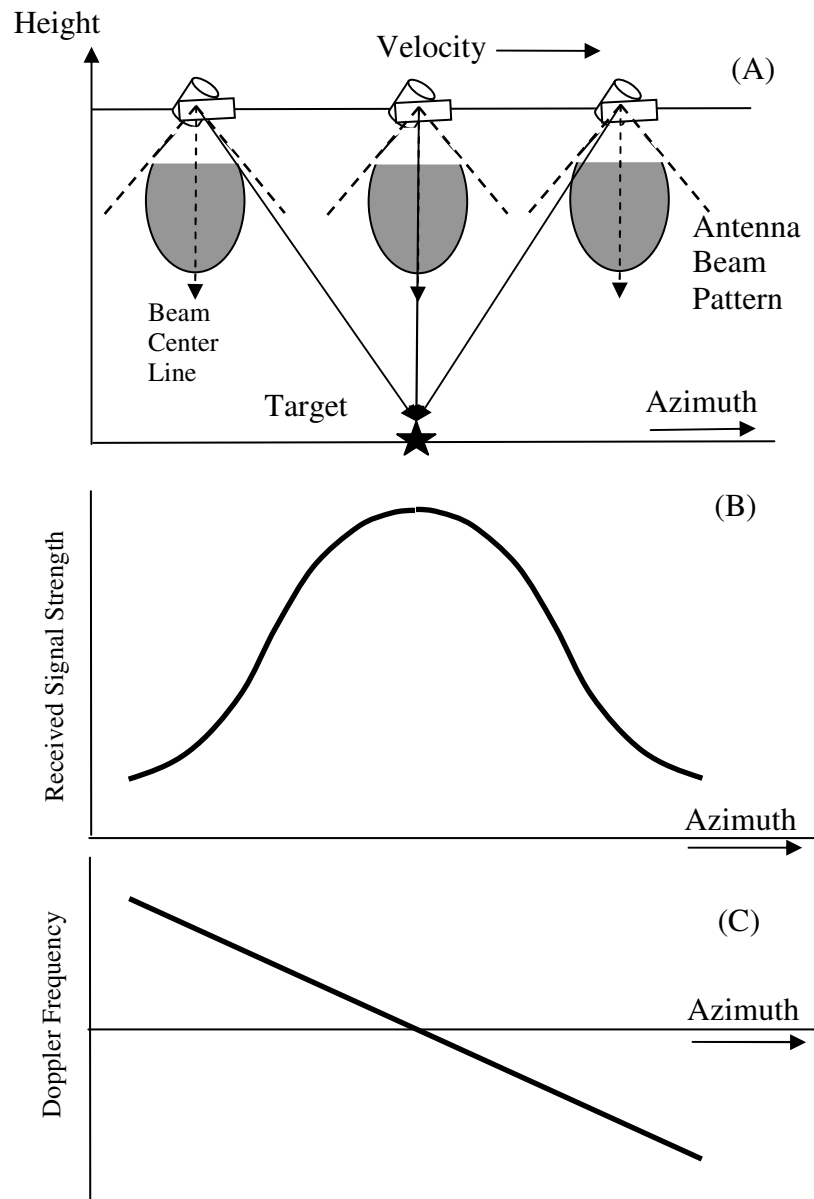


Figure 2.4: A 2-D projection of the slant range plane onto the vertical plane defined by azimuth and height (Adapted from Cumming and Wong [2005]). (A) Relative position of the target within the radar beam as the satellite travels from left to right. (B) Variation in the received signal strength with azimuth. (C) Linear variation of Doppler frequency in azimuth.



### *Azimuth Signal*

The azimuth component of the received radar signal can be approximated as a chirp signal by assuming a parabolic variation of the instantaneous slant range with azimuth time. The instantaneous slant range  $\rho$  to the target from the sensor (Figure 2.3) as a function of the azimuth time  $\eta$  can be written as:

$$\rho^2(\eta) = \rho_0^2 + V^2(\eta - \eta_0)^2 \quad (2.12)$$

where  $\eta_0$  is the azimuth time when the instantaneous squint angle is zero,  $\rho_0$  is the nearest slant range (i.e., the slant range at  $\eta = \eta_0$ ), and  $V$  is the velocity of the satellite. Noting that  $\rho_0 \gg V(\eta - \eta_0)$ , and using binomial expansion, the hyperbolic form of the slant range (Equation 2.12) can be approximated with the parabolic form:

$$\rho(\eta) = \sqrt{\rho_0^2 + V^2(\eta - \eta_0)^2} = \rho_0 \sqrt{1 + \frac{V^2(\eta - \eta_0)^2}{\rho_0^2}} \cong \rho_0 + \frac{V^2(\eta - \eta_0)^2}{2\rho_0} \quad (2.13)$$

A two-dimensional SAR signal can be written by substituting Equation 2.13 in Equation 2.8 and by dropping the rect function terms:

$$s_{cr}(t, \eta) \cong A_g(\eta - \eta_0) B_{WR} \text{sinc}[\pi B_{WR}(t - t_\rho)] \exp\left\{-j \frac{4\pi\rho_0}{\lambda}\right\} \exp\left\{-j\pi \frac{2V^2(\eta - \eta_0)^2}{\lambda\rho_0}\right\} \quad (2.14)$$

where  $A_g(\eta - \eta_0)$  is the azimuth antenna pattern and is essentially a representation of the curve shown in Figure 2.4 (B). From the perspective of the signal phase, the antenna pattern term is inconsequential and can be ignored for subsequent analysis.

The modulation of the signal phase as a function of azimuth time  $\eta$  is evident in the last exponential term in Equation 2.14. The signal phase varies in a quadratic fashion in azimuth with the phase becoming zero when the target is closest to the sensor or the target zero-Doppler time. Analogous to the frequency modulation seen in the range signal, the SAR signal in the azimuth direction also has linear FM characteristics. The rate of change of azimuth frequency can be written as:

$$f_R = -\frac{2V^2}{\lambda\rho_0} \quad (2.15)$$

where  $f_R$  is the rate of change of the Doppler frequency or simply the *Doppler rate*. Under the assumption of the principle of stationary phase, the instantaneous Doppler frequency at any azimuth time  $\eta$  can be written as [Cumming and Wong, 2005]:

$$f_{di}(\eta) \cong f_{DC} + f_R\eta \quad (2.16)$$

Using the condition that Doppler frequency is zero when  $\eta = \eta_0$ , we get:

$$\eta_0 = -\frac{f_{DC}}{f_R} \quad (2.17)$$

We also note that the Doppler history of a target on the ground can be approximated with a linear FM chirp signal. In the general case where the Doppler centroid is non-zero,  $\eta_0$  refers to the zero-Doppler time with respect to the beam center time ( $\eta = 0$ ).

The bandwidth of the azimuth chirp signal depends on the time duration for which the target is within the radar beam footprint. The time of exposure or aperture time  $T_a$  is

the azimuth beam width divided by the satellite velocity and can be written as [Cumming and Wong, 2005]:

$$T_a = \frac{(0.886\lambda)}{L_a} \frac{\rho_0}{V} \quad (2.18)$$

where  $\rho_0$  is the closest range to target and  $L_a$  is the length of antenna length. Based on Equations 2.15 and 2.18, the azimuth Doppler frequency bandwidth can be estimated to be:

$$B_{WD} = T_a |f_R| = \frac{(1.772)V}{L_a} \quad (2.19)$$

### ***Azimuth Resolution***

Analogous to the range resolution of a chirp pulse, we can calculate the synthetic aperture radar azimuth resolution  $\Delta\rho_a$  processed by an azimuth matched filter as:

$$\Delta\rho_a = \frac{V}{2} \frac{1}{B_{WD}} = \frac{L_a}{1.772} \quad (2.20)$$

For ERS-1 and ERS-2, the real aperture radar azimuth resolution without matched filtering is 4 km, whereas, with the synthetic aperture and matched filtering, the synthetic aperture radar azimuth resolution is 5 meters. So, a resolution cell of a processed ERS-1 or ERS-2 SAR image is approximately 8 meters by 5 meters in slant range and azimuth, respectively.

### ***Range Cell Migration Correction***

The variation of the sensor-target range with azimuth time leads to a corresponding variation in the location of the range compressed response of the target in successive radar echoes. The instantaneous sensor-target range can be approximated as a parabolic function in azimuth time. Typically for satellite SAR systems, the range pixel spacing, which depends on the sampling frequency of the returned signal, is much smaller than the variations in instantaneous sensor-target range seen over the target exposure time. The parabolic sensor-target range variation results in a target response that is spread over many range pixels in azimuth. The range trajectory is said to migrate through the range pixels, and this migration complicates the azimuth compression. In order to facilitate the processing of 2-D SAR data through separate, one-dimensional processing steps, an additional step is performed called the Range Cell Migration Correction (RCMC) [Cumming and Wong, 2005]. After applying RCMC, the signal shown in Equation 2.14 can be written as:

$$s_{cr}(t, \eta) \cong B_{WR} \text{sinc}[\pi B_{WR}(t - t_{\rho 0})] \exp\left\{-j \frac{4\pi \rho_0}{\lambda}\right\} \exp\left\{-j\pi \frac{2V^2(\eta - \eta_0)^2}{\lambda \rho_0}\right\} \quad (2.21)$$

where  $t_{\rho 0} = 2\rho_0/c$ .

### ***Azimuth Compression***

An azimuth matched filter compresses the target to the location corresponding to the center of the radar beam. The azimuth matched filter operation is the convolution of the range compressed and range migration corrected signal  $s_{cr}(t, \eta)$  with the unit impulse

response of the azimuth matched filter  $h_A(\eta)$ . The unit impulse response of the azimuth matched filter can be written as:

$$h_A(\eta) = \exp\{-j\pi f_R \eta^2\} \text{rect}\left[\frac{\eta}{T_A}\right] \quad (2.22)$$

The final compressed SAR signal response can then be written as [Cumming and Wong, 2005]:

$$s_{cr}(t, \eta) \cong B_{WR} \text{sinc}[\pi B_{WR}(t - t_{\rho_0})] B_{WD} \text{sinc}[\pi B_{WD}(\eta - \eta_0)] \exp\left\{-j \frac{4\pi \rho_0}{\lambda}\right\} \quad (2.23)$$

We see that the compressed response is the superposition of two sinc functions in two dimensions, each with a different bandwidth. Also, we note that the phase of a compressed SAR signal corresponding to the peak of the two-dimensional sinc function (i.e., at  $\eta = \eta_0$ , and  $t = t_{\rho_0}$ ) is proportional to the two-way range to the target when the sensor is at the beam center location.

### ***Squinted Geometry or Non-Zero Doppler Centroid Case***

In the case of a non-zero Doppler centroid, the beam center slant range  $\rho_1$  can be expressed as:

$$\rho_1 = \sqrt{\rho_0^2 + V^2 \eta_0^2} \quad (2.24)$$

By substituting Equation 2.24 in Equation 2.12, we can write the instantaneous slant range  $\rho(\eta)$  to the target in terms of beam center slant range  $\rho_1$ :

$$\rho(\eta) = \sqrt{\rho_1^2 + V^2\eta^2 - 2V^2\eta_0\eta} = \rho_1 \sqrt{1 + \frac{V^2\eta^2 - 2V^2\eta_0\eta}{\rho_1^2}} \quad (2.25)$$

Using the parabolic approximation for Equation 2.25, we can write the two-dimensional range-compressed and RCMC-applied azimuth signal as:

$$s_{cr}(t, \eta) \cong A_g(\eta) B_{WR} \text{sinc}[\pi B_{WR}(t - t_{\rho_1})] \exp\left\{-j \frac{4\pi}{\lambda} \rho_1\right\} \times \exp\left\{-j \frac{2\pi V^2}{\lambda \rho_1} (\eta^2 - 2\eta_0\eta)\right\} \quad (2.26)$$

In this case, the azimuth matched filter can be written as:

$$h_A(\eta) = \exp\left\{j\pi(2f_{DC}\eta - f_R\eta^2)\right\} \text{rect}\left[\frac{\eta}{T_A}\right] \quad (2.27)$$

The final two-dimensional azimuth-compressed response in the squinted geometry case is:

$$s_{cr}(t, \eta) \cong B_{WR} \text{sinc}[\pi B_{WR}(t - t_{\rho_1})] B_{WD} \text{sinc}[\pi B_{WD}\eta] \exp\left\{-j \frac{4\pi\rho_1}{\lambda}\right\} \quad (2.28)$$

where the azimuth antenna pattern has been ignored. Similar to the zero-Doppler case, the response is compressed to the beam center time in the squinted geometry case. Also,

the phase at the peak of the compressed response is proportional to the slant range to the target at the beam center time. Note that in the squinted geometry, the Doppler rate is calculated based on the beam center slant range.

### 2.1.6 Backscatter Amplitude and Phase

In addition to the sensor-target distance, the phase and amplitude of the SAR return signal is also dependent on the specific backscatter characteristics of the target. Surface characteristics like roughness of the surface being imaged and orientation of the target with respect to the radar beam are some of the factors that influence the backscatter response. In the discussion of the SAR signal in the preceding sections, the backscatter properties of the target or resolution cell were ignored to simplify the equations. The backscatter response of a single target or resolution cell can be modeled as the summation of backscatter responses from a number of elemental scatterers located within a single resolution cell.

The backscatter response of a target has two components: backscatter phase and backscatter amplitude. The backscatter amplitude is an indicator of the amount of energy reflected back by the target to the sensor, and it depends on the sensor-target range and geometry, the antenna pattern, and the reflective properties of the target. After applying the two-way spherical gain and the antenna pattern gain, the resulting energy of the signal is representative of the backscatter amplitude  $A_{bs}$  of the target. The interaction of the SAR signal with the target or resolution cell produces a phase shift in the reflected pulse. This phase shift is in addition to the phase shift caused by the two-way propagation of the signal to the target. The additional phase shift is called the backscatter phase  $\psi_{bs}$  of the target. Consequently, the composite complex backscatter response for a resolution cell at a slant range  $\rho$  can be written as:

$$s = A_{bs} \exp(j\psi_{bs}) \exp\left(-j\frac{4\pi}{\lambda}\rho\right) \quad (2.29)$$

This concludes the section of SAR imaging principles, signal properties, and processing. The following section explains the concepts of SAR interferometry.

## 2.2 SYNTHETIC APERTURE RADAR INTERFEROMETRY

### 2.2.1 Repeat-Pass InSAR

InSAR is a technique of combining two or more SAR acquisitions coherently. Repeat-pass InSAR makes use of two SAR images acquired on different dates from repeat orbits of a satellite with almost identical viewing geometries. The idea of interferometry is based on the provision that the backscatter response of resolution cell on the ground does not change over the time period of separation between the two SAR images. If this condition is met, then the phase difference of the resolution cell will be dependent only on the difference in the two-way signal propagation times.

#### *Interferometric Phase*

If  $s_1$  and  $s_2$  are the complex SAR signals of a target imaged on the reference date and secondary date, respectively, then the complex interferogram signal  $I$  is defined as the product of  $s_1$  and the complex conjugate of  $s_2$ :

$$I = s_1 s_2^* = A_{bs1} A_{bs2} \exp[j(\psi_{bs1} - \psi_{bs2})] \exp\left[-j\frac{4\pi}{\lambda}(\rho_1 - \rho_2)\right] \quad (2.30)$$



where  $A_{bs1}$  and  $A_{bs2}$  are the backscatter amplitudes,  $\psi_{bs1}$  and  $\psi_{bs2}$  are the backscatter phases, and  $\rho_1$  and  $\rho_2$  are the slant ranges to the target on the reference and secondary SAR images, respectively. If we assume that the backscatter responses of the target on the reference and secondary image are identical, i.e.,  $\psi_{bs1} = \psi_{bs2} = \psi_{bs}$  and  $A_{bs1} = A_{bs2} = A_{bs}$ , then Equation 2.33 becomes:

$$I = A_{bs}^2 \exp\left\{-j \frac{4\pi}{\lambda} (\rho_1 - \rho_2)\right\} \quad (3.31)$$

The interferometric phase  $\phi_{\text{int}}$  arising from the difference in slant range to the target in the two SAR images, measured modulo  $2\pi$  is:

$$\phi_{\text{int}} = \frac{4\pi}{\lambda} \delta\rho \quad (2.32)$$

where  $\delta\rho$  is the difference in slant ranges to the target.

### ***Relation of Interferometric Phase to Satellite-Earth Geometry and Topography***

Starting from the repeat-pass InSAR geometry (Figure 2.5), the interferometric phase can be related to the satellite orbits, an earth model, and the topography. In Figure 2.5, the satellite is flying into the page and imaging to the right at each of the two satellite locations  $S_{p1}$  and  $S_{p2}$ . A zero-squint angle for the radar beam center is assumed. The vector from the reference satellite position  $S_{p1}$  to the secondary satellite position  $S_{p2}$  is the interferometric baseline vector  $\vec{B}$ . The slant range vectors to the target  $P_0$  from satellite positions  $S_{p1}$  and  $S_{p2}$  are  $\vec{\rho}_1$  and  $\vec{\rho}_2$ , respectively. Point  $P_0$  is the location of the target at an elevation  $z$  above a known reference surface such as the ellipsoid model of

the earth.  $P_{RS}$  is a point on the reference surface which is at the same slant range to the satellite as point  $P_0$ . The look angle to  $P_0$  from  $S_{P1}$  is  $\theta_l$ , while the look angle to  $P_{RS}$  from  $S_{P1}$  is  $\theta_{IRS}$ . Using these definitions for parameters shown in Figure 2.5, we proceed to derive the relationship between the interferometric phase, satellite-target geometry, the earth surface model and the topography.

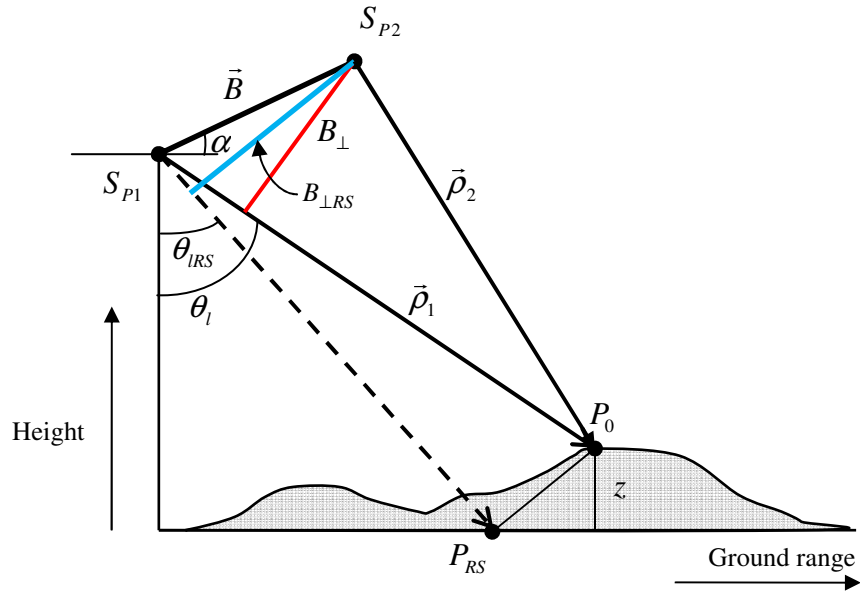


Figure 2.5: A 2-D sketch describing interferometry geometry. Satellites at positions  $S_{P1}$  and  $S_{P2}$  are assumed to be flying into the page, imaging to their right. Points  $S_{P1}$ ,  $S_{P2}$ ,  $P_{RS}$ , and  $P_0$  are all in the same plane.

The interferometric phase  $\phi_{int}$  associated with point  $P_0$  can be modeled as:

$$\phi_{int} = \phi_{RS} + \phi_{TOPO} + \phi_{DEF} \quad (2.33)$$

where  $\phi_{RS}$  is the interferometric phase due to the reference surface,  $\phi_{TOPO}$  is the interferometric phase due to topography (i.e., due to the elevation  $z$  of point  $P_0$  above the reference surface), and  $\phi_{DEF}$  is the interferometric phase due to the deformation of the target at  $P_0$ . It is noted that  $\phi_{DEF}$  represents only that deformation in the radar line-of-sight direction. The phase noise sources will be considered later in this chapter.

The difference in slant range  $\delta\rho$  to  $P_0$  between the two passes can be written as:

$$\delta\rho = \rho_2 - \rho_1 = \left( \sqrt{(\rho_1 - B_{\parallel})^2 + B_{\perp}^2} + \Delta\rho_{DEF} \right) - \rho_1 \quad (2.34)$$

where

$$B_{\parallel} = B \sin(\theta_l - \alpha) \quad (2.35a)$$

$$B_{\perp} = B \cos(\theta_l - \alpha) \quad (2.35b)$$

and  $B_{\parallel}$  is the parallel baseline component,  $B_{\perp}$  is the perpendicular baseline component, and  $\Delta\rho_{DEF}$  is the change in range due to deformation of the target. Similarly, the difference in slant range  $\delta\rho_{RS}$  to  $P_{RS}$  between the two passes can be written as:

$$\delta\rho_{RS} = \sqrt{(\rho_1 - B_{\parallel RS})^2 + B_{\perp RS}^2} - \rho_1 \quad (2.36)$$

where

$$B_{\parallel RS} = B \sin(\theta_{IRS} - \alpha) \quad (2.37a)$$

$$B_{\perp RS} = B \cos(\theta_{IRS} - \alpha) \quad (2.37b)$$

The interferometric phase due to the reference surface point  $P_{RS}$  can be written as:

$$\phi_{RS} = \frac{4\pi}{\lambda} \delta\rho_{RS} \quad (2.38)$$

The flattened interferometric phase  $\phi_{FLAT}$  is found by subtracting the reference surface interferometric phase  $\phi_{RS}$  from the total interferometric phase  $\phi_{int}$  :

$$\begin{aligned} \phi_{FLAT} &= \phi_{int} - \phi_{RS} = \frac{4\pi}{\lambda} (\delta\rho - \delta\rho_{RS}) \\ &= \frac{4\pi}{\lambda} \left[ \left( \sqrt{(\rho_1 - B_{\parallel})^2 + B_{\perp}^2} - \rho_1 + \Delta\rho_{DEF} \right) - \left( \sqrt{(\rho_1 - B_{\parallel RS})^2 + B_{\perp RS}^2} - \rho_1 \right) \right] \\ &= \frac{4\pi}{\lambda} \left[ \rho_1 \sqrt{1 - \frac{2B_{\parallel}}{\rho_1} + \frac{B^2}{\rho_1^2}} - \rho_1 \sqrt{1 - \frac{2B_{\parallel RS}}{\rho_1} + \frac{B^2}{\rho_1^2}} + \Delta\rho_{DEF} \right] \end{aligned} \quad (2.39)$$

It is noted that  $\phi_{FLAT}$  is known only modulo  $2\pi$  since  $\phi_{int}$  is only known modulo  $2\pi$  . A complex-valued representation of the flattened interferometric phase, in which phase values are always modulo  $2\pi$  , is known as the flattened interferogram.

### ***Approximation of the Flattened Interferometric Phase***

By using binomial expansion and ignoring higher order terms, the flattened interferometric phase in Equation 2.39 can be approximated as:

$$\begin{aligned} \phi_{FLAT} &\cong \frac{4\pi}{\lambda} [B_{\parallel RS} - B_{\parallel} + \Delta\rho_{DEF}] \\ &= \frac{4\pi}{\lambda} [B \sin(\theta_{IRS} - \alpha) - B \sin(\theta_l - \alpha) + \Delta\rho_{DEF}] \end{aligned} \quad (2.40)$$

Noting that the change in look angle  $\delta\theta = \theta_l - \theta_{IRS}$  is small (i.e.,  $\delta\theta \ll 1$ ), the flattened interferometric phase in Equation 2.40 can be written as:

$$\phi_{FLAT} = \frac{4\pi}{\lambda} [-B_{\perp RS} \delta\theta + \Delta\rho_{DEF}] \quad (2.41)$$

The change in look angle  $\delta\theta$  can be related to the height  $z$  of the target above the reference surface [Hanssen, 2001]:

$$\delta\theta = \frac{z}{\rho_1 \sin \theta_{IRS}} \quad (2.42)$$

Substituting Equation 2.42 in Equation 2.41, the flattened interferometric phase becomes:

$$\phi_{FLAT} = \phi_{TOPO} + \phi_{DEF} \cong -\frac{4\pi}{\lambda} \frac{B_{\perp RS}}{\rho_1 \sin \theta_{IRS}} z + \frac{4\pi}{\lambda} \Delta\rho_{DEF} \quad (2.43)$$

It should be noted that the flattened interferometric phase is very sensitive to the deformation of the target as compared to the elevation of the target above the reference surface. The ambiguity height  $H_A$  is the topographic relief required to change the topographic phase component by  $2\pi$  radians and can be written as:

$$H_A = \frac{\lambda \rho_1 \sin \theta_{IRS}}{2B_{\perp RS}} \quad (2.44)$$

On the other hand, the amount of deformation needed to change the deformation phase component by  $2\pi$  radians is  $\lambda/2$ . The topographic ambiguity height is 100-1000 times larger than the deformation ambiguity height.

Since the calculated flattened phase is known only modulo  $2\pi$ , an *unwrapping* operation of the phase has to be undertaken to find the absolute phase. Ghiglia and Pritt [1998] provide an overview of the phase unwrapping problem. The solution of the phase unwrapping problem is inherently non-unique and strongly dependent on the assumptions made on phase behavior [Hanssen, 2001].

Repeat-pass InSAR has been used for several mapping applications. Early applications of InSAR focused on estimating the topographic phase with an assumption that there is no ground deformation. Li and Goldstein [1987, 1990] are credited with the first demonstration of repeat-pass interferometry for topography mapping using SEASAT data. A more impressive application of SAR interferometry, differential interferometry, was first demonstrated by Gabriel et al. [1989] to measure surface deformation.

### 2.2.2 Differential Interferometry

The aim of differential InSAR is to accurately extract the deformation phase  $\phi_{DEF}$  from the measured interferometric phase. By using a digital elevation model (DEM) of the study site, the topographic component of the interferometric phase  $\phi_{TOPO}$  can be removed from the flattened interferogram to obtain what is called as a differential interferogram. A differential interferogram is a complex-valued image where the deformation phase is represented modulo  $2\pi$ . Finally, a phase unwrapping operation is carried out to estimate the unwrapped differential interferometric phase. Many two-dimensional phase unwrapping algorithms have been used for InSAR applications. These include the Residue-cut method [Goldstein et al, 1998; Chen and Zebker, 2000] and the

Minimal Cost Flow method [Constantini, 1996, 1998; Flynn, 1997; Chen and Zebker, 2000].

### 2.2.3 InSAR Limitations and Noise Sources

As is the case with any physical measurement system, InSAR has its limitations and is affected by noise sources. The accuracy with which deformation is estimated is dependent on the levels of noise. A review of limitations of SAR interferometry using ERS data is given by Massonnet and Feigl [1998]. The biggest limitation of InSAR is the phenomenon of decorrelation. Decorrelation can be both a limitation and a noise source. In addition to decorrelation, there are a number of noise sources affecting the differential interferometric phase, some of which can be modeled and estimated as errors. In the presence of noise, the unwrapped differential interferometric phase can be written as:

$$\phi_{DIFF} = \phi_{DEF} + \phi_{DIFF\_NOISE} \quad (2.45)$$

Further, noise in the differential interferometric phase can be represented as:

$$\phi_{DIFF\_NOISE} = \Delta\phi_{DECOR} + \Delta\phi_{ATM} + \Delta\phi_{TOPO} + \Delta\phi_{ORBITS} + \Delta\phi_{\eta} \quad (2.46)$$

where  $\Delta\phi_{DECOR}$  is the noise associated with decorrelation,  $\Delta\phi_{ATM}$  the noise associated with a variable atmosphere,  $\Delta\phi_{TOPO}$  is the phase error associated with height errors in the DEM,  $\Delta\phi_{ORBITS}$  is the error associated with satellite orbit errors, and  $\Delta\phi_{\eta}$  represents random noise. This section presents a discussion of each of these noise sources.

### ***Decorrelation***

Repeat-pass radar interferometry can be performed under the condition that the imaged targets remain coherent. Loss of coherence, called decorrelation, is the difference in the backscatter properties of the resolution cells whose phase is being interfered. Mathematically, it is the breakdown of the assumptions made in deriving Equation 2.30 from Equation 2.31. The correlation coefficient  $\gamma_{cc}$  is a measure of correlation of the received SAR signals on the two images and can be defined as [Ziemer and Tranter, 1995]:

$$\gamma_{cc} = \frac{\left\| \langle s_1 s_2^* \rangle \right\|}{\sqrt{\langle s_1 s_1^* \rangle \langle s_2 s_2^* \rangle}} \quad (2.47)$$

where the  $\langle \rangle$  operator represents the ensemble average of the signal. The value of the correlation coefficient is a fraction varying between 0 and 1, with 0 indicating complete decorrelation and 1 indicating perfect correlation.

There are a number of reasons for phase decorrelation. One of them is related to the data processing. Specifically, misalignment of the two SAR images being interfered causes decorrelation. However, this aspect of decorrelation can be minimized with accurate registration and resampling of the secondary image to the reference image.

Spatial decorrelation and temporal decorrelation are the two most significant sources of decorrelation noise. Spatial decorrelation is caused by the changes in imaging geometry. Spatial decorrelation can be further divided into volumetric decorrelation and baseline decorrelation [Gatelli et al., 1994; Li and Goldstein, 1990].

Volumetric decorrelation is caused by a random distribution of the elemental scatterers with the resolution cell. The cumulative backscatter arising from the



propagation and interaction of the signal with the elemental targets located within the resolution cell is dependent on the angle at which the target is imaged. Differences in viewing angle on the two SAR acquisitions results in a change in relative ranges to elemental scatterers within the resolution cell, ultimately resulting in random changes in backscatter response [Zebker and Villasenor, 1992].

Baseline decorrelation is caused by the differential SAR geometry. A change in viewing angle produces a shift in the range frequency spectrum of the secondary image with respect to the range frequency spectrum of the reference image [Gatelli et al., 1994]. The range spectrum shift is a function of perpendicular baseline, radar wavelength, and the slant range to the target and increases with increasing perpendicular baseline. The overlap of the range spectra of the two images is a measure of phase coherence. Large perpendicular baselines produce large shifts in the spectrum resulting in lesser overlap of the image spectra. When the perpendicular baseline equals the critical baseline, there is no overlap of the spectra and results in complete decorrelation [Gatelli et al., 1994]. Special common band pass filters can be used to reduce the spatial decorrelation noise at the cost of reducing the range bandwidth and range resolution. It is intuitive that to produce coherent interferograms, SAR image pairs with short perpendicular baselines should be used.

Temporal decorrelation is caused by changes in backscatter properties of the resolution cell over time. Decorrelation over time is a characteristic of the surface being imaged. The time scales at which a resolution cell decorrelates can vary from a few seconds to a few years. From the perspective of ERS-1 and ERS-2 C-band data, areas where arid and dry conditions occur are suitable for interferometry while heavily vegetated areas tend to decorrelate quickly.

### ***Atmospheric Noise***

Variations in atmospheric conditions over time significantly influences deformation measurements derived from InSAR. As the radar signal traverses the two-way distance between the sensor and target, it passes through various layers of the atmosphere, including the ionosphere and the troposphere. The propagation of the radar signal through these atmospheric layers results in what is referred to as path length excess. Variations in temperature, water vapor content in the troposphere and the TEC in the ionosphere, result in different path length excess on the two SAR acquisitions. The differential path length excess will appear as an apparent change in slant range and contaminate the InSAR measurements. The differential path length excess, also called atmospheric noise, is indistinguishable from the true surface deformation. Also, the magnitude of the atmospheric effects can have a high temporal variability, predominantly due to changes in water vapor distribution in the lower troposphere [Hanssen, 2001]. Presence of atmospheric noise poses problems in detecting, measuring and interpreting real deformation signals.

### ***Noise from Errors in Topography***

The differential interferogram is produced by using a DEM to remove the interferometric phase contribution due to topography. Errors in the DEM, will result in residual topographic phase errors. These errors become significant in cases where perpendicular baselines are large.

### ***Noise from Errors in Satellite Orbits***

Use of incorrect orbit information in locating the satellite will result in an erroneous calculation of the interferometric baseline. Phase noise originating from errors in baseline is spatially correlated and appears as phase ramps across the differential interferogram. These errors are corrected by using the interferometric phase to estimate a refined baseline.

## **2.3 SUMMARY**

This chapter provided the necessary background on SAR imaging principles, image formation, interferometry, and the deduction of surface deformation phase from the interferometric phase. Major limitations and noise sources influencing InSAR analysis were reviewed. Chapter One and Chapter Two are expected to give the reader a detailed background required to understand the problem being addressed as part of this research work.

Chapter Three details the operation and imaging geometry of the ScanSAR mode of data acquisition. SAR imaging concepts explained in this chapter will be helpful in comparing stripmap and ScanSAR modes.

## **CHAPTER THREE**

### **SCANSAR IMAGING AND BURST MODE DATA PROCESSING**

In this chapter the ScanSAR data acquisition geometry and the backscatter signal properties of a target imaged in the SAR burst mode are described. Concepts explained in Chapter Two are utilized to elucidate similarities and differences between stripmap and ScanSAR mode acquisitions and the resulting target response. Also, phase preserving algorithms to process burst mode data are discussed in this chapter. These algorithms produce images for use in interferometry.

#### **3.1 BURST MODE AND SCANSAR MODE DATA**

##### **3.1.1 Burst Mode Data**

As described in Chapter Two, a SAR sensor operating in stripmap mode images targets on the ground by transmitting and receiving SAR signal pulses. The number of pulses that hit a target depends on the time the target is illuminated (azimuth aperture time) and the rate at which the radar transmits pulses (pulse repetition frequency). All the pulses of a stripmap acquisition can be used to obtain SAR images at the intrinsic (maximum possible) azimuth resolution. Such an image is often referred to as a full-resolution image or a single look complex (SLC) image. Each target in an SLC image would have been imaged by the number of pulses that are equivalent to a full-aperture length.

However, to obtain a continuous SAR image, it is not necessary for the SAR sensor to utilize every pulse of the full aperture. In applications where the high resolution obtained from full-aperture processing of the SAR image is not crucial, a subset of the

aperture length can be used to obtain low resolution images [Tomiyasu, 1981]. This was the case on the Magellan mission to Venus in 1990 [Johnson, 1991]. Due to constraints on power requirements for near-simultaneous use of other instruments onboard the satellite, the SAR sensor was designed to operate on a periodic “on-off” basis. As long as there is an overlap between radar beam footprints of consecutive “on” cycles of the SAR sensor, a continuous processed image can be formed. SAR data collected in this manner is called burst mode data, wherein a single burst represents a block of radar pulses that were received continuously. If there are no restrictions on the power requirements and the operation of the SAR sensor, the time between the bursts, i.e. inter-burst time gap, can be used to image in other directions by changing the beam look angle. This type of imaging is termed ScanSAR mode [Moore et al., 1981].

### **3.1.2 ScanSAR Imaging Geometry**

A SAR sensor operating in the ScanSAR mode sensor is able to image multiple strips of land called subswaths from a single satellite pass (Figure 3.1 (A)). The sensor achieves this by electronically steering the radar beam through a set of elevation or look angles. SAR data corresponding to each subswath is collected in the burst mode, wherein the inter-burst gap time corresponds to the time when the sensor is imaging the remaining subswaths. The raw data from each subswath are processed to burst mode images and merged into a composite ScanSAR image.

Many of the current civilian satellite SAR sensors are capable of imaging a wide swath of land using the ScanSAR mode. ScanSAR mode was first used on the NASA SIR-C mission that flew in 1994 [Honeycutt, 1989]. Radarsat-1, Radarsat-2, Envisat, ALOS, COSMO-SkyMed, and TerraSAR-X are currently operating satellite SAR sensors

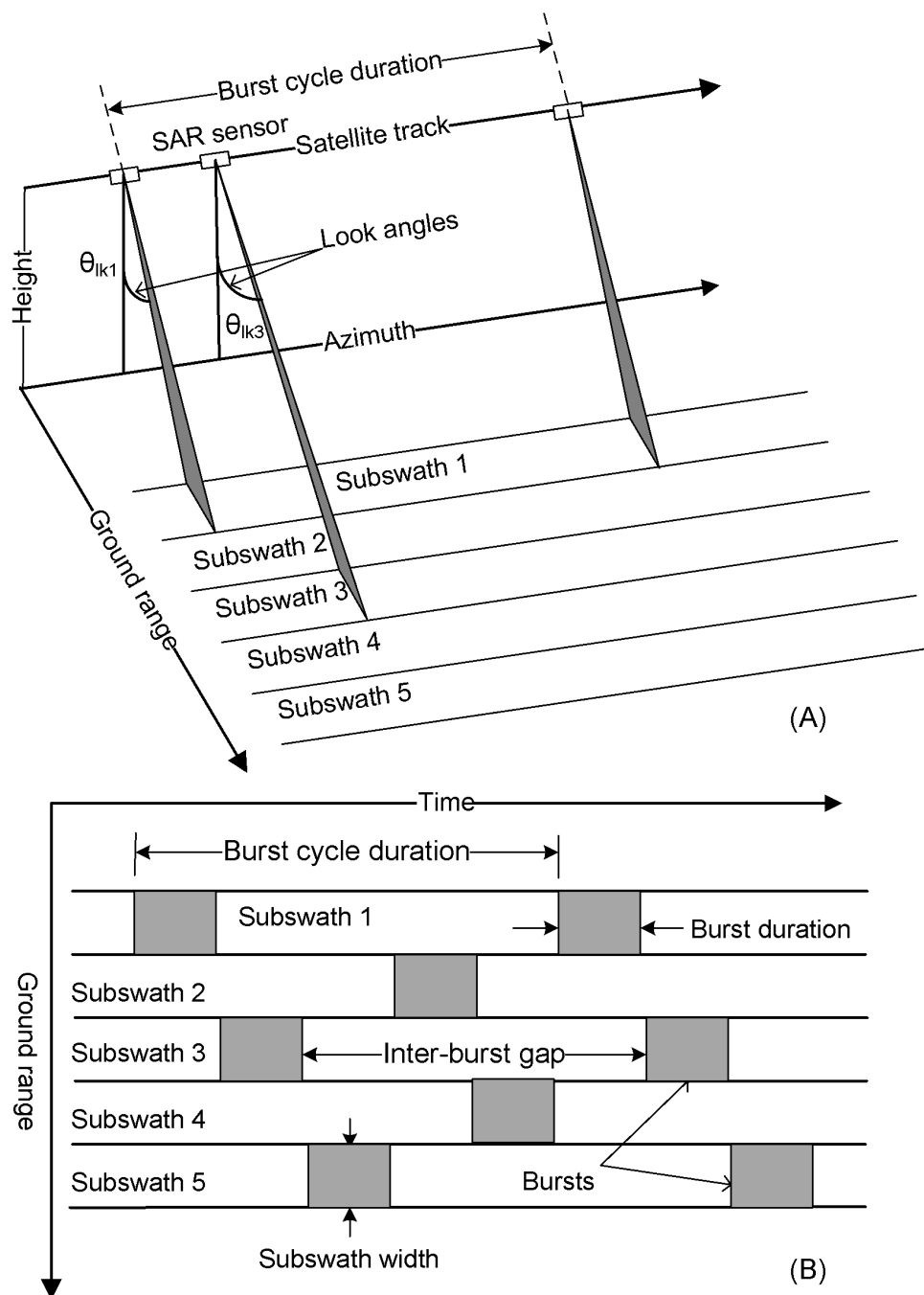


Figure 3.1: A ScanSAR data acquisition scheme. The SAR sensor images 5 subswaths, returning to the same subswath after one burst cycle duration. Parameters such as the burst duration, the inter-burst gap, and the subswath width, can vary from one subswath to another.

capable of imaging in ScanSAR mode. Radarsat-1 has two different ScanSAR modes each with a different number of subswaths (2, 3 or 4 subswaths) [Raney et al., 1991]. On Envisat, the ScanSAR mode is called Wide Swath Mode (WSM) and has 5 subswaths.

The data acquisition pattern of the ScanSAR mode on various SAR sensors is generally the same (Figure 3.1(B)). A SAR sensor operating in the ScanSAR mode acquires bursts of raw data from various subswaths in a cyclic fashion. In the case of Envisat Wide Swath mode, the sensor cycles through subswaths 1, 3, 5, 2, and 4, in that order. The sensor images only one subswath at any given time. Accordingly, while the sensor images a particular subswath (shaded areas in Figure 3.1(B)), there will be data gaps in all the other subswaths that are not being imaged. Although there are temporal data gaps in each subswath, a continuous processed image can still be generated as long as the radar beam footprints of successive bursts have a spatial overlap. The time duration of each burst is called burst length or dwell time. The dwell time of bursts varies from one subswath to another subswath but usually remains constant for the same subswath. The time taken for the sensor to complete one cycle through all the subswaths is called the cycle time. Usually the ScanSAR cycle time is much smaller than the full-aperture time. So each burst can be considered an azimuth look extracted from the full-aperture. The number of effective looks of a ScanSAR subswath can be defined as the number of times a subswath is imaged in the duration of one full-aperture time. The number of effective looks of the ScanSAR mode  $N_{EL}$  can be defined as:

$$N_{EL} = T_A / T_C \quad (3.1)$$

where  $T_A$  is the full-aperture time and  $T_C$  is the cycle time. Typically for the WSM on Envisat, the effective number of looks rounded down to the smaller integer is 3. This

means that every target within a ScanSAR subswath will be imaged by at least 3 consecutive bursts. Since a SAR sensor operating in the ScanSAR mode acquires data in a discontinuous way, i.e. periodic bursts of data, the sensor-target viewing geometries observed in ScanSAR data will also be discontinuous. Compared to the sensor-target viewing angles of a SAR sensor imaging in the stripmap mode, there are large gaps in the set of viewing angles seen in ScanSAR mode (Figures 3.2 (A) and (B)). The gaps in the viewing angles seen in Figure 3.2 (B) correspond to the time when the sensor is imaging other subswaths.

### **3.1.3 Burst Parameters**

In this section, an overview of various burst parameters is given. While all subswaths of the ScanSAR mode acquisition are imaged in a similar way, i.e. as bursts of raw data, each subswath can have a different set of burst parameters. These parameters can be considered as the characteristics of each subswath. The selection of these parameters is mission specific, and some of them critically influence the intrinsic resolution of the SAR images that can be obtained from ScanSAR mode. The three important parameters that determine the resolution of the burst mode images are: the pulse repetition frequency ( $PRF$ ), lines per burst, and SAR chirp bandwidth. All the three parameters can vary from one subswath to another.

The inherent azimuth resolution of the burst mode images of a subswath is linearly dependent on the burst duration or the dwell time of the sensor in that subswath. The dwell time is in turn a function of  $PRF$  and the number of lines per burst.



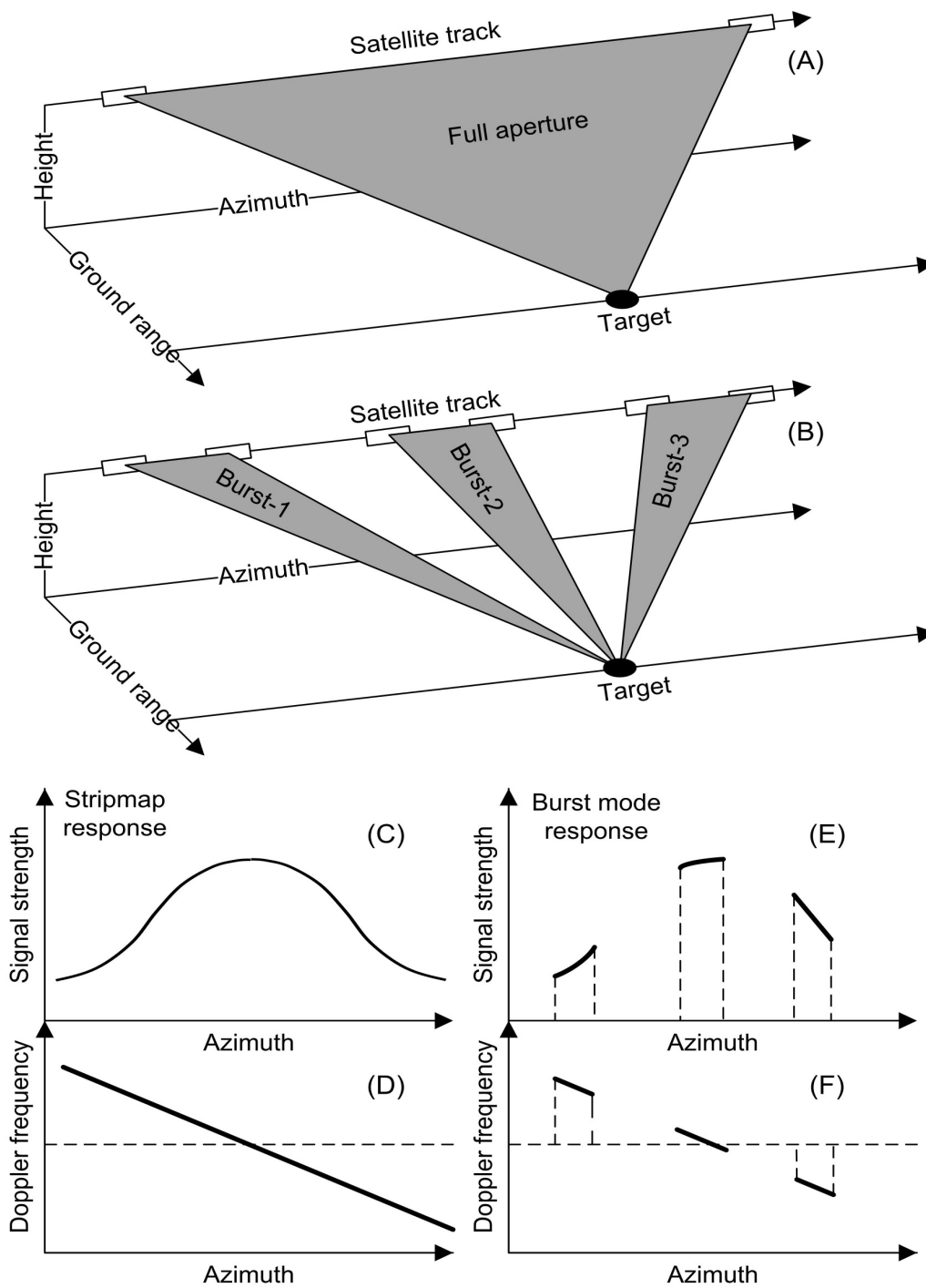


Figure 3.2: A comparison of stripmap and burst mode imaging geometry, azimuth signal strength, and Doppler history for a single target.

The burst duration or dwell time can be related to the number of pulses per burst ( $N_B$ ) and  $PRF$  as follows:

$$T_B = (N_B - 1)/PRF \quad (3.2)$$

where  $T_B$  is the length of the burst in units of time. Consequently, the burst bandwidth ( $W_B$ ) in azimuth direction can be expressed as:

$$W_B = T_B |f_R| \quad (3.3)$$

where  $f_R$  is the Doppler rate. The value of number of lines per bursts ( $N_B$ ) is optimized in such a manner that the azimuth bandwidths of all the subswaths are comparable to each other [Cumming and Wong, 2005]. This is the case with the various subswaths of Envisat WSM (Table 3.1).

The slant range resolution of the various subswaths of the ScanSAR mode depends on the transmitted chirp bandwidth of the SAR signal. On Envisat WSM, each subswath has a different chirp bandwidth that gradually decreases from the near subswath to the far-subswath (Table 3.1). As part of this research work, burst mode data are synthesized from ERS-1 and ERS-2 stripmap data, so corresponding parameters for the ERS-1 and ERS-2 are also given in Table 3.1. Comparison of the chirp bandwidths of the subswaths of the WSM with the IS2 beam stripmap mode on Envisat reveals that stripmap mode data has slightly higher slant range resolution. While the chirp bandwidth of the SS1 subswath is comparable to the Envisat/ERS1-/2 stripmap chirp bandwidths, the chirp bandwidth of SS5 is almost half of the stripmap bandwidth.

Table 3.1: Burst parameters for various subswaths of Envisat WSM (compared to Envisat and ERS stripmap modes).

Parameter\Sensor	ENVISAT Wide Swath Mode Subswaths					Envisat Image Mode (stripmap) IS2	ERS 1 and 2
	SS1	SS2	SS3	SS4	SS5		
Center Frequency (GHz)	5.33	5.33	5.33	5.33	5.33	5.33	5.3
PRF (Hz)	1684.9	2102.4	1692.6	2080.6	1707.0	1652.4	1679.9
Chirp Bandwidth (MHz)	14.75	12.86	10.48	9.54	8.78	16.00	15.55
Burst length (pulses)	50	65	55	71	60	N.A.	N.A.
Mean look angle (Deg.)	19.16	25.24	29.53	32.81	35.63	20.13	20.35
Swath width (km)	106	86	105	86	101	90	89
Mid-swath azimuth bandwidth (Hz)	62.2	61.9	61.9	62.6	61.7	1322	1344

The variations in the look angles for the different subswaths determine the spatial extent and location of the subswaths on the ground. While each subswath is imaged independently, there is usually a small overlap between adjacent subswaths in the slant range direction. This overlap in slant range of subswaths helps in forming a mosaic of all the subswaths into one large ScanSAR image. When processing ScanSAR data, each subswath is processed individually and later the processed subswaths are mosaicked together. Accordingly, processing ScanSAR data is equivalent to processing burst mode data. Before discussing algorithms to process burst mode data, a pertinent discussion of the burst mode data signal properties is presented.

## 3.2 BURST MODE DATA SIGNAL PROPERTIES

### 3.2.1 Range Signal

The properties of the transmitted and received SAR pulses in ScanSAR mode are very similar to those in the stripmap mode. Except for the bandwidth of the SAR pulse,

which changes with subswath, there is no difference in the treatment of the SAR signal in the slant range direction between ScanSAR and stripmap modes. Major differences between burst mode and stripmap mode data arise in the azimuth direction. Differences in azimuth component of the SAR signal can be understood by looking at the Doppler histories of a single target in burst mode data.

### 3.2.2 Doppler History and Azimuth Signal

The Doppler history of a target that is imaged by a sensor operating in the ScanSAR mode is significantly different from the Doppler history obtained from stripmap imaging. Since burst mode data is discontinuous, the Doppler spectrum of a target within a ScanSAR subswath is also discontinuous. In the burst mode data, each burst contains a part of the full Doppler history of the target seen in the stripmap data (See Figures 3.2 (C – F)). Also, the spectrum contained within a single burst is dependent on the position of the target with respect to the position of the burst. That means in burst mode data, targets that are at the same slant range but different azimuth locations will have different Doppler histories. Contrastingly, in stripmap data, all targets that are at the same slant range have the same Doppler history. The dependence of Doppler history of a target on its location relative to the burst location complicates the processing of burst mode data in the azimuth direction.

The azimuth component of the SAR signal from a single burst of data that has already been compressed in range using a range matched filtering process and corrected for range cell migration (i.e. RCMC applied) is derived. As a starting point, the two-dimensional expression for range compressed and range migration corrected SAR signal ( $s(t, \eta)_{cr}$ ) for stripmap data as shown in Equation 2.28 of Chapter Two, is considered here:

$$s_{cr}(t, \eta) \cong A_g(\eta) B_{WR} \text{sinc}[\pi B_{WR}(t - t_{\rho_1})] \times \exp\left\{-j \frac{4\pi \rho_1}{\lambda}\right\} \exp\left\{-j 2\pi \left(\frac{V^2 \eta^2}{\rho_1 \lambda} - \frac{V^2 \eta_0 \eta}{\rho_1 \lambda}\right)\right\} \text{rect}\left[\frac{\eta}{T_A}\right] \quad (3.4)$$

In Equation 3.4 (which is same as Equation 2.26),  $\eta$  is the azimuth time variable and  $\eta = 0$  corresponds to the azimuth time when the target is at the center of the radar beam,  $\eta_0$  is the zero Doppler time of the target,  $\rho_1$  is the slant range to the target at the beam center time,  $t$  is the slant range time variable,  $t_{\rho_1}$  is the two-way slant range time to the target,  $\lambda$  is the wavelength of the radar signal,  $V$  is the satellite velocity,  $B_{WR}$  is the bandwidth of SAR chirp signal,  $T_A$  is the azimuth aperture time and  $A_g(\eta)$  is azimuth antenna gain pattern. The approximation symbol in Equation 3.4 arises from the fact that a parabolic variation of the sensor-target range with azimuth time has been assumed. In reality the sensor-target range variation with azimuth time is hyperbolic. The subscript  $cr$  in  $s_{cr}(t, \eta)$  is to indicate that the signal is already compressed in slant range.

Using the expressions for the Doppler rate ( $f_R = -2V^2/\lambda\rho_1$ ) and the zero Doppler time ( $\eta_0 = -f_{DC}/f_R$ ), Equation 3.4 can be re-written as:

$$s_{cr}(t, \eta) \cong A_g(\eta) B_{WR} \text{sinc}[\pi B_{WR}(t - t_{\rho_1})] \times \exp\{-j 4\pi \rho_1/\lambda\} \exp\{-j \pi (2f_{DC}\eta - f_R \eta^2)\} \text{rect}[\eta/T_A] \quad (3.5)$$

Since the range components of the SAR signal in stripmap and ScanSAR mode are identical, the following treatment concerns only the azimuth components of the signal. So the range signal terms can be ignored. Now, ignoring the slant range signal terms, i.e.  $B_{WR} \text{sinc}[\pi B_{WR}(t - t_{\rho_1})]$  and  $\exp\{-j 4\pi \rho_1/\lambda\}$  in Equation 3.5, the azimuth

component of the two-dimensional SAR signal can be isolated and represented as a one-dimensional signal ( $s_{cr}(\eta)$ ) as:

$$s_{cr}(\eta) \equiv (A_g(\eta)) \exp\{j\pi(f_R\eta^2 - 2f_{DC}\eta)\} \text{rect}[\eta/T_A] \quad (3.6)$$

The length of the rect function in Equation 3.6 indicates that the duration of the azimuth component of the SAR signal is equal to  $T_A$  which is the azimuth aperture length in stripmap data. An equivalent expression, showing the one-dimensional azimuth component of the SAR signal,  $s(\eta)_{bcr}$ , for a target imaged in the burst mode can now be written as:

$$s_{bcr}(\eta) \equiv (A_g(\eta)) \exp\{j\pi(f_R\eta^2 - 2f_{DC}\eta)\} \text{rect}[(\eta - \eta_{BC})/T_B] \quad (3.7)$$

In the above equation,  $\eta$  is the azimuth time variable,  $\eta_{BC}$  is the azimuth time of the center of the burst (subscript  $BC$  in  $\eta_{BC}$  is for burst center), and the last term of Equation 3.7 is a standard rect function which indicates that the length of the signal is equal to the length of the burst ( $T_B$ ). The first term in Equation 3.4,  $A_g(\eta)$ , is the azimuth antenna gain pattern. It is easily noticeable that the only difference in the expressions for the azimuth component of the SAR signal, between stripmap response (Equation 3.6) and the response from a single burst of ScanSAR mode (Equation 3.7) is the length and the location of the signal, i.e. the rect functions. The azimuth component of the SAR signal in the burst mode can be considered as a small portion of the azimuth component of the SAR signal in stripmap mode.

The shortened length of the azimuth component of burst mode signal, relative to the azimuth component of the stripmap signal, complicates the process of azimuth

compression in burst mode data. Complications in the azimuth compression of burst mode signal can be grouped into two main issues: azimuth antenna gain pattern, and azimuth variant Doppler histories.

The azimuth antenna gain pattern is the variation of the SAR signal strength as a function of azimuth time. In the stripmap mode, all targets that are illuminated by the radar and present at the same slant range, are imaged through the complete azimuth antenna pattern, as the satellite passes over them (Figure 3.2 (C)). As a result, the same azimuth antenna gain is applicable to all targets present at a certain range. However, in the case of the burst mode data, the portion of the azimuth antenna pattern through which a target is imaged varies with target azimuth location. In burst mode data, each of the targets that are at the same range but different azimuth locations will have a different antenna gain applied to its response. This azimuth dependent gain results in a periodic amplitude banding or scalloping effect in the ScanSAR image, running in the azimuth direction [Bamler, 1995]. Scalloping does not affect the phase of the final compressed response but does affect its amplitude. However, in applications such as the Persistent Scatterer (PS) InSAR analysis where the amplitude dispersion index is used to identify PS targets, it is necessary to remove the scalloping effect. To negate the effect of scalloping, it is essential to compensate for the antenna beam pattern in burst mode data [Moreira et al., 1996]. Assuming that the antenna beam pattern can be compensated, we can ignore the amplitude factor  $A_g(\eta)$  in Equation 3.7 for subsequent derivations.

Because of the azimuth dependent Doppler histories of targets in burst mode data, a matched filter based azimuth compression of burst mode data is not trivial. In stripmap data, the matched filter length is equal to the azimuth aperture length  $T_A$  and is same for all the targets present at a certain range. A matched filter implementation that is similar to the one in stripmap data case but with a filter length equal to the burst length is not

practical in the case of burst mode data. As mentioned before, in stripmap data, all targets have the same Doppler history and hence, the same azimuth matched filter can be used to compress all targets that are at the same slant range. However, in the case of burst mode data, although all the targets have the same Doppler bandwidths, the center frequency of the Doppler frequency band varies as a function of the target azimuth position. So each target will require a different azimuth matched filter. Such an implementation of matched filtering is not efficient and outweighs the advantage of the computing speed available through the FFT operations [Cumming and Wong, 2005].

To perform a matched filter based azimuth compression of burst mode data, the matched filter has to be extended to length  $T_A$  so that the filter encompasses Doppler histories of all the targets in the burst. The burst data can be padded with zeros to make their length equal to the filter length, and in this way all targets can be compressed in one single step. The matched filter based azimuth compression is a convolution operation between the azimuth component of the SAR signal  $s_{bcr}(\eta)$  and the complex conjugate of the impulse response  $h_A(\eta)$  of the matched filter.

$$s_{bacr}(\eta) = s_{bcr}(\eta) * h_A(\eta) \quad (3.8)$$

Where  $s_{bacr}(\eta)$  is the azimuth compressed response of the azimuth component of the burst mode SAR signal and

$$h_A(\eta) = \exp\{-j\pi f_R \eta^2\} \text{rect}[\eta/T_A] \quad (3.9)$$

The matched filter based azimuth compressed response of a target imaged in burst data can then be written as [Cumming and Wong, 2005]:



$$s_{bacr}(\eta) \equiv W_B \text{sinc}[\pi W_B \eta] \exp\{j\pi f_R \eta \eta_{BC}\} \exp\{-j\pi f_R \eta^2\} \quad (3.10)$$

where  $W_B = f_R T_B$  is the burst bandwidth.

The azimuth compressed response of the burst mode data using a matched filter is compared with the azimuth compressed response of the stripmap data (Equation 2.28).

$$s_{cr}(t, \eta) \equiv B_{WR} \text{sinc}[\pi B_{WR} (t - t_{\rho 1})] \exp\{-j4\pi \rho_1 / \lambda\} B_{WD} \text{sinc}[\pi B_{WD} \eta] \quad (2.28)$$

In the above Equation,  $B_{WR}$  is the range bandwidth and  $B_{WD}$  is the stripmap Doppler bandwidth. Ignoring the range dependent terms, i.e.  $B_{WR} \text{sinc}[\pi B_{WR} (t - t_{\rho 1})]$  and  $\exp\{-j4\pi \rho_1 / \lambda\}$ , in Equation 2.28, the azimuth component of the azimuth compressed stripmap SAR signal can be written as:

$$s_{cr}(\eta) \equiv B_{WD} \text{sinc}[\pi B_{WD} \eta] \quad (3.11)$$

Comparison of the Equation 3.10 with the azimuth compressed response of the stripmap data in Equation 3.11, reveals that there are two additional phase terms in the azimuth compressed response of the burst mode data. The last term in Equation 3.10 is a quadratic phase term caused by the use of a matched filter that is longer than the burst length [Cumming and Wong, 2005]. The quadratic phase term is the same for all targets. In addition to the quadratic phase term, there is a linear phase term whose slope is dependent on the relative position of the target beam center time with respect to the burst center time  $\eta_{BC}$ .

In this section the compressed response of a target where the burst mode data is processed using the matched filtering technique is shown. Use of the Range Doppler

Algorithm (RDA) to process one burst at a time is not very efficient as each burst has to be zero-padded to the length of  $T_A$ . Also, the processed burst will be highly oversampled compared to the expected resolution of burst mode data. The next section discusses several algorithms that have been proposed for processing burst-mode data, especially in the case of low squint angles.

### 3.3 BURST MODE DATA PROCESSING

In this section, SAR data processing algorithms available in the literature for ScanSAR data processing are discussed. The major difference between stripmap data and burst mode data is in the azimuth direction, so existing range compression algorithms for stripmap data can be used for burst mode data range processing as well. Since range processing can be considered independent of azimuth processing, range compression of all the bursts can be carried out together by disabling the azimuth processing steps in stripmap processors. Such an algorithm is referred to as a “Pack and Go Algorithm” [Holzner and Bamler, 2002]. Existing stripmap algorithms can also be used in the so-called full-aperture processing of burst mode data. Alternatively, computationally efficient algorithms that are particularly suitable for processing low resolution data can be used for ScanSAR data processing. Presented in this section are descriptions of three algorithms. First, a brief review of the full-aperture processing method is presented elucidating the advantages and the drawbacks associated with the use of existing stripmap processing methods. Then, detailed descriptions of the SPECAN and the modified SPECAN algorithms are given. For this research, I utilize the modified SPECAN algorithm to process burst mode data which is discussed the last.

### **3.3.1 Full-Aperture Processing with Zero-Padding**

Full-aperture processing of burst mode data refers to a method where the inter-burst gaps are filled with zeros [Bamler, 1995; Bamler and Eineder, 1996]. In this way, burst mode data would resemble stripmap data with blocks of data have been deliberately set to zero. If the inter-burst gap is not an integer multiple of the original pulse repetition interval, then the burst data have to be re-sampled to a new interval such that the inter-burst gaps now correspond to an integer number of raw data samples. After filling the gaps with zeroed lines, the entire subswath can be processed as a stripmap image in range, as well as in azimuth. Full-aperture processing has the advantage that any of the existing stripmap processors can be used. However, its processing efficiency is very low because a large amount of zero-padded lines have to be processed and an additional re-sampling step may be needed.

Coherent azimuth processing of multiple bursts using full-aperture processing method preserves the compressed target phase information, but the processed image suffers from amplitude modulation artifacts as noted in Bamler and Eineder [1996]. These artifacts are caused by the periodic nature of the impulse response when multiple bursts are processed simultaneously. These modulation effects can be reduced by using an incoherent low-pass azimuth filter [Bamler and Eineder, 1996]. A more efficient way of processing burst mode data, which is one burst at a time, is presented in the SPECTral ANalysis (SPECAN) method.

### **3.3.2 SPECAN algorithm**

The SPECAN algorithm is more efficient than the RD algorithm for processing low-squint SAR data when moderate to low resolution images are required [Cumming and Wong, 2005]. The origins of the SPECAN algorithm are embedded in the concepts of stretch and step transform methods for processing linear FM signals [Caputi, 1971].

MacDonald Dettwiler (MDA) and the European Space Technology Center (ESTEC) are credited with the first real time implementation of the SPECAN algorithm in 1979 [Cumming and Lim, 1981]. The SPECAN algorithm was historically used for processing burst mode data from the Megallan mission to Venus [Leung et al., 1992], ScanSAR data from SIR-C [Chang et al., 1996], and Radarsat ScanSAR data [Leung et al., 1996].

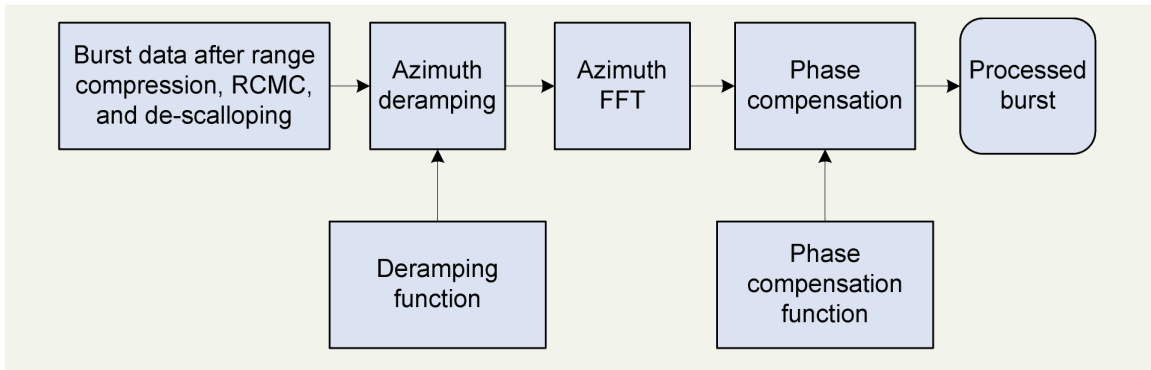


Figure 3.3: Block diagram of the SPECAN algorithm (Adapted from Cumming and Wong [2005]).

A detailed explanation of the SPECAN algorithm (Figure 3.3) is provided here, which will be useful in understanding the Modified SPECAN algorithm discussed later in the chapter. The central idea of the SPECAN algorithm is a “deramping” operation that converts the linear FM characteristics of the SAR azimuth component of the SAR signal to a sine wave of a single frequency. This is followed by a Discrete Fourier Transform (DFT) operation implemented using Fast Fourier Transforms (FFT) algorithms, that compresses the signal by registering the targets to their appropriate frequency bins. After the FFT operation, even though the signal is in the frequency domain, the Fourier frequency bins can be associated with azimuth time based on a relation between Fourier frequency and azimuth time and Doppler rate [Cumming and Wong, 2005]. Since the Doppler rate is a function of the slant range, the relation between Fourier frequency and

azimuth time varies as a function of slant range. This will result in a processed image where the output sample spacing varies with slant range. If required, an interpolation process, which is not a part of the SPECAN algorithm, has to be carried out to place the compressed response of the targets on an evenly spaced grid. If implemented, this interpolation step negates the efficiency gained from the SPECAN algorithm. The derivation of the azimuth compressed response using the SPECAN algorithm is provided in the next section.

Consider the azimuth component of the SAR signal of a target imaged by a sensor through a single burst, i.e. Equation 3.7 (re-produced here for convenience):

$$s_{bcr}(\eta) \equiv (A_g(\eta)) \exp\{j\pi(f_R\eta^2 - 2f_{DC}\eta)\} \text{rect}[(\eta - \eta_{BC})/T_B] \quad (3.7)$$

For simplification, the reference time of the signal is chosen to be the start of the burst instead of the beam center time (Figure 3.4) and a zero-Doppler geometry has been assumed ( $f_{DC}=0$ ). Also the antenna gain term  $A_g(\eta)$  is dropped assuming that antenna gain pattern has been compensated. If the zero-Doppler time of the target is  $u_0$ , and the azimuth time variable with respect to the burst start time is  $u$ , then the azimuth component of the SAR signal can be represented as:

$$s_{bcr}(u) = \exp\{j\pi f_R(u - u_0)^2\} \text{rect}[(u - T_B/2)/T_B] \quad (3.12)$$

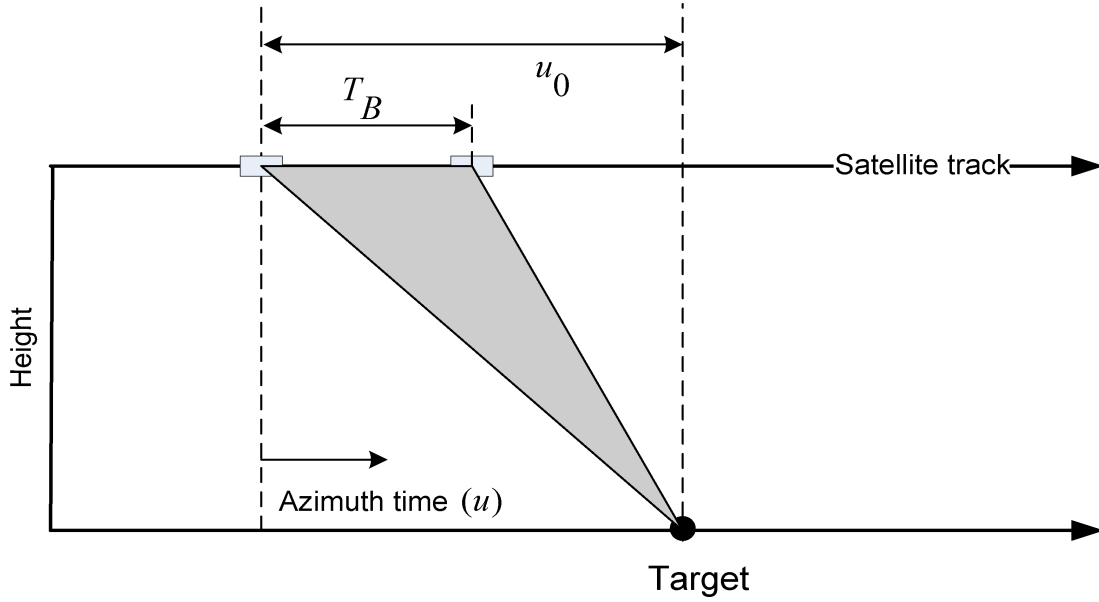


Figure 3.4: A sketch showing 2-D projection of sensor-target imaging geometry for a single burst. The shaded area indicates the set of satellite to target lines of sight projected into the vertical plane containing the satellite track.

Equation 3.12 can be obtained from Equation 3.7, by dropping  $A_g(\eta)$  and by making substitutions for change of variables as  $\eta = u - u_0$  and  $\eta_{BC} = -u_0 + T_B/2$ .

The deramping function ( $h_{drmp}$ ) that will remove the quadratic phase term from Equation 3.12 is given as:

$$h_{drmp}(u) = \exp\{-j\pi f_R u^2\} \text{rect}[(u - T_B/2)/T_B] \quad (3.13)$$

Multiplying Equation 3.12 with Equation 3.13, the deramped signal,  $s_{drmp}$ , is obtained as:

$$s_{drmp}(u) = \exp\{j\pi f_R u_0^2\} \exp\{-j2\pi f_R u_0 u\} \text{rect}[(u - T_B/2)/T_B] \quad (3.14)$$

In the deramped signal  $s_{drmp}$ , the first term is a constant phase term whose phase is proportional to the square of the target zero-Doppler time with respect to the burst start time. The second term is a complex sinusoid whose frequency is equal to  $(-f_R u_0)$ . Taking a Fourier transform of the deramped signal, the compressed response  $s_{comp}(\xi)$  in the azimuth frequency ( $\xi$ ) domain is given as:

$$\begin{aligned}
s_{comp}(\xi) &= \int s_{drmp}(u) \exp\{-j2\pi\xi u\} du \\
&= \exp\{j\pi f_R u_0^2\} \int \text{rect}\left[\frac{u - T_B/2}{T_B}\right] \exp\{-j2\pi f_R u_0 u\} \exp\{-j2\pi\xi u\} du \\
&= \exp\{j\pi f_R u_0^2\} \exp\{-j\pi T_B(\xi + f_R u_0)\} T_B \text{sinc}[\pi T_B(\xi + f_R u_0)]
\end{aligned} \tag{3.15}$$

The peak of the compressed response is at the azimuth frequency  $\xi = -f_R u_0$ .

There is an ambiguity here about the concept of frequency domain and time domain, as even after performing an FFT operation, the data is still in the “time” domain. This ambiguity can be explained using the fact that the Fourier frequency, to which a target gets compressed, is linearly related to the target location in the time domain via the Doppler rate, i.e.  $\xi = -f_R \bar{\xi}$ , where  $\bar{\xi}$  is the azimuth time after compression. Using this linear relation between the Fourier frequency and azimuth time, Equation 3.15 can be re-written in terms of azimuth time variable  $\bar{\xi}$  as:

$$s_{comp}(\bar{\xi}) = \exp\{j\pi f_R u_0^2\} \exp\{-j\pi f_R T_B(\bar{\xi} - u_0)\} T_B \text{sinc}[\pi f_R T_B(\bar{\xi} - u_0)] \tag{3.16}$$

In the above equation, note that the target is compressed to its zero-Doppler time, i.e. the peak of the sinc function is at  $\bar{\xi} = u_0$ . The constant phase term (first term on the right-

hand side of Equation 3.16) indicates that the peak phase of the compressed response of a target is dependent on the target azimuth location with respect to the start of the burst.

The last step of the SPECAN algorithm is the phase compensation process which is done compensate the quadratic phase term (first term in Equation 3.16) dependent on relative location of the target with respect to the burst. The phase compensation is a quadratic function of azimuth time. The compressed response after phase compensation,  $s_{cm}$ , can be written as:

$$s_{cm}(\bar{\xi} - u_0) = \exp\left\{-j\pi f_R(\bar{\xi} - u_0)^2\right\} \exp\left\{j\pi f_R T_B(\bar{\xi} - u_0)\right\} T_B \text{sinc}\left[\pi W_B(\bar{\xi} - u_0)\right] \quad (3.17)$$

where  $W_B = f_R T_B$  is the bandwidth of the burst. Equation 3.17 is the compressed target response obtained from SPECAN algorithm for a zero-Doppler case. After phase compensation, the azimuth component of the compressed SAR response has zero phase at the peak of the response, i.e. at  $\bar{\xi} = u_0$ .

If the discrete form of Equation 3.17 is considered, then the pixel spacing is determined by the spacing between frequency bins of the FFT. If the original SAR signal is sampled at the PRF in the azimuth direction, then the frequency bin spacing after an FFT operation is  $PRF/(N_{FFT} - 1)$ , where  $N_{FFT}$  is the length of the FFT used. Then the azimuth sample spacing ( $\Delta\bar{\xi}$ ) after FFT is:

$$\Delta\bar{\xi} = \left| \frac{\Delta\xi}{f_R} \right| = \left| \frac{PRF}{(N_{FFT} - 1)f_R} \right| \quad (3.18)$$

where  $\Delta\xi$  is FFT frequency bin spacing. From Equation 3.18, it is clear that the sample spacing is inversely proportional to the Doppler rate. However, the Doppler rate is again



inversely proportional to the slant range ( $f_R = -2V^2/\lambda\rho_1$ ). So it can be said that the sample spacing is directly proportional, and varies linearly, with slant range.

Although SPECAN is an efficient algorithm compared to the Range Doppler algorithm, it suffers from a disadvantage of having range dependent output sample spacing. If an equally spaced sample spacing of the output is desired, an interpolation process is required which is not insignificant in terms of computational efficiency. To address the limitation of the SPECAN algorithm, a less efficient method called the modified SPECAN algorithm was developed [Lanari et al., 1998].

### 3.3.2 Modified SPECAN algorithm

The modified SPECAN algorithm (Figure 3.5) overcomes the pixel spacing constraints of the SPECAN algorithm in an elegant way. The modified SPECAN algorithm (Figure 3.5) uses the Scaled Fourier Transform (SCFT) instead of the standard Fourier transform [Cumming and Wong, 2005]. The SCFT operation can be implemented using the Chirp-Z Transform [Cumming and Wong, 2005; Rabiner et al., 1969]. The modified SPECAN algorithm was utilized to process burst mode data as part of this research work. This section explains the algorithm in detail.

The first step of the modified SPECAN algorithm is a deramping step, identical to the one performed in the SPECAN algorithm. As in the case of the SPECAN algorithm, it is assumed that the burst data has been range compressed and corrected for range migration. Consider the same expression for the azimuth component of the SAR signal of a target in burst mode data as was considered in the derivation of the SPECAN method (Equation 3.6). The deramped signal is then the same as that in SPECAN (Equation 3.8).

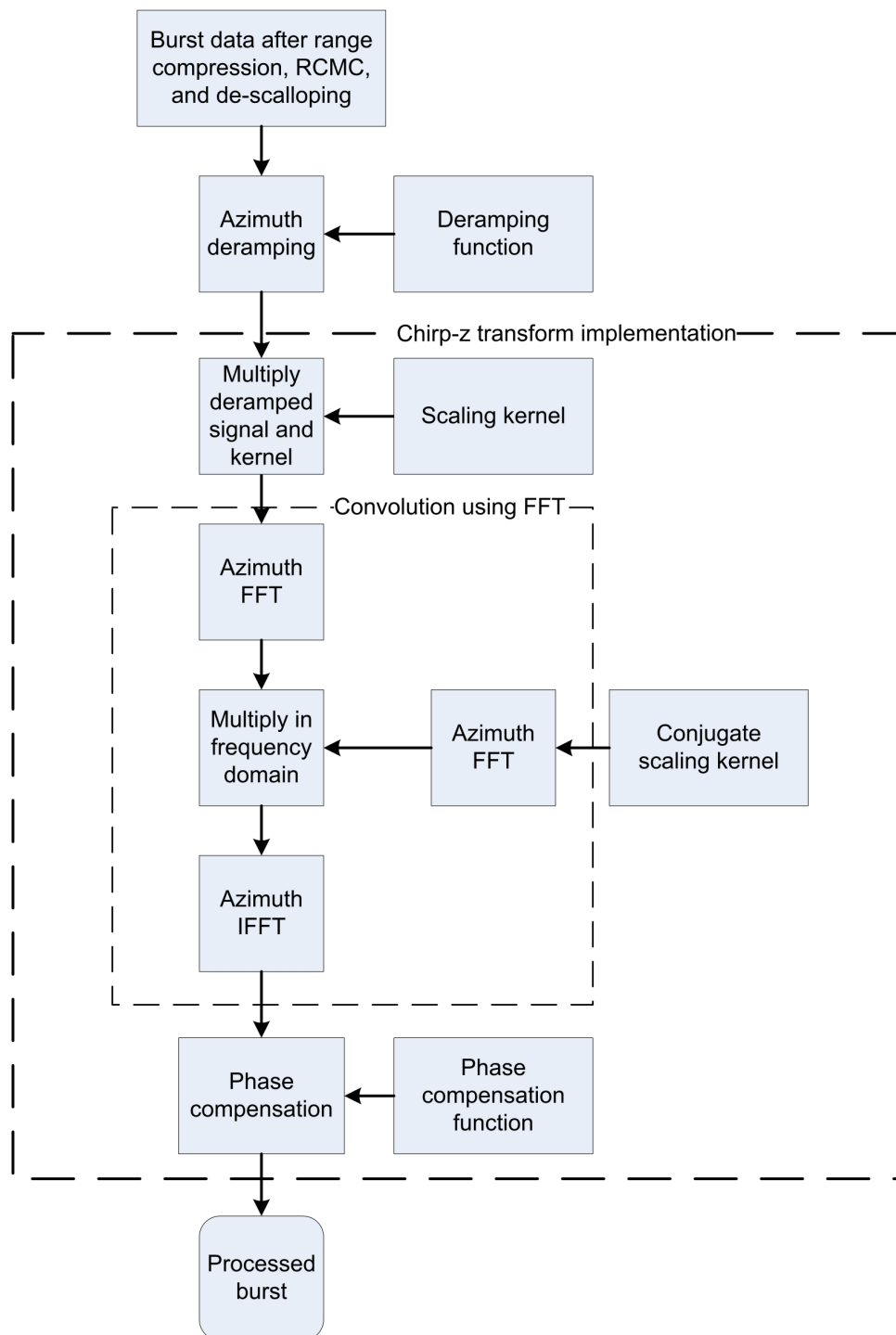


Figure 3.5: Block diagram of the Modified SPECAN algorithm (adapted from Lanari et al. [1998]).

The compressed response,  $s_{comp}(\xi)$ , derived from the SCFT operation of the modified SPECAN algorithm can be written as [Cumming and Wong, 2005]:

$$s_{comp}(\xi) = \exp\{j\pi f_R u_0^2\} \int_{-T_B/2}^{T_B/2} \exp\{-j2\pi f_R u_0 u\} \exp\{-j2\pi \beta_r \xi u\} du \quad (3.19)$$

where  $\beta_r$  is a unitless scaling factor which is the ratio of a fixed reference slant range  $r_0$  and the beam center slant range of the target  $\rho_1$ :

$$\beta_r = r_0 / \rho_1 \quad (3.20)$$

The final output spacing of the compressed response is dependent on the scaling factor which in turn is dependent on the fixed reference slant range. The reference slant range can be chosen so as to obtain desired output sample spacing.

The evaluation of the integration in Equation 3.19 gives the compressed response as:

$$s_{comp}(\xi) = \exp\{j\pi f_R u_0^2\} \exp\{-j\pi T_B (\beta_r \xi + f_R u_0)\} T_B \text{sinc}[T_B (\beta_r \xi + f_R u_0)] \quad (3.21)$$

Unlike in the SPECAN algorithm, the discrete frequency bin spacing in the modified SPECAN algorithm is independent of slant range. The slant range dependence of sample spacing caused by the Doppler rate is cancelled by the range dependent scaling factor  $\beta_r$ .

The sample sampling  $\Delta\bar{\xi}$  after the Scaled Fourier Transform operation is:

$$\Delta\bar{\xi} = \left| \frac{\beta_r \Delta\xi}{f_R} \right| = \left| \frac{r_0}{\rho_1 (N_{FFT} - 1) f_R} \right| \quad (3.22)$$

The choice of the fixed reference slant range  $r_0$  in Equation 3.22 is arbitrary. Thus, depending on the desired output spacing, the fixed reference slant range can be chosen. The final step of the modified SPECAN algorithm, similar to the SPECAN algorithm, is the phase compensation operation which makes the peak phase of the compressed response equal to zero.

The Chirp-Z Transform (CZT) can be utilized to perform the integration in Equation 3.19 in its discrete form. The derivation of the CZT and its implementation are discussed in Appendix A. The application of CZT to process burst mode data, starting from the discrete form of the deramped azimuth component of the SAR signal, is discussed here. For simplicity, assume that the target is located in the azimuth sample number  $q_0$  with respect to the first sample of the burst data, i.e. the target azimuth time with respect to the first sample of burst data is  $u_0 = q_0 / PRF$ . Similarly, the discrete azimuth sample variable and its azimuth time with respect to the first sample of the burst are  $q$  and  $q/PRF$ , respectively. Then, the discrete form of the deramped azimuth component of the SAR signal (Equation 3.14) with  $N_B$  samples is:

$$s_{drmp}(q) = \exp\left\{j\pi \frac{f_R}{PRF^2} q_0^2\right\} \exp\left\{-j2\pi \frac{f_R}{PRF^2} q_0 q\right\} \text{rect}\left[\frac{(q - N_B/2)}{N_B}\right],$$

$$q = 0, N_B - 1 \quad (3.23)$$

Now, consider the CZT of the deramped signal with the angular spacing between the complex numbers set to:

$$\Delta\phi = 2\pi \frac{f_R}{PRF^2} \beta \quad (3.24)$$

where  $\beta$  is called the pixel spacing factor. The pixel spacing factor  $\beta$ , similar to the spacing factor  $\beta_r$  defined earlier in Equation 3.20, can be arbitrarily chosen to obtain the desired final output spacing of the processed image. While the values of  $\beta_r$  were dependent on the selection of an arbitrary reference slant range, the pixel spacing factor used in the CZT implementation can be chosen directly. Plugging Equation 3.24 into the expression for the CZT (refer Appendix A), we can write the  $k^{th}$  sample of the CZT of the deramped signal as:

$$\begin{aligned} CZT_{Sdrmp(q)}[k] &= \sum_{q=0}^{N_B-1} \left[ s_{drmp}(q) \exp \left\{ -j\pi \frac{f_R}{PRF^2} \beta q k \right\} \right] \\ &= \exp \left\{ -j\pi \beta \frac{f_R}{PRF^2} k^2 \right\} \times \\ &\quad \left[ \sum_{q=0}^{N_B-1} s_{drmp}(q) \exp \left\{ -j\pi \frac{f_R}{PRF^2} \beta q^2 \right\} \right] \exp \left\{ j\pi \frac{f_R}{PRF^2} \beta (k-q)^2 \right\} \end{aligned} \quad (3.25)$$

The compressed response after the convolution operation and the phase compensation step of CZT can be written as:

$$\begin{aligned} s_{comp}[k] &= \exp \left\{ -j\pi \frac{f_R}{PRF^2} q_0^2 \right\} \exp \left\{ -j\pi \frac{\beta f_R}{PRF^2} H_{BL} \left( k - \frac{q_0}{\beta} \right) \right\} \times \\ &\quad W_B \operatorname{sinc} \left[ \beta W_B \left( k - \frac{q_0}{\beta} \right) \right] \end{aligned} \quad (3.26)$$

where  $H_{BL}$  is the pixel number corresponding to the center pixel of the burst, defined as:

$$H_{BL} = N_B/2 - 1 \quad \text{if } N_B \text{ is even} \quad (3.27a)$$

$$H_{BL} = (N_B - 1)/2 \quad \text{if } N_B \text{ is odd} \quad (3.27b)$$

The characteristics of the discrete form of the compressed response obtained from the modified SPECAN algorithm (Equation 3.26) are dependent on the chosen processing parameters. For example, the number of samples in the compressed response or the output length of the CZT is dictated by the length of the FFT used in the convolution. Unlike the SPECAN algorithm, the sample spacing is not a function of the Doppler rate. The azimuth sample to which a target is compressed can be controlled by the pixel spacing factor ( $\beta$ ). If  $\beta = 1$ , then the sample spacing of the original data ( $1/PRF$ ) is maintained, and the target gets compressed to its zero-Doppler azimuth location of  $q_0$ . With the value of  $\beta$  set to 1.0 to compress all the targets contained within the burst, the length of the FFT should be equal to the full aperture length.

However, if a pixel spacing factor of 2 is used, then the target gets compressed to the pixel location of  $k = q_0/2$ . Similarly, all the other targets contained in the burst are also compressed to locations corresponding to half the distance to their true location. So, a pixel spacing factor of 2 is equivalent to under sampling the output response by a factor of 2. In such a case, the required FFT length to compress all the targets contained in a burst will be half of the aperture length. There are other advantages of the pixel spacing factor. First, the output sample spacing can be increased to a value that is close to the expected resolution from the burst image. Typically Envisat WSM ScanSAR images have a resolution that is 20 times coarser than their stripmap image resolution. In such a case, a pixel spacing factor of 20 would keep the output spacing of the ScanSAR image comparable to its ScanSAR resolution. This will help avoid oversampling of the data.

Another advantage of the pixel spacing factor is that the output spacing can be adjusted so as to make the inter-burst gap time an integer multiple of the spacing. This way the processed bursts can be aligned and mosaicked together without further interpolation. Also, the spacing factor has been used in controlling pixel spacing of burst mode SAR data for ScanSAR-stripmap interferometric purposes [Ortiz and Zebker, 2007]. In the case of Envisat, where the stripmap data and the ScanSAR data are acquired at different PRF, the processed stripmap and ScanSAR images can be placed on a common output grid before being interfered [Ortiz and Zebker, 2007].

This concludes the discussion on burst mode data processing. Following is a brief summary of the topics discussed in this chapter.

### **3.4 SUMMARY**

This chapter provided an overview of ScanSAR mode imaging and the concept of burst mode data. The Doppler history and azimuth signal properties of burst mode SAR data were described and compared with stripmap mode data. A summary of the phase preserving algorithms used to process burst mode data was provided. Also, the SPECAN and the modified SPECAN algorithms were explained in detail.

Chapter Four considers differential interferometry using burst mode data and demonstrates its effectiveness as a deformation monitoring tool. Burst alignment, a necessary condition for burst mode interferometry, and other factors that influence interferometric phase coherence in burst mode are explained in the next chapter.

## **CHAPTER FOUR**

### **DIFFERENTIAL INTERFEROMETRY AND DEFORMATION TIME SERIES GENERATION USING SCANSAR DATA**

In this chapter, results pertaining to the application of the Small Baseline Subset (SBAS) technique to a database of ScanSAR interferograms are presented. Time series of surface deformation maps showing the temporal evolution of land subsidence in Phoenix, Arizona are generated from ScanSAR interferograms simulated from stripmap ERS-1 and ERS-2 data. It has been demonstrated that, in arid regions which are conducive for interferometry, repeat-pass InSAR using ScanSAR data with reasonable burst overlap can be utilized to monitor ground surface deformations. Also, as part of researching the viability of ScanSAR interferometry for monitoring purposes, the effect of the so-called burst overlap or burst synchronization on interferometric is investigated.

This chapter is organized as follows. First, a brief background of ScanSAR interferometry is given including an explanation of the concept of the so-called burst overlap. Results elucidating the effect of burst overlap on interferometric phase coherence are presented in Section 4.2. The methodology of ScanSAR interferogram formation, the SBAS technique, and its application to this research are presented in Section 4.3. Next, time series results and their validation are discussed in section 4.4 followed by some conclusions in Section 4.5.



## 4.1 BACKGROUND ON SCANSAR INTERFEROMETRY

The use of ScanSAR data for InSAR has been previously demonstrated in the literature. Guarnieri et al. [1995] show the proof of the concept of ScanSAR interferometry using burst mode datasets that were simulated from ERS-1 and ERS-2 stripmap data. Bamler et al. [1999] are credited with one of the first studies to show interferometry results using actual ScanSAR data collected from Radarsat-1. ScanSAR interferometry was also the basis for the Shuttle Radar Topography Mission (SRTM) launched in February 2000 that mapped the topography of almost the entire Earth's surface [Farr et. al, 2007]. Initial ScanSAR interferometry results using data collected from the Envisat Wide Swath Mode were shown by Guarnieri et al. [2003] and Guccione [2006].

ScanSAR interferometry has been demonstrated but thus far its use for differential interferometry has been infrequent and virtually unexplored for InSAR time series analysis. Although ScanSAR modes have been operational on some of the current SAR satellites for over half a decade (Envisat) or more (Radarsat-1), the development of phase-preserving processing algorithms for ScanSAR data lagged behind the data acquisitions. The reason for the lag was that ScanSAR mode was initially intended for radiometric purposes [Holzner and Bamler, 2002]. Further, to form an interferogram with two ScanSAR scenes, it is necessary to have sufficient burst overlap between the two scenes [Guarnieri and Prati, 1996]. The concept of the burst overlap, or burst *synchronization*, is explained below. The lack of ScanSAR data with adequate burst synchronization has been a limiting factor in the use of ScanSAR data for differential interferometry.

Burst synchronization can be defined as the overlap of the Doppler spectra of the targets contained in the two bursts that are interfered. The Doppler spectrum is

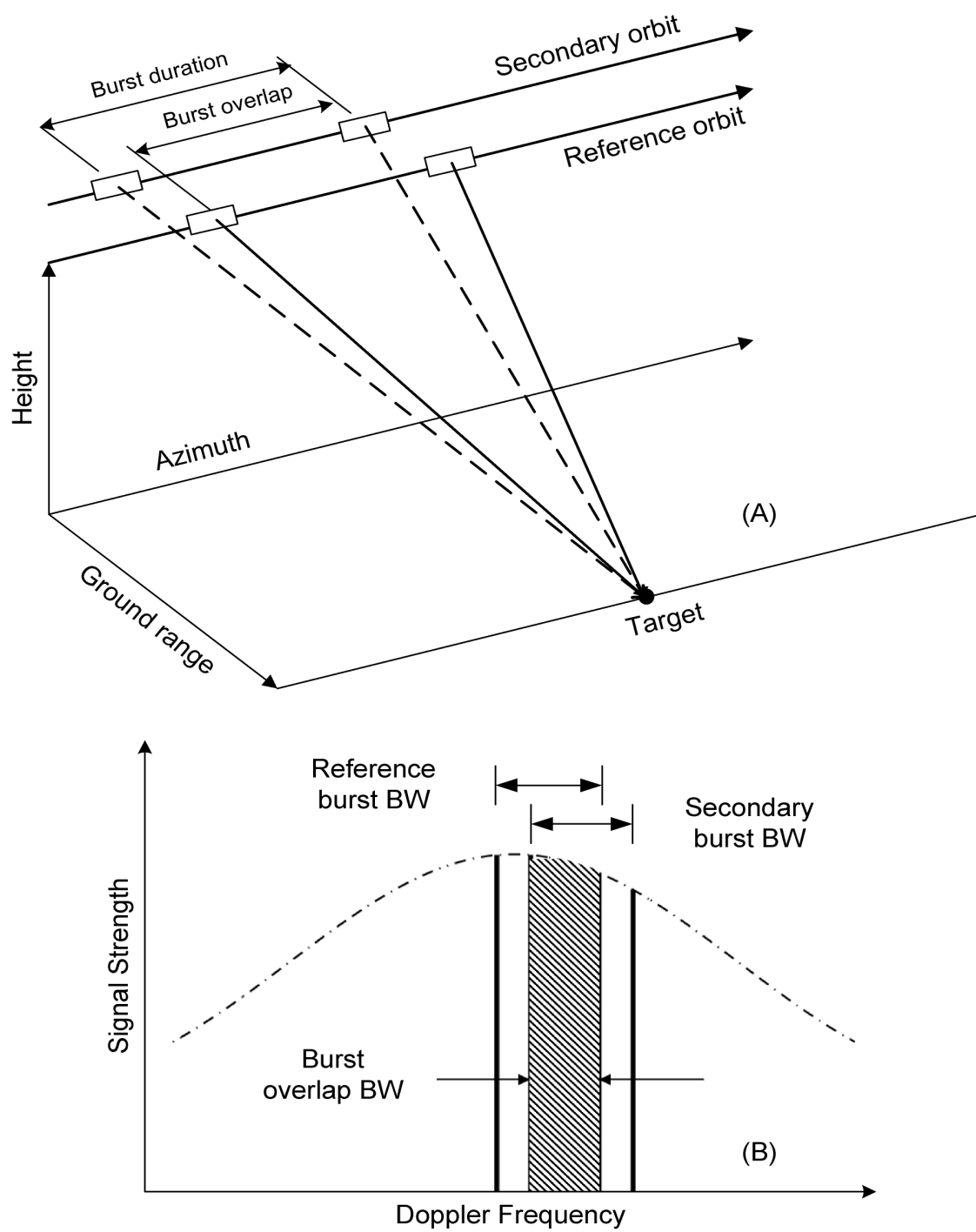


Figure 4.1: Repeat-pass imaging geometry in burst mode SAR. (B) Burst Doppler response of a target relative to the full-aperture Doppler bandwidth.

determined from the set of azimuth viewing angles (Figure 4.1 (A)) through which a target is imaged. To obtain a coherent interferometric phase response, the Doppler spectra of the reference and secondary acquisitions must overlap (Figure 4.1-B). This means that the target should be imaged from overlapping sets of viewing angles on the two acquisitions. Although the burst duration and, consequently, the bandwidth of the bursts of data on the two acquisitions is the same, only the overlapping portion of the spectra contributes to a meaningful interferometric phase. So the effective interferometric burst bandwidth is determined by the amount of burst overlap. More burst overlap leads to higher interferometric bandwidth and consequently, results in higher spatial resolution of the interferometric phase in the azimuth direction. Burst overlap is also referred to as burst alignment and often expressed as a percentage of the burst length. The opposite of burst alignment is called burst misalignment, which is the offset between the two bursts.

The requirement to have common Doppler spectra between reference and secondary SAR images is not confined to ScanSAR interferometry. Even in the case of interferometry with stripmap SAR data, only the overlapping portions of the Doppler spectra contribute to the coherent interferometric phase. The difference in the Doppler centroid frequency of the two acquisitions determines the extent of the overlap of the stripmap Doppler spectra. However, the difference in the Doppler centroid frequency of SAR data collected from the same sensor is usually small compared to the full-aperture Doppler bandwidth seen in stripmap data. Thus, the problem of Doppler spectra alignment is not a major limitation in stripmap interferometry.

Good burst alignment in ScanSAR data can be obtained only through active planning by satellite operators. For example, early Envisat operations with minimal planning for repeatable ScanSAR acquisitions resulted in only a 10% probability of having at least 65% burst overlap and a 20% probability of having at least 30% burst

overlap [Rosich et al., 2007]. However, a new beam synchronization strategy implemented in September 2006 has improved the prospects of performing ScanSAR-ScanSAR repeat-pass interferometry with Envisat data. The probability of having at least 50% burst overlap between two Envisat ScanSAR acquisitions is now 90%. Also, the probability that there will be at least 80% burst overlap between ScanSAR datasets is now approximately 50% [Rosich et al., 2007]. In addition, modifications in Envisat orbit control implemented in January 2007 are now producing orbits with baselines that are more conducive for interferometry [Rosich et al., 2007].

Although satellite SAR operators are now providing ScanSAR images of potential use in radar interferometry studies, there has not been an investigation of the performance one might expect from a ScanSAR interferometry analysis. The rest of this chapter evaluates the effectiveness of ScanSAR-ScanSAR interferometry for measuring deformation.

## **4.2 EFFECT OF BURST OVERLAP ON PHASE COHERENCE**

The quality of the phase in a ScanSAR interferogram depends on the amount of burst overlap between the reference and secondary ScanSAR images. For this reason, it is important to quantify the minimum amount of burst overlap that is needed to measure the interferometric phase with reasonable accuracy. Throughout this research, the accuracy of ScanSAR interferometric phase is evaluated in relation to stripmap interferometric phase. This section presents the results of an experiment that qualitatively and quantitatively measures the amount of interferometric phase noise as a function of burst overlap. In the experiment, differential interferometric phase maps obtained from a stripmap interferogram are compared to ScanSAR interferograms simulated from the same pair of stripmap SAR images. ScanSAR interferograms are generated with varying amounts of

burst overlap percentage between the simulated reference and secondary ScanSAR images. For each burst overlap percentage, profiles through the unwrapped differential interferometric phase of ScanSAR interferograms are plotted and compared to the corresponding profile through the stripmap interferogram. The effect of burst overlap on phase noise is evaluated for different study sites that vary in terms of the scale of the deformation and the phenomenon causing it. First, results pertaining to the main study site, Phoenix, are presented.

#### **4.2.1 Primary Study Site: Phoenix, Arizona**

The aforementioned experiment is implemented for an interferogram over the Phoenix study site using a pair of ERS-2 images. A 9-month interferogram spanning the time period between March 15, 1999 (reference image) and December 20, 1999 (secondary image) and having a perpendicular baseline of 150 meters is considered. The observed surface deformation is land subsidence resulting from aquifer compaction caused by excessive groundwater withdrawal (Figure 4.2). Surface deformation features in the cities of Peoria to the west and Glendale to the east can be clearly identified from the interferogram. The multi-looked interferogram was formed with ten looks taken in the azimuth direction and two looks taken in the range direction. Further, an adaptive spatial filter [Goldstein and Werner, 1998] of window size  $64 \times 64$  and a filter weight of 1.0 was applied before unwrapping the phase. Later, this stripmap differential interferometric phase map is compared to burst mode interferograms that are simulated from the same pair of ERS-2 images.

Burst mode data were simulated and processed from Phoenix stripmap data. The raw data from the two stripmap ERS-2 scenes were used to synthesize burst mode data by omitting blocks of raw data lines from stripmap data files. The length of each burst was

chosen to be 60 lines and the inter-burst gap was set to 240 lines. Consequently, the burst cycle time was equivalent to 300 lines of ERS-2 raw data. The burst data parameters of this simulation are comparable to those of the Envisat Wide Swath Mode (Table 3.1). The same bursting scheme was used to simulate burst mode data from both the stripmap images. However, the selection of the starting line of the simulated burst data within the stripmap file determines the resultant burst overlap between the two simulated images. Since the offset between the two stripmap images was already known from the stripmap InSAR processing, various simulations of the secondary burst mode scene (19991220) were generated with each simulation having a different amount of burst overlap with respect to the bursts in the reference scene (19990315).

All the simulated burst mode data were processed using the modified SPECAN algorithm, with each image burst being processed and stored. The spacing factor used in the modified SPECAN algorithm was set to 10, which resulted in an output pixel spacing that is equivalent to the pixel spacing obtained from taking 10 azimuth looks in the stripmap data processing presented previously. In this way, the stripmap data and ScanSAR data have the same pixel spacing.

The processed bursts of the reference and secondary burst mode images were interfered and the resulting burst interferograms were coherently combined to obtain a continuous interferogram. No further looks of the burst mode interferograms were taken. The burst mode differential interferograms were formed using the same DEM that was used in the stripmap interferometry processing to remove the topographic phase contribution. Also, the same adaptive filter parameters and unwrapping method were used to obtain unwrapped differential interferometric phase maps from the burst mode data.

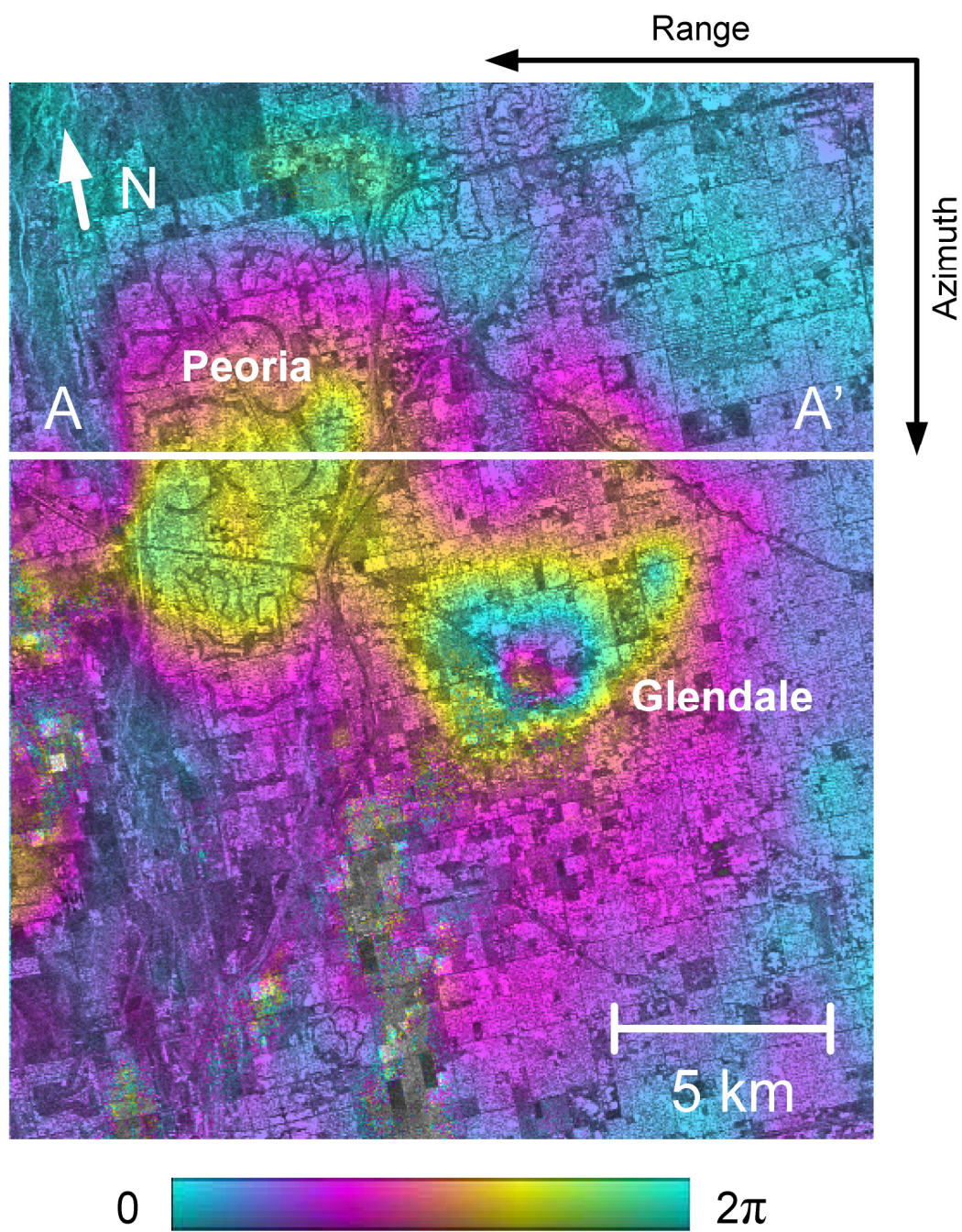


Figure 4.2: InSAR phase map obtained from a stripmap interferogram spanning the time between March 15, 1999 and December 20, 1999. The figure shown bounds the land subsidence features in the cities of Peoria and Glendale in the Phoenix metropolitan area. The perpendicular baseline is 150 meters.

Displacement phase maps obtained from ScanSAR interferograms (Figure 4.3) for four cases of burst overlap (100% 80%, 60% and 40%) are compared to the displacement phase map obtained from stripmap data (Figure 4.2). A visual inspection of ScanSAR interferograms reveals that phase signatures of the land subsidence features are generally similar in all four cases of the ScanSAR interferogram and are comparable with the stripmap interferogram (Figure 4.2). Also noticeable is that the amount of decorrelated area (pixels in grayscale) increases as the amount of burst overlap decreases from 100% to 40%. Although it is expected that interferometric phase coherence decreases with decreasing burst overlap, it is evident that even at 40% burst overlap most of the deformation feature is still detectable.

A quantitative analysis of the results was performed by taking radar azimuth line profiles running approximately east-west through the subsidence features (line AA' shown in Figure 4.2). These profiles (Figures 4.4 (A) through 4.4 (D)) confirm the expectation that differential interferometric phase noise increases with a decreasing burst overlap. In the 100% burst overlap case (Figure 4.4-A), the deformation phase profile from the burst mode interferogram (shown in red) is nearly identical to the profile from stripmap interferogram (shown in black). There is a marked increase in the phase noise levels as burst overlap decreases from 60% to 40%. In the case of the 40% burst overlap (Figure 4.4-D), the profile follows the stripmap profile (in black) in a broad sense but does not pick up the subtle variations seen in the stripmap profile. As expected the standard deviation of the phase differences between the ScanSAR and stripmap profiles shown in Figure 4.4 increases as the burst overlap percentage decreases. The standard deviations are as follows for the 100%, 80%, 60% and 40% burst overlap cases of the Phoenix ScanSAR interferogram are 0.2, 0.3, 0.5, and 1.1 radians, respectively.



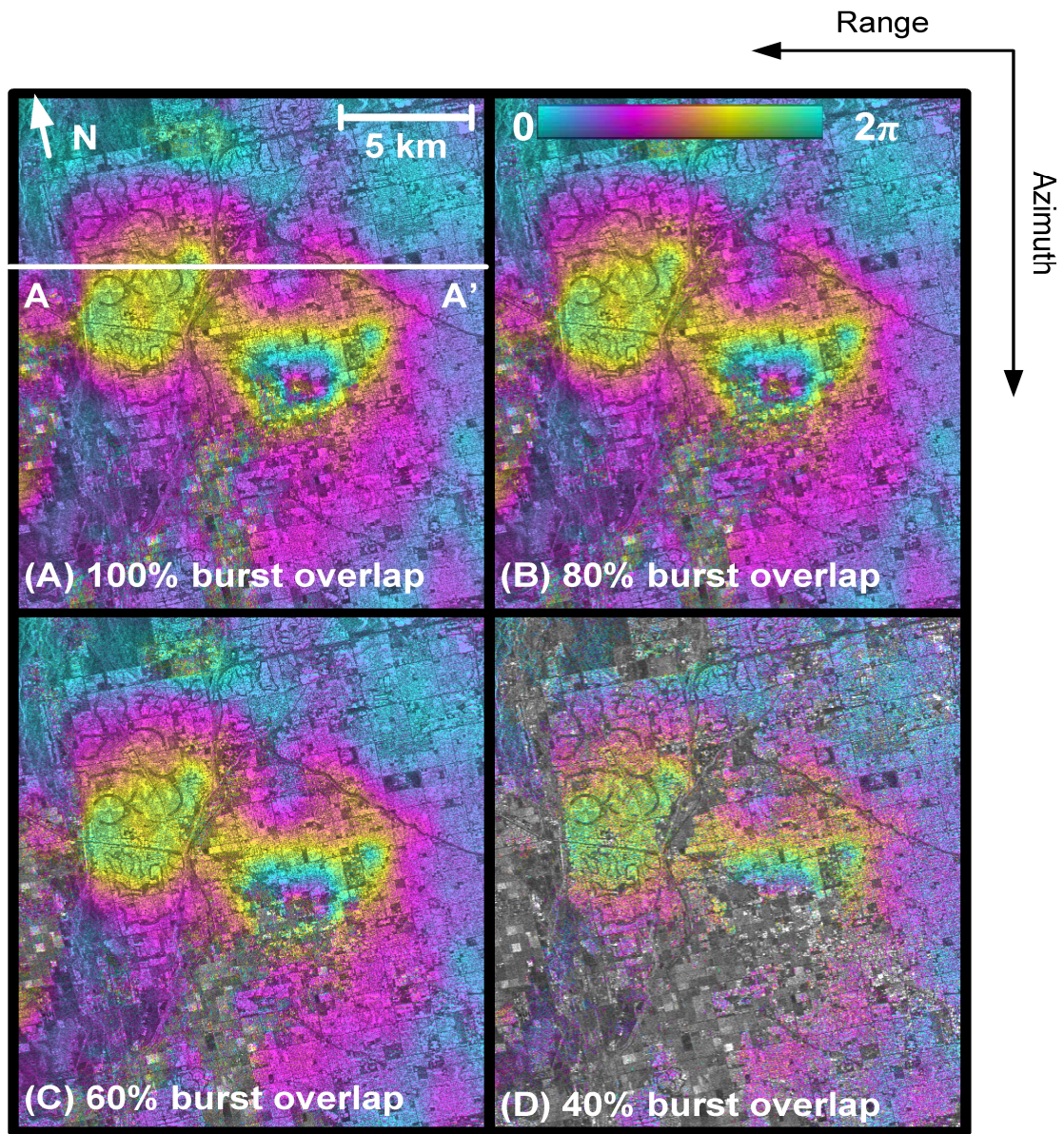


Figure 4.3: ScanSAR InSAR phase maps for various burst overlap cases. Burst mode data was simulated from the same pair of stripmap SAR data scenes considered earlier in Figure 4.2.

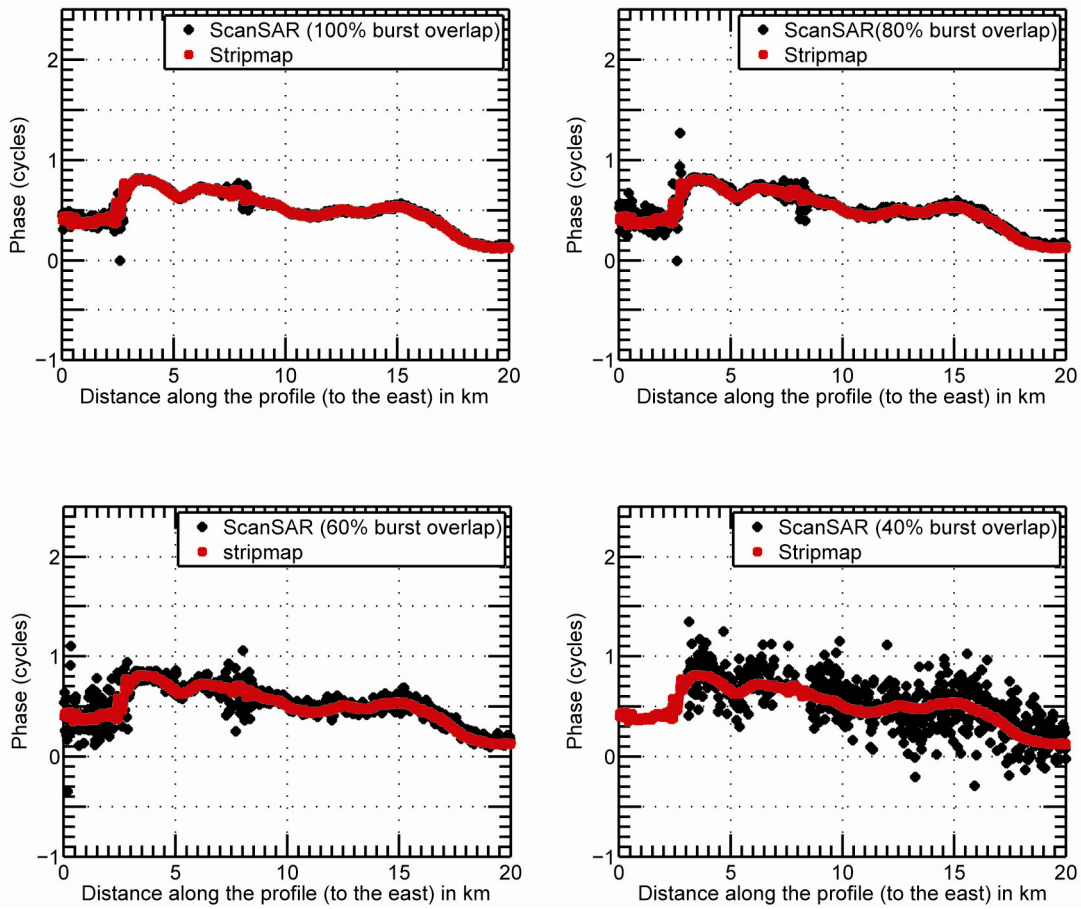


Figure 4.4: Profiles through InSAR phase maps shown in Figure 4.3. Unwrapped phase is calculated along the east-west direction (AA').

#### 4.2.2 Other Case Studies

The effect of burst overlap on the interferometric phase coherence is dependent on land surface characteristic of the imaged area. This aspect is further investigated by considering a number of study sites that vary in terms of land surface characteristics as well as in the scale and magnitude of the deformation.

Similar to the analysis performed at the Phoenix study site, ScanSAR interferograms with varying burst overlap percentages were generated for the following study areas: (1) Hector mine, California, (2) Yellowstone, Wyoming, (3) London, U.K., and (4) Houston, Texas. Presented below are the phase maps and profiles through the deformation features measured using ScanSAR InSAR at each study site each case.

### ***Hector Mine, California***

Co-seismic deformation associated with the October 19, 1999 earthquake in California is measured using a pair of ERS-2 stripmap images. This study site is again an example of an arid area but the scale and the magnitude of the observed deformation feature is quite large (more than 100 km). Unlike the land subsidence feature seen in Phoenix which was localized, the earthquake deformation feature extends over the entire SAR image frame (Figure 4.5). The one-month interferogram spanning the period between September 15, 1999 and October 20, 1999 and having a perpendicular baseline of 20 meters was processed using the same parameters and steps that were followed in processing the Phoenix interferogram. These steps include, taking looks in range and azimuth, removing topographic phase contribution using an SRTM DEM, applying a spatial adaptive filter, and phase unwrapping using the same correlation threshold. Again, burst mode images were simulated from stripmap images using the same bursting scheme of 60 lines per burst and 300 lines per burst cycle.

ScanSAR displacement phase maps (Figure 4.6) generated from simulated burst mode images faithfully reproduce the deformation signature of the earthquake event as seen in the stripmap displacement map (Figure 4.5). Since the interferogram spans just one month and has a small perpendicular baseline the phase coherence in the ScanSAR interferograms is generally high all across the image. Profiles taken (along the line



indicated as AA' in Figure 4.5) through the displacement maps provide a quantitative comparison of ScanSAR and stripmap interferometric phase (Figure 4.7). There is a good agreement between stripmap and ScanSAR profiles even in the case of 60% burst overlap. Although more noise is observed in the case of 40% burst overlap, profile through the ScanSAR interferogram closely follows the profile from stripmap interferogram.

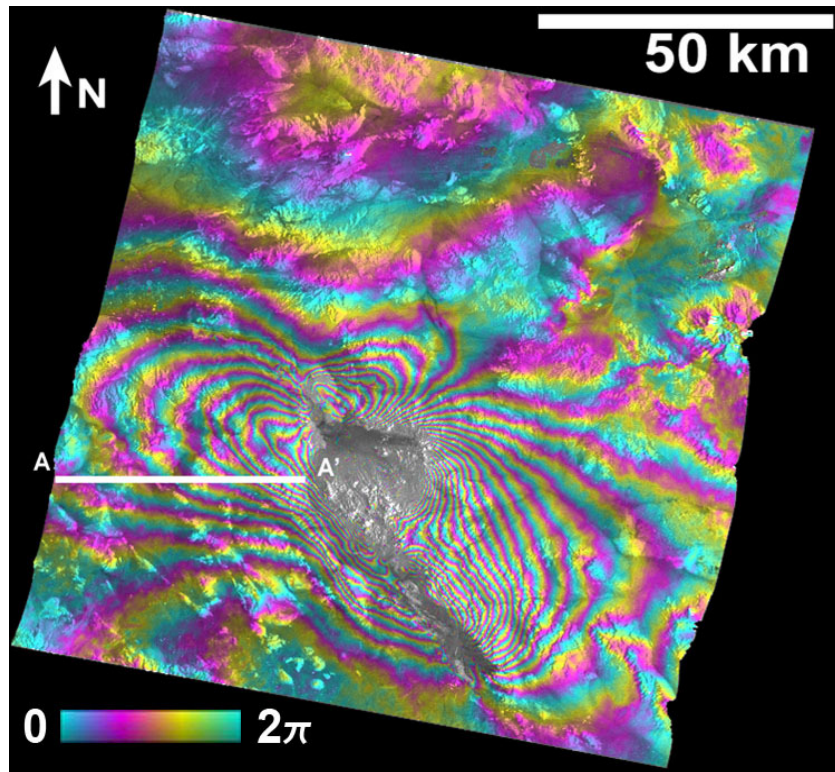


Figure 4.5: InSAR phase map over Hector Mine, California obtained from a stripmap interferogram spanning the time between September 15, 1999 and October 20, 1999. The perpendicular baseline is 20 meters. Co-seismic deformation associated with the October 19, 1999 earthquake is measured.

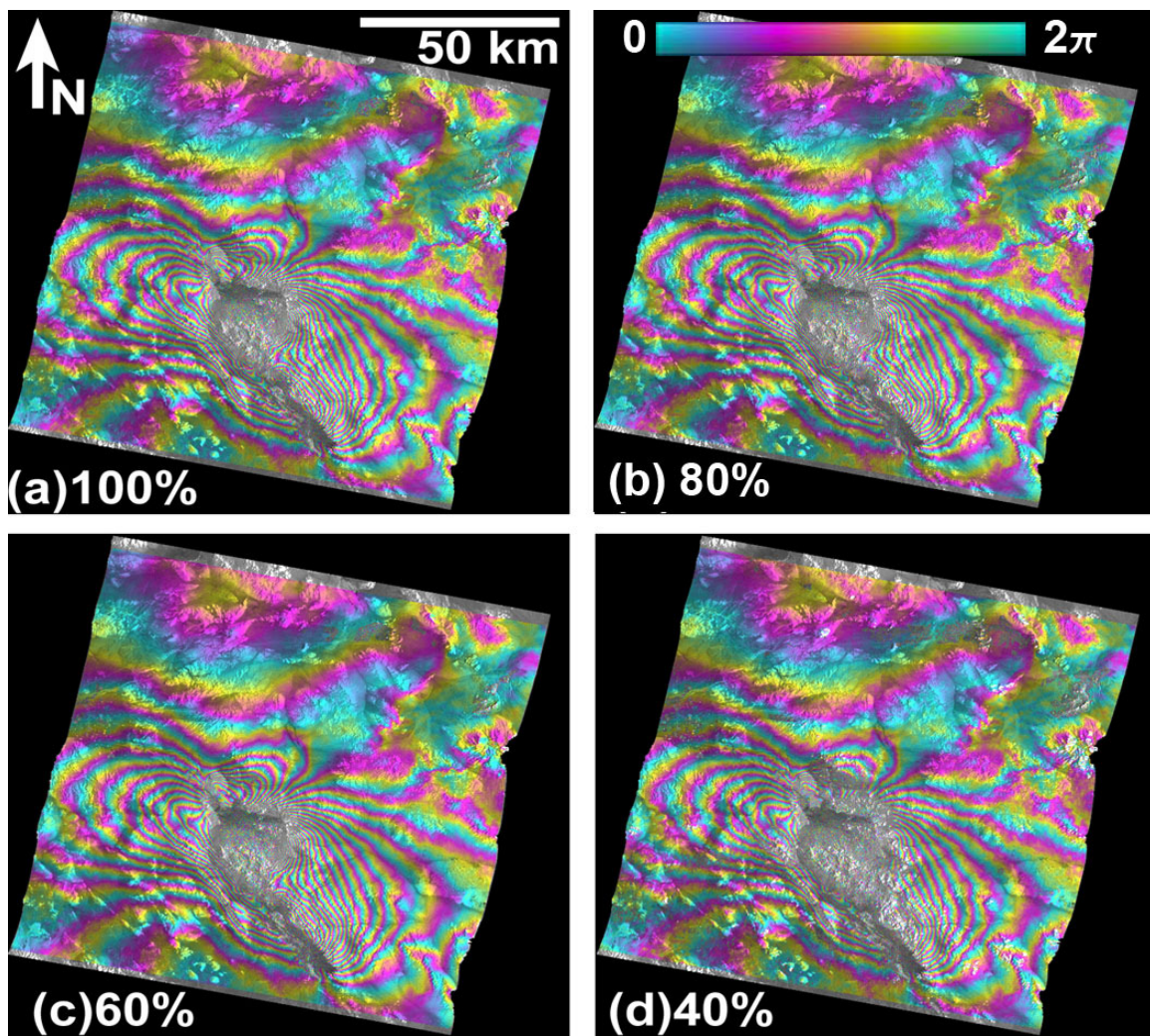


Figure 4.6: ScanSAR InSAR phase maps for various burst overlap cases. Burst mode data was simulated from the same pair of stripmap SAR data scenes considered earlier in Figure 4.5.

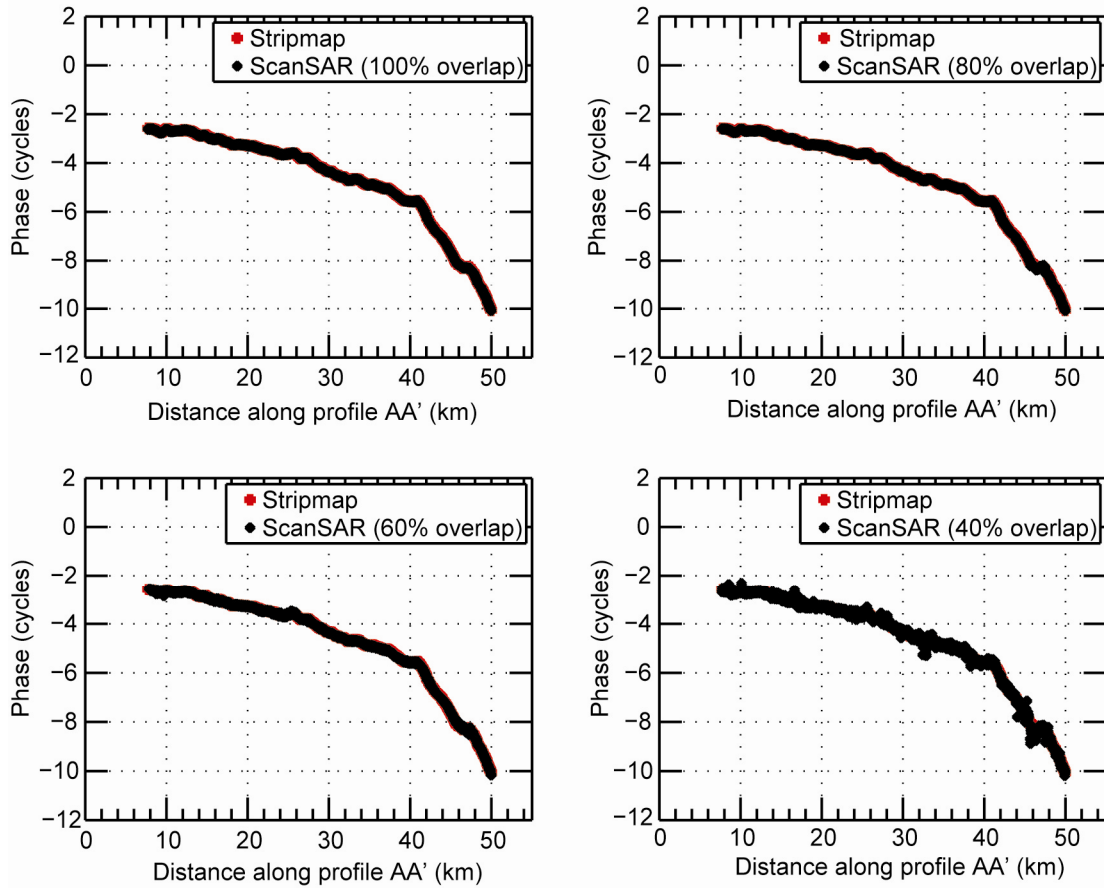


Figure 4.7: Profiles through InSAR phase maps shown in Figure 4.6. Unwrapped phase is calculated along the east-west direction (AA') shown in Figure 4.5.

### *Yellowstone, Wyoming*

Surface deformation associated with the magmatic fluid migration in the Yellowstone caldera captured by a pair of ERS-2 SAR images is considered (Figure 4.8). This is an example of an area where there is very little urbanization. The 26-month interferogram spanning the duration between June 28, 1993 and August 30 1995 has a perpendicular baseline of 190 meters. Following the usual process of simulating burst



mode data from stripmap images, displacement phase maps were generated from ScanSAR interferograms having varying amount of burst overlap.

ScanSAR displacement maps over the Yellowstone caldera (Figure 4.9) reveal the

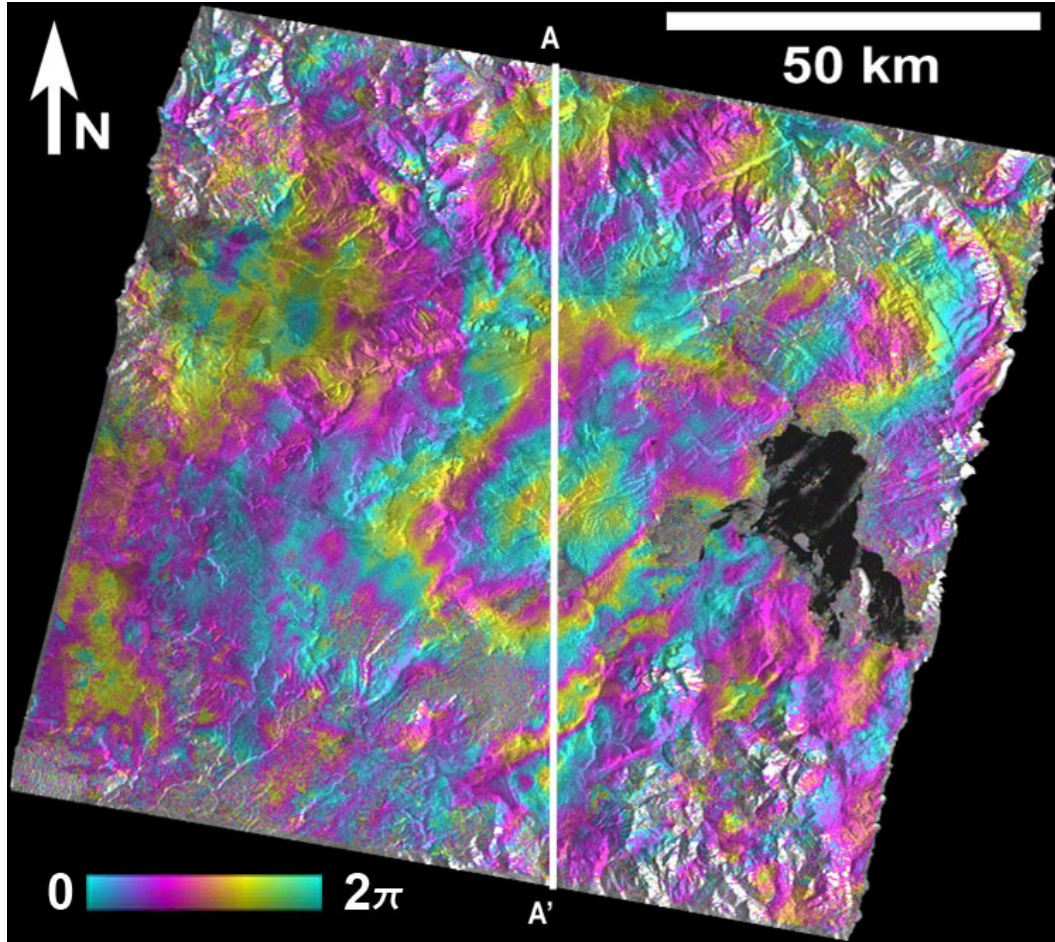


Figure 4.8: InSAR phase map over Yellowstone, Wyoming obtained from a stripmap interferogram spanning the time between June 28, 1993 and August 30, 1995. The perpendicular baseline is 190 meters.

same expected trend. Interferometric phase coherence drops as the amount of burst overlap decreases. Although the multi-kilometer scale deformation feature is clearly visible in the 100% burst overlap case (Figure 4.9 (a)), in the case of the 40% burst over, the deformation feature is only faintly noticeable. As done for the previous study sites,

profiles through the subsidence features (along the line AA' in Figure 4.8) are taken for closer inspection of the phase noise (Figure 4.10). From the profiles, it appears that there is no significant improvement in interferometric phase noise in going from lower burst overlap to higher burst overlap. However, it can be seen that the number of pixels with a correlation value higher than the threshold, decreases as burst overlap percentage decreases. Although, ScanSAR profiles through interferograms fail to follow the subtle spatial variations in the subsidence profile seen in stripmap interferograms, the ScanSAR profiles follow the general large-spatial scale trends.

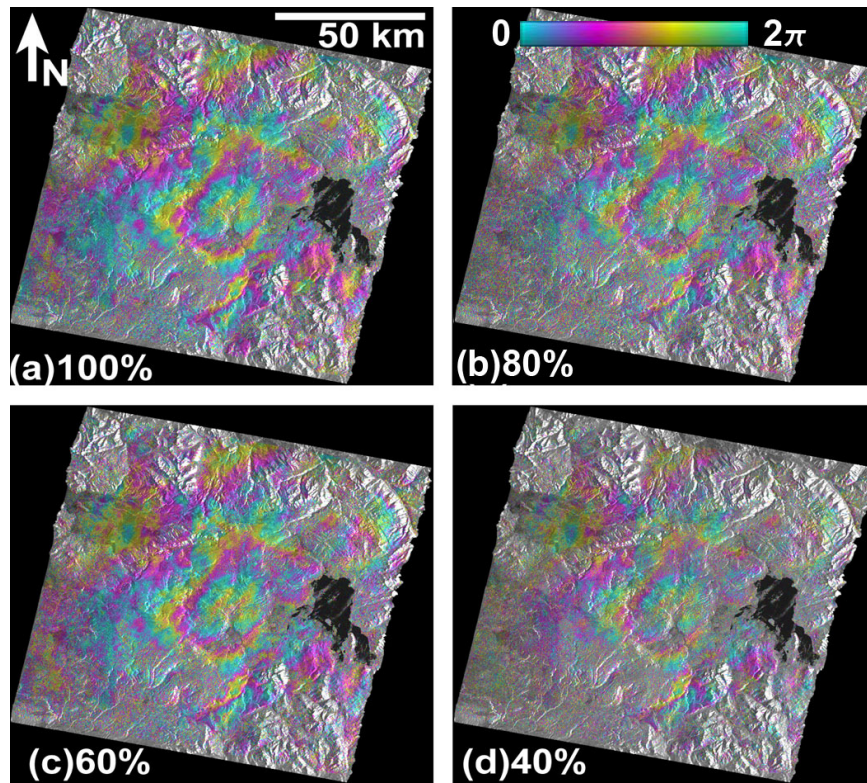


Figure 4.9: ScanSAR InSAR phase maps for various burst overlap cases. Burst mode data was simulated from the same pair of stripmap SAR data scenes considered earlier in Figure 4.8.



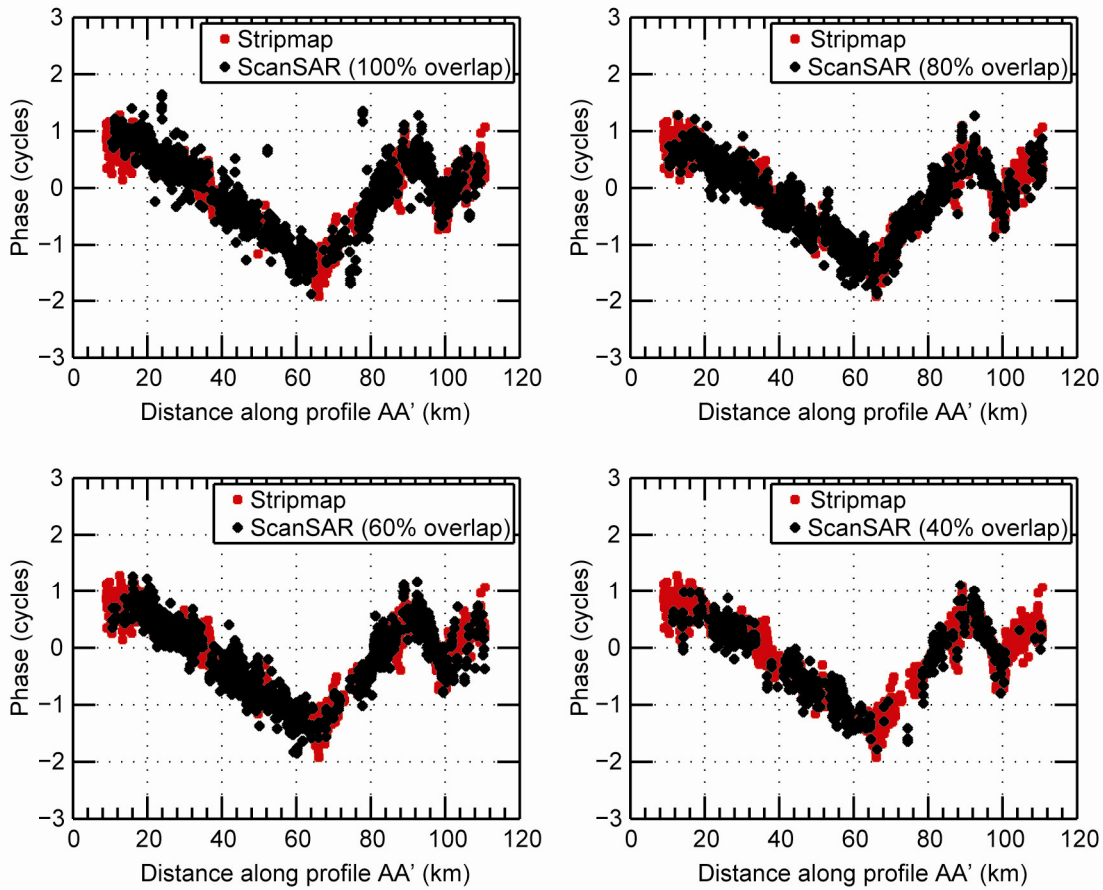


Figure 4.10: Profiles through InSAR phase maps shown in Figure 4.9. Unwrapped phase is calculated along the east-west direction (AA') shown in Figure 4.8.

### ***London, United Kingdom***

In the case study, land subsidence caused by tunnel excavation work in central London is considered where small spatial scale deformations with small magnitudes are measured using InSAR. Due to the very slow rate of land surface deformation, an interferogram spanning more than 5 years is considered so that a measurable quantity of the deformation signal is captured by InSAR. An interferogram spanning the period between September 1, 1995 and November 3, 2000 and having a perpendicular baseline

of 20 meters is used to obtain a displacement phase map showing land subsidence at the London Jubilee Tunnel excavation site (Figure 4.11). Burst mode data is then simulated from the same pair of ERS-2 stripmap images for various burst overlap percentages.

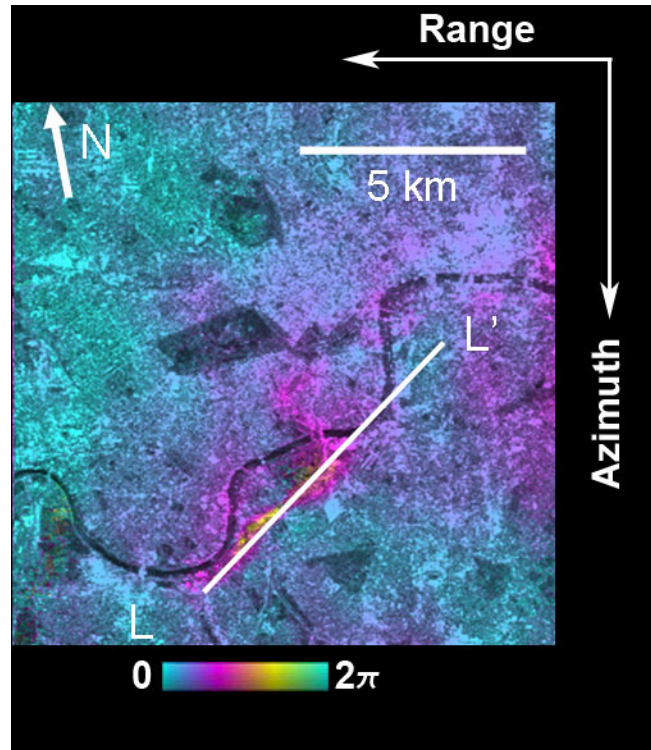


Figure 4.11: InSAR phase map over central London, UK obtained from a stripmap interferogram spanning the time between September 1, 1995 and November 3, 2000 and having a perpendicular baseline of 20 meters.. The figure shown is a small subset encompassing the land subsidence feature caused by tunnel excavation.

A comparison of ScanSAR displacement maps (Figure 4.12) with stripmap displacement maps indicates that interferometry with ScanSAR images having low burst overlap is not suitable for the detection of small scale deformation features. For the London study site, only a small portion of the ScanSAR interferogram had good coherence when the burst overlap dropped below 70%. Although the profiles (taken

along the line LL' in Figure 4.11) through the subsidence feature roughly follow the profiles from stripmap data, they fail to capture the subtle spatial trends seen in stripmap data. It was not possible to extract meaningful unwrapped interferometric phase when burst overlap was less than 70% (Figure 4.13).

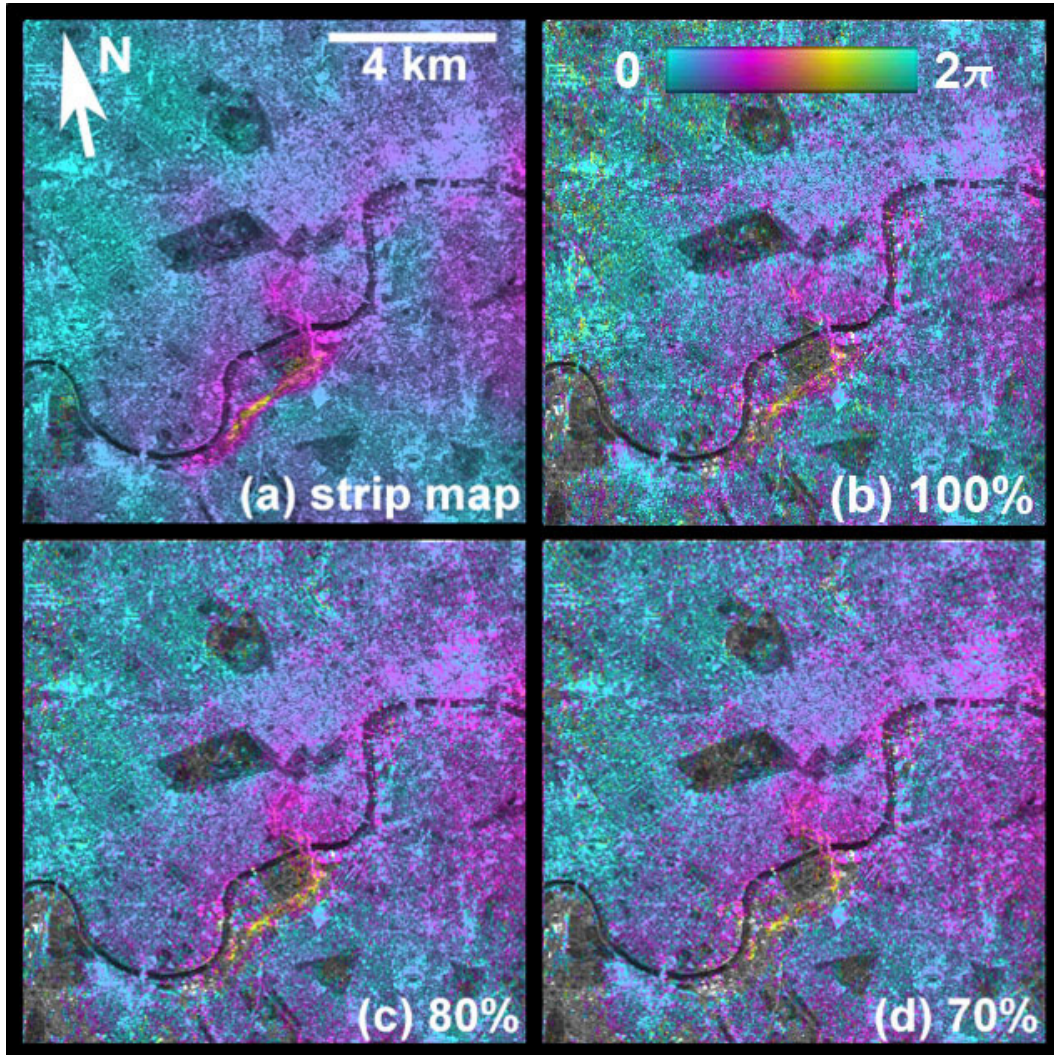


Figure 4.12: ScanSAR InSAR phase maps for various burst overlap cases. Burst mode data was simulated from the same pair of stripmap SAR data scenes considered earlier in Figure 4.11.

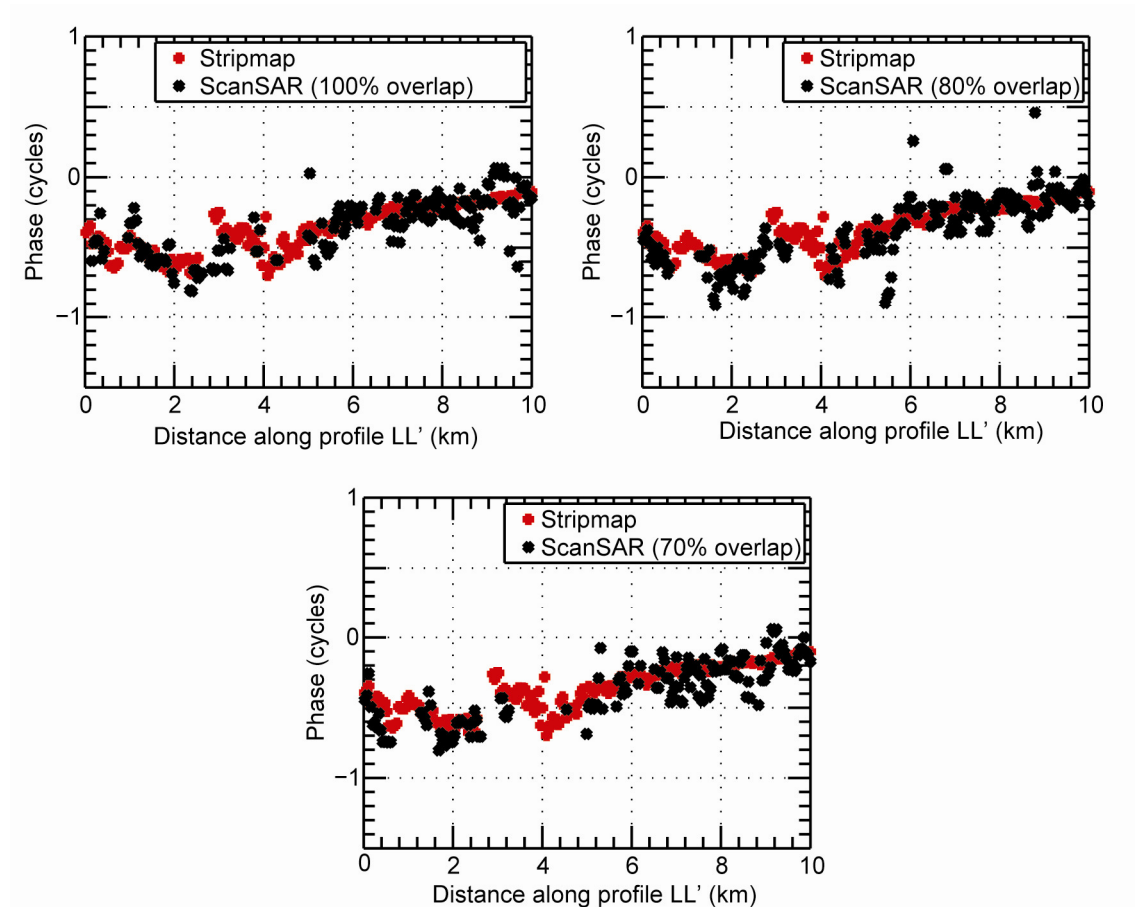


Figure 4.13: Profiles through InSAR phase maps shown in Figure 4.12. Unwrapped phase is calculated along the east-west direction (LL') shown in Figure 4.11.

### *Houston, Texas*

InSAR measurements of land subsidence in Houston, Texas, caused by groundwater withdrawal pose similar challenges as seen in the London study site. Houston is characterized by dense urbanization along with the significant vegetation. A two-year interferogram formed using ERS-2 images is used to analyze the effects of burst overlap in ScanSAR interferograms over Houston, Texas. The interferogram spanning the dates of December 26, 1995 and December 30, 1997 has a baseline of 240 meters. Burst



mode data simulated from stripmap ERS-2 images are used to form ScanSAR interferograms with varying burst overlap percentages.

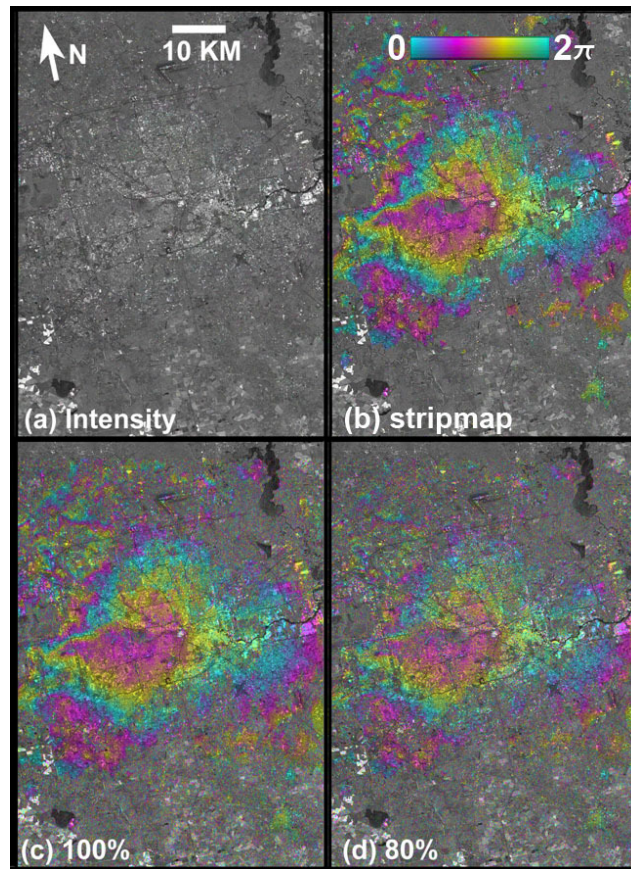


Figure 4.14: Stripmap and simulated ScanSAR InSAR phase map over Houston Texas obtained from stripmap ERS-2 SAR images acquired on December 26, 1995 and December 30, 1997. The perpendicular baseline is 240 meters.

ScanSAR displacements phase maps (Figure 4.14) were formed for burst overlap cases in which adequate portion of the interferogram had good phase coherence. Unlike the Phoenix ScanSAR interferograms, where even 60% burst overlap was sufficient to obtain reasonable phase coherence, ScanSAR interferograms over Houston show a faster rate of decline in phase coherence with decreasing burst overlap. It was found that at least

80% burst overlap is needed to obtain reasonable phase coherence in ScanSAR interferograms over Houston using an Envisat WSM like bursting scheme. This concludes the presentation of the results describing the effect of burst overlap.

In the foregoing analysis (for all study sites including Phoenix), an important filtering operation was skipped while forming the ScanSAR interferograms from burst mode data. When implemented, the so-called azimuth common band filtering improves the interferometric phase coherence in ScanSAR interferograms in cases where the burst overlap percentage is less than 100%. The filtering step was intentionally omitted so as to accentuate the true noise levels in ScanSAR interferograms caused by burst misalignments. Also, presenting the interferometric phase that contains decorrelation noise due to burst misalignment helps in appreciating the significant reduction of noise levels when azimuth common band filtering is implemented. Azimuth common band filtering is discussed in the next section.

To summarize, results showing the effect of burst overlap on the interferometric phase in ScanSAR interferograms were presented in this section. Presence of higher phase noise in interferograms with lower burst overlap reiterates the necessity of having good burst overlap in ScanSAR interferograms. It is seen that in arid regions like Phoenix, Arizona and Hector Mine, California it is possible to retrieve meaningful interferometric phase with 60% burst overlap using a bursting scheme that is similar to Envisat Wide Swath mode. In urban areas that are heavily vegetated like London and Houston, performing ScanSAR interferometry can be challenging and is limited to pairs of ScanSAR images that have very good burst overlap. Use of azimuth common band filtering operation, discussed later in the chapter, is expected to improve the phase coherence when burst overlap is less than 100%.

In the next section, it is shown that a time series of deformation maps can be generated from a database of ScanSAR interferograms. A realistic burst overlap scenario is assumed where the burst overlap between the ScanSAR images is not ideal but adequate. The methodology and the time series results obtained from ScanSAR interferograms over Phoenix are presented. Also, it is shown that by using azimuth common band filtering coherent phase can be extracted from ScanSAR interferograms having less than 50% burst overlap.

#### **4.3 INSAR AND SBAS ANALYSIS USING SCANSAR DATA**

The goal of this study is to generate land surface deformation time series maps from a database of interferograms formed from ScanSAR or burst mode data, i.e. burst mode interferograms. The Small BAseline Subset (SBAS) technique [Berardino et al., 2002] is applied to burst mode interferograms synthesized from a large collection of stripmap ERS-1 and ERS-2 stripmap SAR data. These SAR images are over a known area of land subsidence in the Phoenix metropolitan area. Simulated burst mode data is used here because it is not yet feasible to obtain a large collection of actual ScanSAR data with suitable baselines and with favorable burst overlaps from the currently available ScanSAR archival data.

The rest of this section is organized in the following manner: the first subsection briefly explains the SBAS technique followed by a subsection that describes the simulation of burst mode data and its processing. The last subsection elaborates on the InSAR processing steps and the various parameters used in the processing algorithm.

### 4.3.1 The SBAS Technique

The SBAS technique of time series generation (Figure 4.15) is based on an “inversion” of a database of interferograms [Berardino et al., 2002]. Starting from a collection of SAR images over a particular study site, interferograms are formed between pairs of SAR images. The pairing is done in a wise manner by imposing limits on the maximum allowable perpendicular baseline and the maximum allowable temporal separation between the pair of images. These limits reduce the effects of geometric and temporal decorrelation.

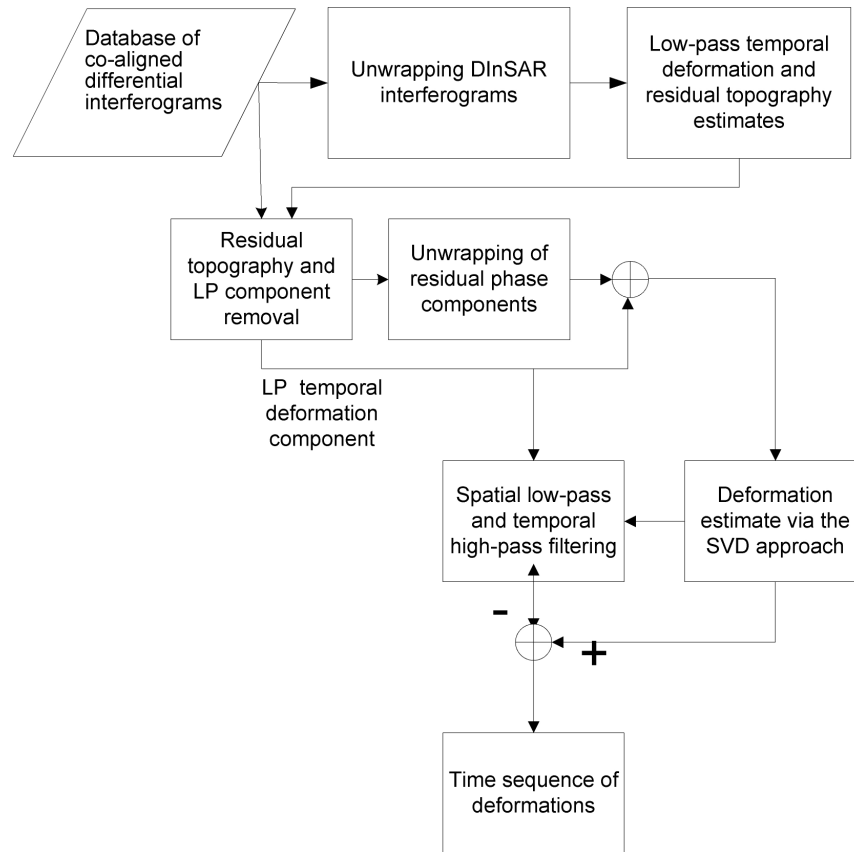


Figure 4.15: Block diagram of the SBAS technique (Adapted from Berardino et al. [2002]).



The SBAS technique relies on a database of interferograms that are all co-aligned in radar coordinates, i.e. in azimuth and slant range. So, before the interferograms are formed, all images are resampled to a common reference image, which is chosen from one of the SAR images of the collection. The resampling process ensures that all the SAR images and the interferograms resulting from the various combinations of those images are all co-aligned. After the interferogram formation step, all interferograms are multi-looked to improve the phase coherence as well as to assure that the interferograms have comparable resolutions in range and azimuth directions. For each interferogram, the usual steps of the differential interferometry are followed. A DEM is used to remove the contribution of the reference surface and the topography from the interferometric phase. The resulting differential interferogram is spatially filtered, and using a phase unwrapping method, the differential interferometric phase is obtained for all pixels whose correlation coefficient is above a selected threshold. The next step of the SBAS algorithm involves the estimation of a low-pass, long-term trend and a residual topography component. The residual topography component is an estimate of the error in the DEM. Following the initial estimation process, the estimated DEM error phase component and the long-term velocity trend component are removed from the original differential interferograms to obtain the residual differential interferograms. These interferograms are spatially filtered and a phase unwrapping process is performed to obtain the residual differential interferometric phase maps, also called residual phase maps. Next, the long-term linear trend is added to the residual phase maps to obtain the topography-corrected differential phase maps.

The estimation of deformation time series involves an inversion operation. The database of topography-corrected differential phase maps is inverted using the Singular Value Decomposition (SVD) method to obtain a differential phase map on each of the

SAR acquisition dates with respect to the first date of the SAR image collection. The output of the SVD method is a time series of estimated deformation phase maps. Note that the differential phase maps contain atmospheric phase components superimposed on deformation trends. Next, a spatial low-pass filter and a temporal high-pass filter are applied to the differential phase maps to estimate the atmospheric phase maps. The estimated atmospheric phase maps are then subtracted from the differential phase maps to obtain the nonlinear or short-term deformation trends. Since the SBAS technique is an approach that is applied to differential interferograms, it can be directly extended to burst mode differential interferograms without any modification to the method.

The SBAS processing software used in this analysis was developed and graciously provided by fellow doctoral student Dochul Yang.

#### **4.3.2 Burst Mode Data Simulation and Processing**

To achieve the objective of generating deformation time series from ScanSAR interferograms, burst mode data was simulated from a collection of stripmap images. A set of 40 stripmap SAR images collected over the Phoenix area were used to synthesize burst mode data. These images, spanning the time period between July 10, 1992 and October 30, 2000, were used to generate a time history of land subsidence. Refer to Table B.1 in Appendix-B for a complete list of ERS scenes used in this study. The bursting scheme described in Section 4.2.1 was utilized, i.e. 60 lines per burst and an inter-burst gap of 240 lines. This bursting scheme, which is similar to the Envisat Wide Swath Mode configuration, resulted in approximately 3 looks per full-aperture length of the ERS azimuth beam. The mid-swath azimuth bandwidth of a single burst of 74 Hz is comparable to the 62 Hz bandwidth seen in the Envisat Wide Swath Mode. The azimuth resolution of the simulated bursts was 90 meters, which was 18 times coarser than the

ERS stripmap data resolution. Since the stripmap data was left unchanged in the slant range direction, the slant range resolution of burst mode images was the same as that of ERS stripmap data.

The burst overlaps, between the various simulated burst mode images, were synthesized in the following manner. Since burst mode data were simulated from existing stripmap data, the burst overlap between the images could be adjusted with a choice of the starting line of the bursting scheme. Two scenarios of simulated burst mode data were generated. In the first scenario, all 40 simulated burst mode images have 100% burst overlap. This scenario, referred to as 100% burst overlap case, is representative of an ideal ScanSAR imaging pattern wherein the orbits and timing of the bursts are perfectly controlled. This scenario is not a realistic possibility with the currently available ScanSAR missions, but it represents a case which would give the best possible interferometric results. In the second scenario, the burst cycles of the 40 simulated images were staggered in such a manner that there would be at least 50% burst overlap between any pair of images of the SAR data collection. This scenario, referred to as the variable burst overlap case, represents a more realistic scanning pattern that is, in principle, close to the new strategy implemented by ESA [Rosich et al., 2007]. The amount of burst overlap between the simulated burst mode images was random selected such that a uniform distribution of offsets ranging between -15 lines and 15 lines was generated for 39 images with respect to one image of the collection. This ensured that the offset between any two simulated burst mode images was at most 30 lines (i.e., 50% burst overlap for a burst length of 60 lines).

A combination of the Range Doppler Algorithm and the modified SPECAN algorithm was used to process the burst mode images. Similar to the processing of example data in Section 4.2.1, each burst of the simulated burst mode image was

processed and stored individually. The Range Doppler Algorithm was used for the following operations: range compression, range cell migration correction, and descalloping. Doppler centroid polynomials estimated from stripmap data were used to process the burst mode data. To remove the scalloping effect, the azimuth antenna pattern was estimated from stripmap images using an estimation algorithm described in Bamler [1991]. The modified SPECAN algorithm was used for the azimuth compression of the bursts with the azimuth output sample spacing factor set to 10. Consequently, the output pixel spacing was 10 times the pulse repetition interval of raw data. Compared to the expected resolution, the chosen output pixel spacing resulted in an oversampling of the processed burst by a factor of two. This oversampling was necessary to accurately register burst mode images before the interferogram formation step. At the interferogram formation step, additional looks in azimuth were taken to make the spacing of the pixels comparable to the expected resolution. For both scenarios, all 40 burst mode images were processed and stored as individual bursts before performing the InSAR analysis.

#### **4.3.3 InSAR and SBAS Time Series Processing**

The general process of forming a differential interferogram using burst mode data is very similar to the stripmap InSAR process. However, there are a few variations in the processing steps due to differences between processed burst mode and stripmap data. First, burst mode data are stored as individual bursts, unlike the continuous from of stripmap data. Second, the Doppler bandwidth of the targets within the burst is much smaller than bandwidth of targets in stripmap data. So burst mode data have much lower resolution compared to stripmap data. Also, the spectral support within the burst bandwidth varies with the target azimuth location. These differences require specific changes in the image co-registration step. Furthermore, an additional azimuth filtering

step is necessary to reduce noise resulting from the non-overlapping portions of the bursts that are being interfered.

### ***Co-registration of Burst Mode Images***

The SBAS technique requires that all SAR images be placed on a common grid. This involves registering and then resampling all the images to a reference image. Multi-looked intensity images were generated for every burst mode image by combining the processed bursts. A continuous multi-looked image is an incoherent intensity image formed by summing the intensities of overlapping bursts. Burst mode images are inherently multi-looked, in this case 3 looks per aperture.

Co-registration of ScanSAR multi-looked intensity images is not a straightforward process because of the lower resolution of ScanSAR images. A simple intensity-based co-registration of burst mode multi-looked images did not yield satisfactory accuracy in the estimation of co-registration offsets. Incorrect estimation of co-registration offsets resulted in azimuth phase banding artifacts as noted in the ScanSAR-stripmap interferometry analysis by Ortiz and Zebker [2007]. To improve the co-registration, a master multi-look image was generated from a chosen stripmap master image. Appropriate looks were taken on the master multi-look image so that it has the same pixel spacing as the multi-looked images obtained from the burst mode images. Note that although the pixel spacing of the stripmap master multi-look image and the burst mode multi-look images was the same, the stripmap master multi-look image had much less speckle noise compared to the burst mode multi-look images. Every burst mode multi-look image was then registered to the master stripmap multi-look image. Based on the registration process, range and azimuth offset polynomials were estimated. These polynomials were then used to resample the burst mode data into the common

radar geometry of the master stripmap multi-look image. Additionally, before forming the interferograms, a second co-registration and re-sampling step was performed to remove any residual offsets between the two burst mode multi-look images. The algorithm explained above is comparable to the co-registration process suggested by Wiesmann et al. [2006] in which the burst mode multi-look images are registered to a simulated intensity image obtained from a DEM that is at a higher resolution than the two ScanSAR images.

### ***Azimuth Common Band Filtering***

Azimuth Common Band Filtering (ACBF) is analogous to the range common band filtering discussed by Gatelli et al. [1994]. In the range direction, a difference in look angles between two SAR acquisitions leads to a shift between the range bandwidths of the two images. Only the common parts of the spectra contribute to the coherent phase, and the non-common parts contribute phase noise. The same argument, albeit in the azimuth direction, applies to the burst mode data when there is less than 100% burst overlap. In the limit when there is no burst overlap, the interferometric phase will be totally decorrelated.

ACBF reduces the spatial resolution of the interferometric phase in the azimuth direction but considerably improves the phase coherence. The improvement in phase coherence is illustrated using a sample differential interferogram which is the same as the one considered in Section 4.2.1. Two distinct cases of burst overlap percentages are considered, i.e. 95% and 40% burst overlap percentage, where a differential interferogram formed without ACBF is compared with the same interferogram in which ACBF was performed (Figure 4.16).. No additional spatial adaptive filter was applied while processing these interferograms. A visual inspection of the interferograms reveals

an expected trend. In the case of 95% burst overlap, there is no discernable difference between the filtered and the non-filtered interferograms. However, in the 40% burst overlap case, the ACBF interferogram is an improvement over the non-filtered interferogram.

Profiles were taken along the range direction, trending approximately east-west (through the subsidence features shown in Figure 4.6), to perform a quantitative comparison (Figure 4.17). Before the profiles were taken, the interferograms were filtered using an adaptive filter of window size 32 and weight 0.8, and unwrapped. A correlation threshold of 0.5 was used for unwrapping in each case. As expected, in the case of 95% burst overlap, there is little difference in noise levels between the azimuth filtered and non-filtered interferograms. However, for the 40% burst overlap case, the profile through the azimuth band-filtered result is much cleaner than its corresponding non-filtered case.

### ***Burst-by-Burst Interference***

After the co-registration and resampling steps, the interferograms were formed using a burst-by-burst interference of the reference and secondary burst mode images. While forming the interferograms, the ACBF process was performed. Two looks in the azimuth direction and four looks in the range direction were taken so that the interferograms have a resolution of 100 meters in azimuth and range direction. The resulting burst interferograms then were coherently combined to obtain a continuous interferogram.

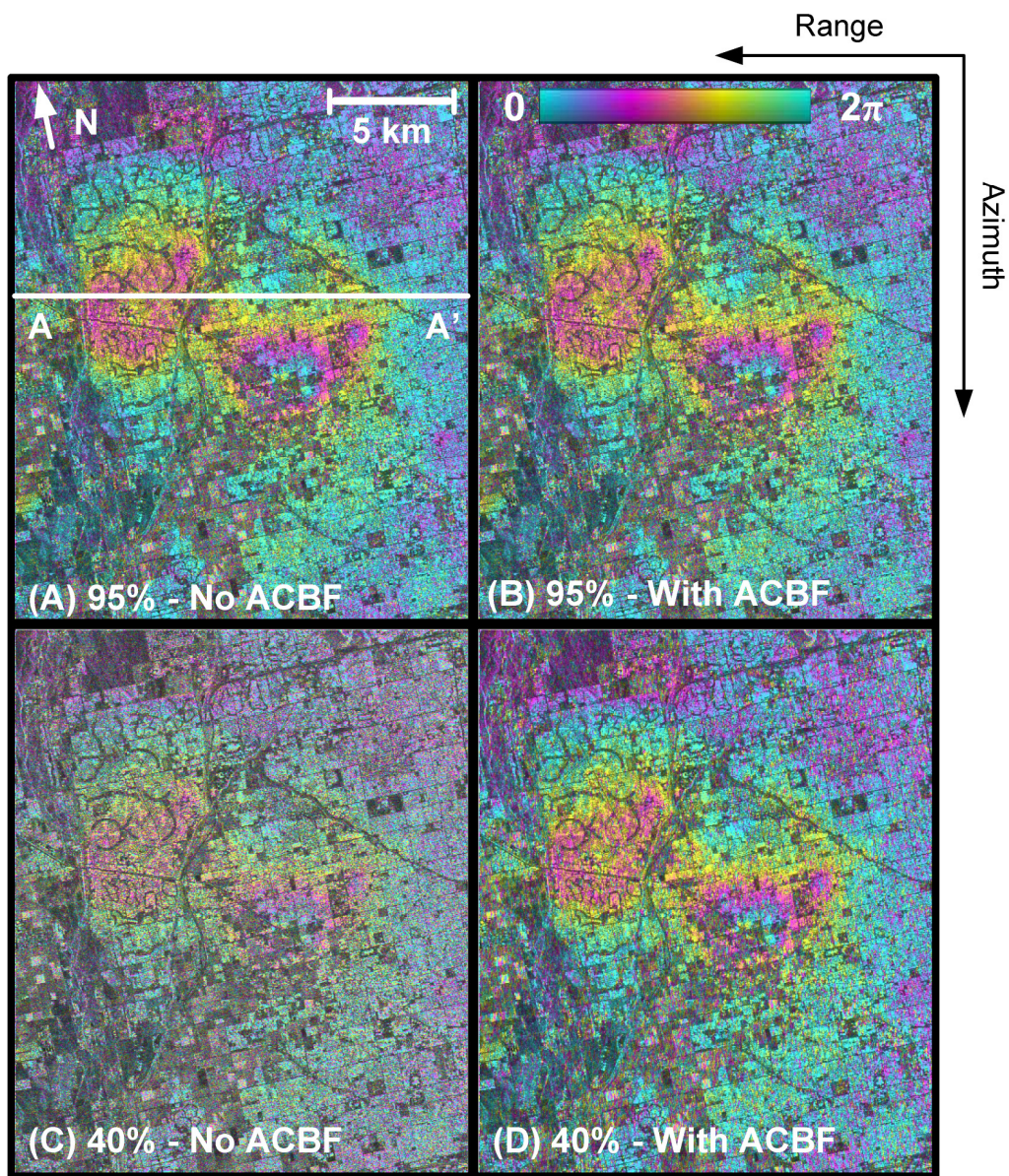


Figure 4.16: Comparison of azimuth-filtered and non-filtered ScanSAR InSAR phase maps.



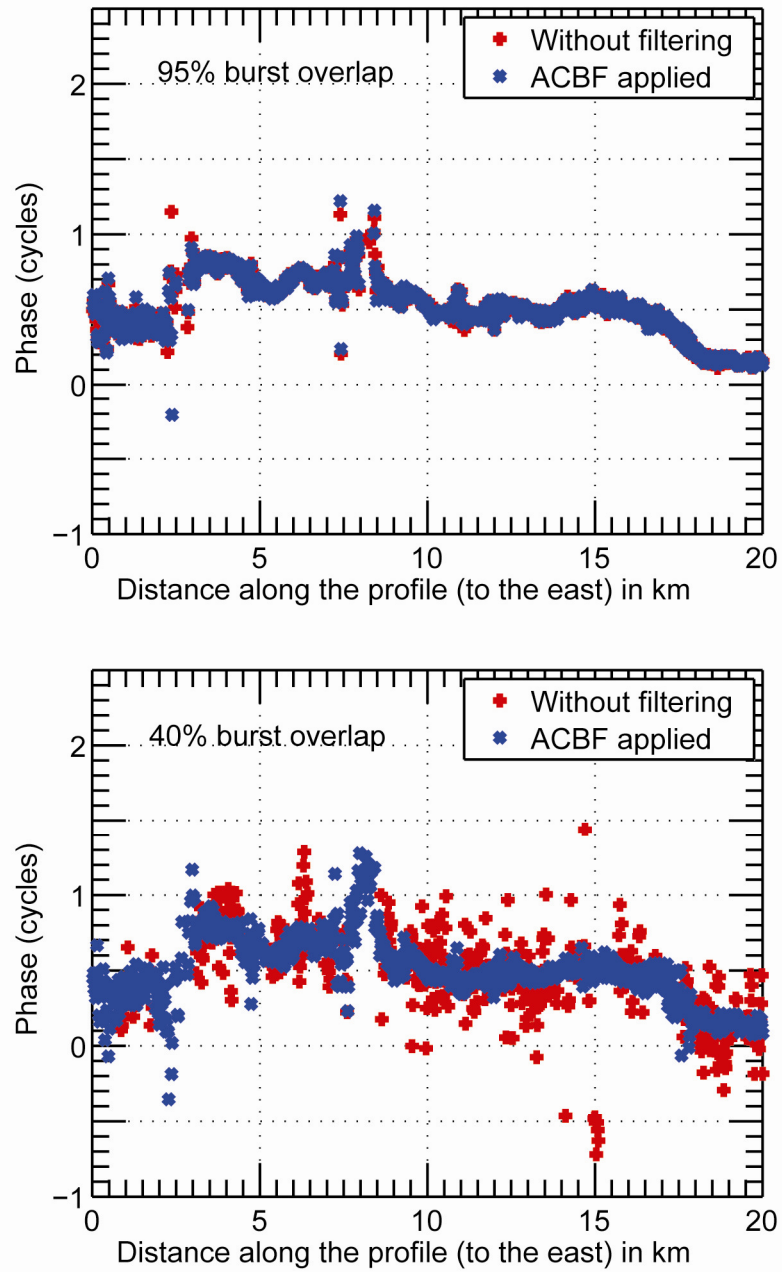


Figure 4.17: Profiles through ScanSAR InSAR phase maps shown in Figure 4.16. The unwrapped phase through azimuth filtered interferograms (blue) is compared with non-filtered phase (red).

### ***Formation of the Differential Interferogram Database***

The first step of the SBAS method is the formation of a database of differential interferograms. The steps mentioned in the foregoing sections, including co-registration, resampling, ACBF, and interferogram formation were used to form two databases of interferograms corresponding to the two burst overlap scenarios. In all, each database contained 101 interferograms formed from pairs of images selected from the 40 simulated burst mode images (Appendix-B Table B.2). SAR image pairs were selected by imposing limits on the maximum allowable perpendicular baseline and the maximum allowable temporal separation between the dates of acquisition. A perpendicular baseline limit of 130 meters and a temporal separation limit of 4 years were applied.

Also, for the purpose of validating the results, a stripmap interferogram database was generated that contained the same 101 interferograms but was formed from regular stripmap data. The ERS stripmap interferograms were multi-looked (20 looks in azimuth and 4 looks in range) so that they have the same 100 m x 100 m spatial resolution as the burst mode interferograms. Refined estimates of the perpendicular baselines obtained from stripmap interferogram processing were used in the InSAR analysis of the burst mode data. A one-arc second SRTM DEM (<http://srtm.usgs.gov>) was used to generate the differential interferograms. A spatial adaptive filter [Goldstein and Werner, 1998] with a filter window size of 64x64 and a filter gain of 0.5 was used to smooth the differential interferograms before the phase unwrapping step. Phase unwrapping was done using a minimal cost flow algorithm. An unwrapping master coherence map was generated by identifying pixels whose correlation coefficient was above 0.5 in all the images of the stack of the 101 images of the database.

The SBAS technique was then applied to the processed differential interferograms and the unwrapped differential phase maps as described in Section 4.3.1. The SBAS

analysis was run three times: once on each of the two simulated ScanSAR interferogram databases and once on the stripmap interferogram database. In each SBAS analysis, linear fit velocities and residual DEM errors were estimated through the stack of differential phase maps for all coherent pixels. The phases associated with the estimated long-term deformation velocities and DEM errors were removed from the differential interferograms and the resulting residual differential interferograms were unwrapped and inverted using the SVD method. The inversion process estimates the residual differential phase maps associated with each of the SAR image dates, calculated with respect to the first image date of the collection. Thus, 39 residual phase maps were estimated where the phase of each map is calculated with respect to the first image. The phase associated with the first image is set to zero, indicating that it is the reference date.

The last stage of the SBAS technique involves the estimation and removal of the so-called atmospheric phase screens. The residual phase maps were passed through a low-pass spatial filter of window size  $2 \text{ km} \times 2 \text{ km}$  followed by high-pass temporal filter to generate the atmospheric phase screen associated with each SAR image. A Kaiser Filter window [Mora et al., 2003] designed to reject non-linear signals having time periods greater than 40 days was applied. It is assumed that the differential phase associated with atmospheric noise is spatially correlated but is temporally uncorrelated. The atmospheric phase screen contains the estimated phase contributions from atmospheric artifacts also calculated with respect to the atmosphere of the first image. Then, the atmospheric phase screens were subtracted from the corresponding residual differential phase maps and the remainder was added to the long-term constant velocity motion. Thus, the final results were obtained as the atmosphere-corrected deformation phase time series maps.

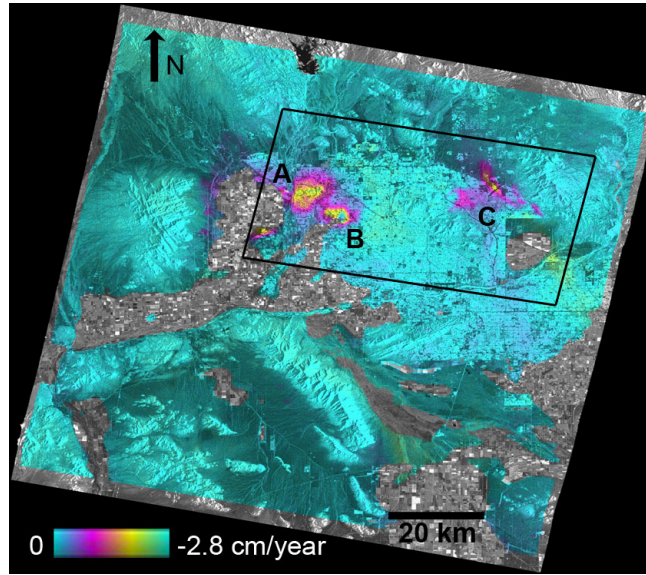


Figure 4.18: Ground displacement rate in the radar line-of-sight direction measured over the Phoenix metropolitan area. This velocity map was obtained from the application of the SBAS technique to a database of ScanSAR interferograms (variable burst overlap case). Locations indicated by letters A, B, and C, correspond to subsidence features in the cities of Peoria, Glendale, and Scottsdale, respectively. Pixels which are decorrelated are in grayscale (radar intensity).

#### 4.4 DEFORMATION TIME SERIES RESULTS AND VALIDATION

The mean velocity map obtained from the application of the SBAS analysis to the database of ScanSAR interferograms with variable burst overlap clearly shows the known land subsidence features around the Phoenix metropolitan area (Figure 4.18). In this figure, rates of land subsidence in the radar line-of-sight direction indicated in color are shown superimposed on a grayscale intensity image of the study site. Deformation phase is converted to displacement using the relation that  $2\pi$  radians of deformation phase correspond to a deformation of  $-\lambda/2 = -2.8$  centimeters, where  $\lambda$  is the wavelength of the

radar signal. Deformation features in the cities of Peoria, Glendale, and Scottsdale are marked with letters A, B, and C, respectively. Similar velocity maps were obtained from the 100% burst overlap base and from the stripmap interferogram database.

Nonlinear deformation trends superimposed on constant-velocity motion are observed from deformation time series for pixels that are located near the center of each of the three subsidence features A, B, and C (Figure 4.19). Seasonal uplifts that coincide with winter months are seen in the time series of the Glendale and Peoria deformation features. Also noticeable is a temporal correlation in the seasonal variations at the Glendale and Peoria features which are in close proximity to each other.

Due to the lack of GPS and leveling survey data that are concurrent with SAR measurements over the study site, deformation time series generated from multi-looked stripmap interferograms (stripmap SBAS results) were used to validate ScanSAR SBAS results. For consistency, all the stripmap images were also registered to the same master reference image to which the burst mode images were registered. This process ensured that the ScanSAR interferograms and the stripmap interferograms, as well as the respective ScanSAR SBAS results and the stripmap SBAS results, were all aligned. Placing the stripmap and the ScanSAR results on a common grid made a pixel-wise comparison of the two possible. For the purpose of validation, stripmap and ScanSAR SBAS time series solutions of the same pixel were considered (Figure 4.19). From visual comparison it is clear that the ScanSAR SBAS time series results are generally in agreement with the stripmap SBAS time series result.

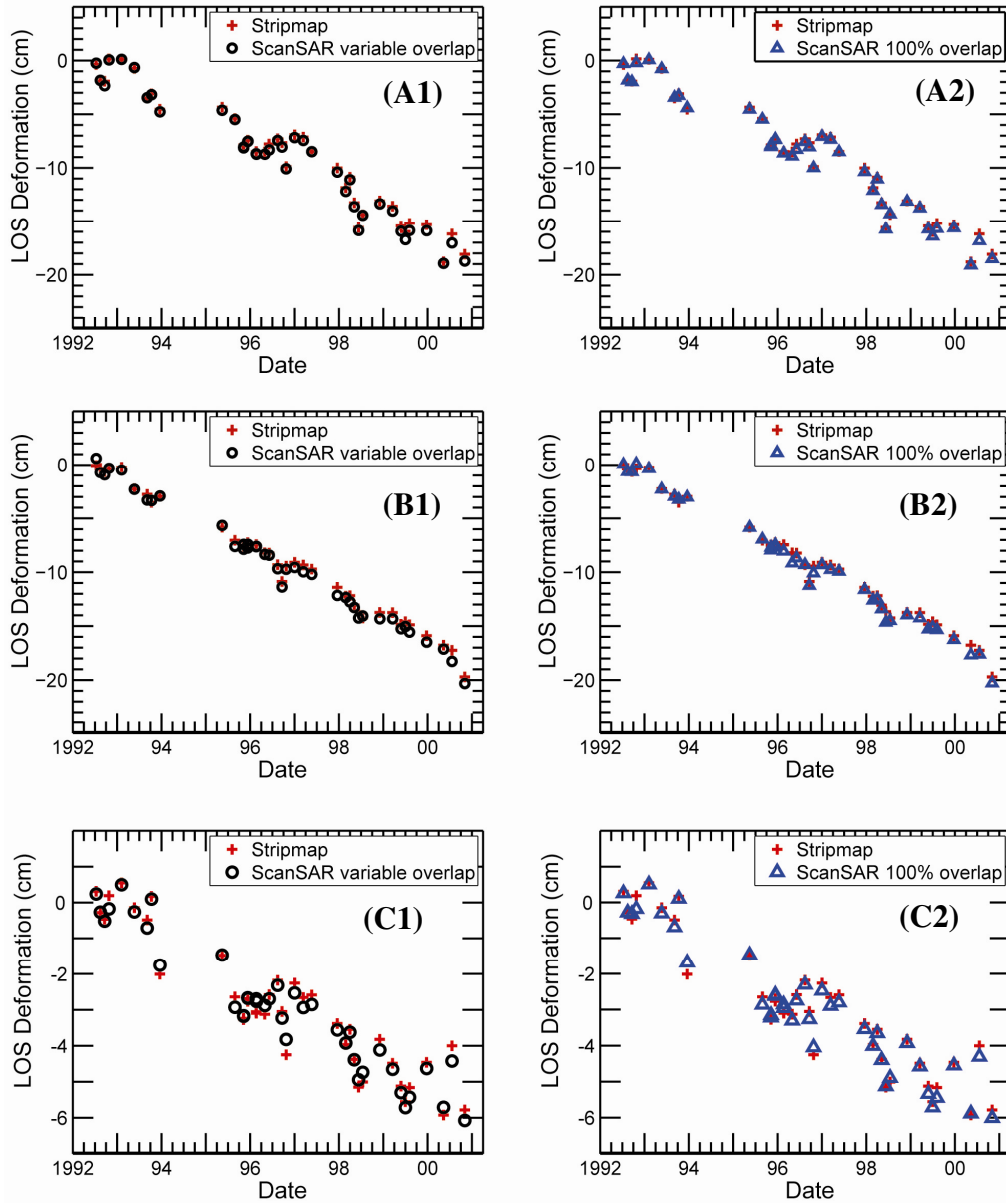


Figure 4.19: Land subsidence time series generated from the SBAS technique applied to ScanSAR data. Deformation corresponding to a single pixel located in subsidence features at Peoria (A1 and A2), Glendale (B1 and B2), and Scottsdale (C1 and C2) are shown. ScanSAR SBAS results from the 100% burst overlap case and the variable burst overlap case are compared with stripmap SBAS results.

Since the same value of correlation threshold was used in determining the coherence mask file, comparison of the number of coherent pixels in the ScanSAR and the stripmap master coherence files gives one of the measures of loss of coherence. It was observed that there was a 3-4% reduction in the number of pixels identified as coherent pixels in going from stripmap data to ScanSAR data. This loss in the number of coherent pixels can be considered a small fraction. For comparison purposes, only those pixels that were coherent in both stripmap and ScanSAR data could be used.

#### **4.4.1 Accuracy in Mean Deformation Velocities**

As a measure of accuracy of the mean deformation velocities obtained from the ScanSAR SBAS analysis of data in the 100% burst overlap case and the variable burst overlap case, the differences of the velocities estimated from the ScanSAR SBAS and the stripmap SBAS processing were considered. For brevity only a subset of the whole image is considered for a visual comparison of the ScanSAR SBAS velocities obtained from the two databases, i.e. 100% burst overlap case and the variable burst overlap case (Figure 4.20 (A)). The boundary of this subset is indicated with a black box in Figure 4.18. For common coherent pixels, velocity difference maps with respect to stripmap SBAS velocities were generated (Figure 4.20 (B)). For the 100% burst overlap case, the mean and standard deviation of the velocity differences computed over all the coherent pixels in the entire image are 0.01 cm/year and 0.02 cm/year, respectively. The mean and standard deviation in the velocity differences for the variable burst overlap case are 0.02 cm/year and 0.02 cm/year, respectively. Note that the deviations in ScanSAR SBAS velocity estimates for the 100% burst overlap case and the variable burst overlap case are nearly identical. The mean and standard deviation of the errors in ScanSAR SBAS velocity estimates obtained in this study are comparable to the estimates made by Casu et



al. [2007], wherein a similar comparison of low-resolution and multi-looked interferograms was performed. Furthermore, the estimated errors in the deformation velocities are within the expected accuracy range of the SBAS method which is 0.05 cm/year to 0.25 cm/year [Casu et al., 2006].

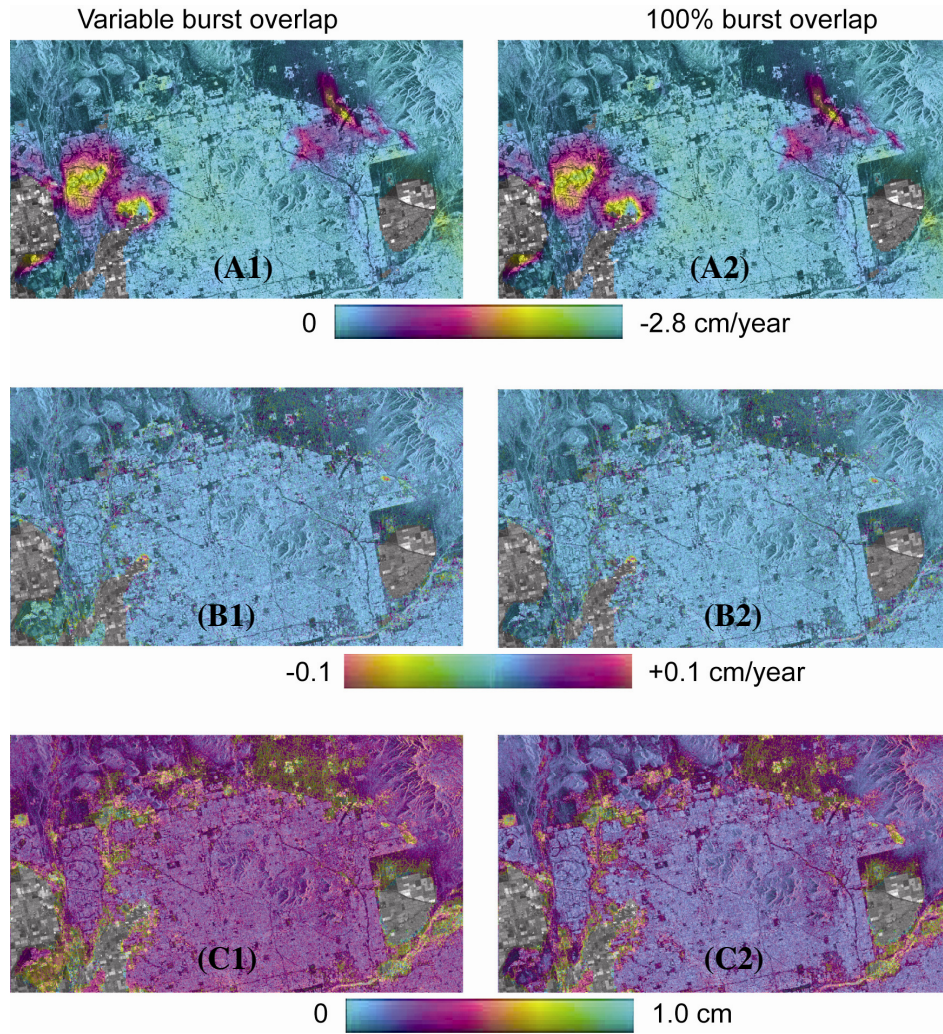


Figure 4.20: Measures of accuracy in ScanSAR SBAS results with respect to stripmap SBAS results. (A1-A2) Mean ground subsidence velocities estimated from ScanSAR data. (B1-B2) Difference between ScanSAR and stripmap velocities. (C1-C2) RMS error in ScanSAR displacements with respect to stripmap displacements. The extent of the map is indicated by a black bounding box shown in Figure 4.8.



#### **4.4.2 Accuracy in Displacement Measurements**

A root-mean-square (RMS) difference was computed as a measure of the accuracy in the estimation of the deformation. The RMS difference was computed pixel-wise, between the ScanSAR SBAS and stripmap SBAS time series solutions at each coherent pixel (Figure 4.20-C). In order to compute the RMS difference between a pair of aligned pixels of stripmap SBAS and ScanSAR SBAS results, the time series solutions were adjusted in such a manner that both data series have a zero linear-fit intercept at the first date of time series. A pixel-wise unweighted RMS difference is then calculated using differences in displacement estimates at each date of the time series.

The RMS difference or error is a measure of relative accuracy of ScanSAR results with respect to stripmap results and not the absolute accuracy of ScanSAR results. For the 100% burst overlap case, the mean and standard deviation of the RMS error computed over the whole image are 0.30 cm and 0.25 cm, respectively. For the variable burst overlap case, the mean RMS was 0.40 cm with a standard deviation of 0.30 cm. Higher RMS differences were seen at a few pixels that are located close to the boundaries of decorrelated regions in ScanSAR interferograms, indicating a need for stricter restrictions on the choice of pixels selected for phase unwrapping. As expected, the RMS differences seen in the 100% burst overlap case are lower than those seen in the variable burst overlap case.

#### **4.4.3 Comparison with Similar Studies**

To compare the results obtained in this work with those reported in a similar study where accuracy of SBAS results from low-resolution SAR data was evaluated [Casu et al., 2007], the statistics of the differences in ScanSAR SBAS velocities and displacements with respect to stripmap SBAS results are expressed in the following

manner. The percentages of the total number of pixels for which the differences in ScanSAR SBAS results and stripmap SBAS results are bracketed by one and two expected standard deviations of the SBAS technique are computed. Based on values reported by Casu et al. [2006], the expected one standard deviation in velocity and in displacement are 1 mm/year and 5 mm, respectively, for the SBAS technique.

The statistics describing the deviations between the ScanSAR and the stripmap velocity estimates reveal that a significant percentage of ScanSAR velocity estimates lie within a reasonable deviation. For the 100% burst overlap case, it was found that 96.4% and 99.1% of velocity differences are within  $\pm 0.1$  cm/year and  $\pm 0.2$  cm/year intervals, respectively. Similarly, for the variable burst overlap case, 96.3% and 99.1% of velocity differences are within  $\pm 0.1$  cm/year and  $\pm 0.2$  cm/year, respectively. These results are close to those reported by Casu et al. [2007] where 98% and 99% of velocity differences (for coherent pixels) are within  $\pm 0.1$  cm/year and  $\pm 0.2$  cm/year, respectively.

Similar statistics that describe the relative accuracy of ScanSAR displacement estimates are given as follows. In the case of the displacement estimates, for 100% burst overlap case, 87% and 98% of coherent pixels have the deviations within  $\pm 0.5$  cm and  $\pm 1.0$  cm, respectively. For variable burst overlap case, 68.5% and 94.6% coherent pixels are within  $\pm 0.5$  cm and  $\pm 1.0$  cm, respectively. Deviations in displacements as reported by Casu et al. [2007] indicate that 98% and 99% of coherent pixels are within  $\pm 0.5$  cm and  $\pm 1.0$  cm, respectively. An inspection of the statistics reported above reveals that the number of pixels for which the deviations in displacements are greater than one- or two-expected standard deviations is more for ScanSAR SBAS analysis than those reported by Casu et al. [2007].

## 4.5 CONCLUSIONS

Results obtained from successfully applying the SBAS technique to ScanSAR interferograms formed from burst mode data were presented. ScanSAR data were synthesized from stripmap data acquired from ERS-1 and ERS-2. Two scenarios of ScanSAR acquisition patterns were simulated. A realistic scenario was simulated wherein any two burst mode images had at least 50% burst overlap. For this realistic case, the difference in the rates of deformation between ScanSAR and stripmap SBAS analyses was found to be on the order of a few millimeters per year (i.e. mean and standard deviation of velocity differences are:  $0.02 \pm 0.02$  cm/year). RMS deviations in displacements were estimated to be less than 1 centimeter (i.e.  $0.40 \pm 0.30$ ).

There is a general agreement between ScanSAR and stripmap time series results. It can be concluded that the velocity and displacement estimates obtained from application of SBAS on ScanSAR data are reliable with acceptable deviations which are expected for low resolution data ( $100 \text{ m} \times 100 \text{ m}$ ). Although velocity estimates obtained from ScanSAR data are very reliable, caution must be used while drawing inferences about nonlinear displacements. Nonlinear signals whose departures from the linear velocity trend are less than 0.5 cm are within the expected noise level for displacement measurements. Results from the 100% burst overlap case are more accurate than results from variable overlap case, especially deviations in displacements. This is expected as ScanSAR interferograms in the variable overlap case have less than 100% burst overlap, thus resulting in loss of interferometric phase resolution.

The burst synchronization characteristics used in this work are similar to those expected from improvements made in 2006 to Envisat ASAR Wide Swath Mode burst synchronization strategy. As more ScanSAR data using Envisat Wide Swath Mode is acquired with favorable baselines, the processing approach presented in this research can

be directly applied to actual ScanSAR data. Moreover, with ScanSAR mode, data collected from multiple subswaths imaged from adjacent tracks can be utilized to increase temporal sampling of deformation phenomena. For example, using the Envisat Wide Swath Mode, it is possible to image the Phoenix area 8 times in a 35 day period compared to just 2 stripmap mode images in the same 35 day period. Some of these revisit tracks are 3 days apart from each other, resulting in virtually sub-weekly SAR image acquisitions. If the observed deformation phenomenon is completely vertical, then interferograms formed from adjacent overlapping tracks can be combined by mapping line of sight deformations of each track into vertical deformations. Another advantage of the wide swath of the ScanSAR mode is that additional study sites can be simultaneously imaged without dropping the coverage over a study site that is currently being investigated.

From the results presented in this chapter, it can be concluded that it is worthwhile to switch to a complete ScanSAR based imaging while imaging arid to semi-arid regions. This includes the entire southwest region of the United States. In other areas which have significant amounts of vegetation good burst overlap between ScanSAR images is necessary for a successful retrieval of coherent InSAR phase.

## **CHAPTER FIVE**

### **PERSISTENT SCATTERER ANALYSIS USING SCANSAR DATA**

In areas where there is a considerable loss of interferometric phase coherence due to temporal and geometric decorrelation, conventional repeat-pass InSAR techniques prove to be ineffective. Persistent Scatterer InSAR (PSInSAR) is the latest of the interferometric methods developed in the current decade that addresses the problems encountered in conventional InSAR. This chapter presents a feasibility study of PSInSAR with ScanSAR data. The formulation of a multiple-scatterer model suitable for ScanSAR data is described, and results pertaining to the application of the model to simulated ScanSAR data are presented.

First, a brief review of the Persistent Scatterer (PS) technique (including the Permanent Scatterer Method, [Ferretti et al., 2000; Ferretti et al., 2001]) and a detailed explanation of a “single-scatterer” PS method used in this study are given. Results from the application of the PS method to stripmap SAR data over Phoenix, Arizona have been provided in the following section.

#### **5.1 BACKGROUND**

The Permanent Scatterer method, originally developed by Ferretti et al. [2000], attempts to tackle the two major problems seen in conventional DInSAR methods: decorrelation and atmospheric noise artifacts. The PS method utilizes a stack of aligned interferograms formed using a single reference scene. Interferometric data from only those pixels that remain coherent in time through the entire stack of the interferograms

are considered as valid. Ferretti et al. [2000] term these pixels as permanent scatterers. It is assumed that the response of such pixels is dominated by a single scatterer present within the resolution cell. The backscatter of such a pixel is considered invariant to variations in viewing angle of repeat-pass SAR imaging [Zebker et al., 2007]. Pixels that have a temporally stable and consistent SAR backscatter are termed PS targets for the remainder of this chapter.

Since PS targets remain coherent over long periods of time and are not affected by geometric decorrelation, interferograms can be formed between any SAR image and a reference image, irrespective of spatial and temporal baselines. Furthermore, in PS methods, phase differences between neighboring PS targets are used to estimate atmospheric phase maps corresponding to each SAR image date. In the PS method, the flexibility of utilizing interferograms having large baselines enables the use of all the available SAR images over a given study site and the advantage of removing atmospheric phase contributions results in better accuracy in the determination of deformation.

Following the development of the original Permanent Scatterer method, several extensions of the method were proposed [Colesanti et al. 2003a, Colesanti et al. 2003b]. Recently, new algorithms which are based on point target analysis were proposed that are collectively referred to as Persistent Scatterer methods [Adam et al., 2003; Werner et al., 2003; Hooper et al., 2004].

The Permanent Scatterer method as proposed by Ferretti et al. [2000, 2001] is a patented technique. Although the motivation and the general processing steps of the Permanent Scatterer method are available in the literature, the exact implementation of the method is proprietary. A general processing chain of the Permanent Scatterer technique as described in Ferretti et al. [2001] is summarized in the following steps:

Step 1: Form differential interferograms using conventional InSAR. Starting from a database of  $N+1$  SAR images over the same area,  $N$  interferograms with respect to a single reference image are formed. Using a DEM of the study area, remove the topographic phase contributions from the interferograms and obtain differential interferograms.

Step 2: Perform a preliminary analysis on the permanent scatterer candidates. Perform preliminary estimation of deformation velocity and DEM error on a sparse grid of potential PS targets. These pixels are referred to as permanent scatterer candidates (PSCs) and are identified by the stability of their amplitude response through the stack of the interferograms. Differences in differential interferometric phase are computed for all possible pairs of PSCs located within a small spatial window (1 km x 1 km). Since the pairs of PSCs are at close proximity to each other, the difference of the differential interferometric phase between the PSC pairs tends to cancel out most of the spatially correlated noise including the phase noise due to baseline errors and the atmospheric phase. It is assumed that all PSC are moving at constant velocity. Again, small deviations from the constant velocity motion tend to cancel out when differences in PSC pairs are computed. Estimates of the difference in velocity and the difference in DEM error between pairs of permanent scatterer candidates are obtained for all possible pairs. The difference estimates then are integrated to obtain the estimates of velocity and DEM error, at each permanent scatterer candidate location with respect to a reference permanent scatterer candidate.

Step 3: Determine and remove an atmospheric phase screen from each interferogram. Phase contributions of the velocity difference and DEM difference estimates are

subtracted from the differential interferometric phase difference for each pair of permanent scatterer candidates. The resulting residual phase differences between permanent scatterer candidate pairs are integrated over the sparse network of the pixels. The residual maps are then low-pass filtered in space and high-pass filtered in time to obtain the atmospheric phase values on the sparse grid of permanent scatterer candidates. Atmospheric phase values that are known only on a sparse grid are interpolated to obtain a low-pass estimate of the Atmospheric Phase Screen (APS) corresponding to each image. APSs are then removed from the differential interferograms to obtain the atmosphere-corrected differential interferograms.

Step 4: Perform an exhaustive search for all permanent scatterers. After correcting the differential interferograms for the APS, a second search for PS targets is carried out for all the pixels in the image. This pixel-by-pixel search is different from the preliminary search for permanent scatterers. Instead of forming differences with neighboring permanent scatterer candidate pairs, the so-called multi-image phase coherence of every pixel is evaluated individually. Unlike in the preliminary search, where the difference in differential interferometric phase cancels out most of the spatially correlated noise, pixel-by-pixel search is more susceptible to noise sources. Phase noise and nonlinear deformations that tend to make the pixel phase deviate from the assumption of the linear deformation model of the permanent scatterers significantly influence the search for permanent scatterers. APS removal from the differential interferograms helps reduce the noise and allows for better detection of permanent scatterers. Unlike the preliminary search, the stability of amplitude response is not used in the detection of permanent scatterers. Pixels which have stable phase are identified as permanent scatterers and for these pixels the deformation velocity and DEM error are estimated.



## **5.2 ADAPTED PERMANENT SCATTERER TECHNIQUE APPLIED TO STRIPMAP DATA**

The PS method implemented in this study is similar to the Permanent Scatterer technique in Ferretti et al. [2000]. Similarities and differences between the original method and the method used in this study are described throughout this chapter.

### **5.2.1 Differential Interferogram Formation**

A set of ERS-1 and ERS-2 SAR images acquired over Phoenix were used to form 40 full-resolution interferograms, each with respect to the same reference image acquired on 30 December, 1996. The term full-resolution indicates that no looks were taken while forming the interferograms. The images used for the PS analysis include the SAR images used for the SBAS analysis in the previous chapter and an additional image acquired on September 25, 2000. The images span a time period between July 10, 1992 and October 30, 2000. The differences between the Doppler centroid frequency of the interferogram image pairs, range from -86 Hz to 315 Hz (Appendix B Table B.1) and indicate that there is little variation in the squint angles through which the images were acquired. Regular processing of SAR images was performed using the Range Doppler Algorithm. All processed images were placed in the zero-Doppler geometry.

Several different criteria can be used in the selection of the reference images used in the PS method. In this research, the reference image was selected in such a way that the largest temporal separation between the interferometric image pairs and the largest perpendicular baseline are both kept as small as possible. In other words, from a chronologically arranged set of images, an image that is centrally located and providing the smallest perpendicular baseline divergence with respect to the rest of the images was selected as the reference image (30 December, 1996). Note that the largest perpendicular

baseline of an interferogram used in this study (Figure 5.1) is about 830 meters, which is comparable to the critical baseline typically seen in ERS data. Other criteria, such as minimizing the distribution of Doppler centroid frequency differences or minimizing the distribution of perpendicular baselines, can be used in selecting the reference image [Kampes, 2006; Colesanti et al., 2003]. In a general case, since the coherence of PS targets is considered to be independent of the baseline geometry, interferograms with baselines larger than the critical baseline can be used in PS analysis.

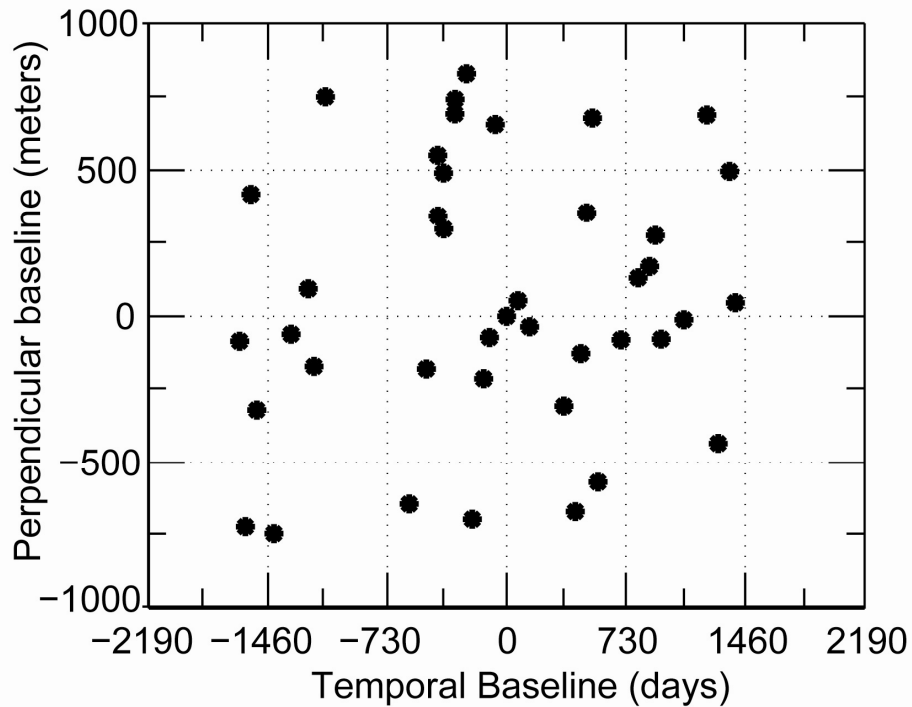


Figure 5.1: Distribution of temporal and perpendicular baselines of interferograms formed with respect to the December 30, 1996 reference image.

Use of the correct baseline estimates is important for accurate measurement of the deformation phase. Precise satellite orbit ephemerides obtained from the Delft Institute for Earth-Oriented Space Research were used in the estimating initial interferometric

baselines. To further improve the baseline estimates, a tedious but straightforward process was used to improve the baseline estimates. First, multi-looked interferograms with 20 azimuth looks and 4 range looks were generated using conventional InSAR processing. Although decorrelation was observed in some portions of the interferograms, the generally arid and urban environment of the study site provided better than expected phase coherence even in the cases of very large perpendicular baselines. Following the usual process of spatial filtering and phase unwrapping, refined interferometric baselines were estimated from multi-looked interferograms. However, this method of obtaining refined baselines cannot be generalized as a processing step because the phase coherence in multi-looked interferograms with large temporal and perpendicular baselines is highly dependent on the characteristics of the study site. In a general case, where refined estimates of interferometric baselines cannot be calculated from the interferograms, residual phase ramps resulting from baseline errors will be absorbed into the atmospheric phase screen. This will be discussed later in the chapter. Differential interferograms were formed using the refined baselines and a one-arc second SRTM DEM.

The differential interferometric phase of an interferogram, which is only known modulo- $2\pi$ , can be expressed as the summation of various components. For pixels that are PS targets, the basic model of the unwrapped differential interferometric phase of the  $i$ th pixel of the  $k$ th interferogram  $\phi_{DIFF}^k(i)$  can be written as [Colesanti et al., 2003a, Kampes, 2006]:

$$\phi_{DIFF}^k(i) = \phi_{DEF}^k(i) + \phi_{TOPO}^k(i) + \phi_{ATM}^k(i) + \phi_{NOISE}^k(i) \quad (5.1)$$

where  $\phi_{DEF}^k(i)$  is the phase due to deformation,  $\phi_{TOPO}^k(i)$  is the phase due to DEM height error,  $\phi_{ATM}^k(i)$  is the phase due to differential atmospheric effects, and  $\phi_{NOISE}^k(i)$  is the

noise from decorrelation and other sources. The topographic phase error is related to the DEM height error  $\Delta z$  [Kampes, 2006]:

$$\phi_{TOPO}^k = \beta^k(i) \Delta z(i) \quad (5.2)$$

where

$$\beta^k(i) = -\frac{4\pi}{\lambda} \frac{B_{\perp}^k(i)}{\rho(i) \sin \theta(i)} \quad (5.3)$$

and  $\beta^k(i)$  is the scale factor to convert height error to phase,  $\rho(i)$  is the slant range to the pixel,  $\theta(i)$  is the look angle,  $\lambda$  is the radar frequency wavelength, and  $B_{\perp}^k(i)$  is the perpendicular baseline associated with the pixel in the  $k^{th}$  interferogram.

The deformation component of the differential interferometric phase can be parameterized and expressed as a function of time. If a physical model of the ongoing surface displacement is available, the deformation phase  $\phi_{DEF}^k(i)$  can be related to the model. In the Permanent Scatterer technique, a constant deformation velocity model is assumed:

$$\phi_{DEF}^k = \alpha^k v(i) \quad (5.4)$$

where

$$\alpha^k = -\frac{4\pi}{\lambda} T^k \quad (5.5)$$

and  $T^k$  is the temporal separation between the two SAR images used to form the  $k^{th}$  interferogram, and  $v(i)$  is the deformation velocity of the pixel. If the actual PS target deformation deviates from the assumed linear deformation model, i.e. the constant velocity model), then the nonlinear terms will be grouped into the noise terms. Small deviations from linear velocity motion are acceptable under the condition that the phase contributions from the unmodeled nonlinear phase variations are less than  $\pi$  radians. The unmodeled components of the differential interferometric phase include the atmospheric phase and noise. Furthermore, the noise term also may contain any components of phase arising due to errors in baselines. So, estimation of the unwrapped differential interferometric phase of the PS targets involves the estimation of three phase components: the DEM error  $\Delta z(i)$  component, the displacement velocity  $v(i)$  component, and the residual phase. These phase components have to be calculated for every pixel of the image.

### 5.2.2 Amplitude Based PS Detection and Sparse PS Network Formation

A sparse network of potential PS targets or permanent scatterer candidates was identified based on the amplitude response of the pixels in the collection of SAR images. The amplitude dispersion index as defined by Ferretti et al. [2001] was used to identify the permanent scatterer candidates. The amplitude dispersion index  $D_A(i)$  is defined as:

$$D_A(i) = \sigma_A(i)/m_A(i) \quad (5.6)$$

where  $\sigma_A(i)$  is the standard deviation of the pixel amplitude through the stack of SAR images and  $m_A(i)$  is the mean of the pixel amplitude. Using statistical analysis, Ferretti et al. [2001] show that pixels with low amplitude dispersion tend to have stable phase.

However, a low dispersion index does not guarantee phase stability. All 41 SAR images used in this study were radiometrically corrected, i.e. compensated for antenna beam pattern before the amplitude dispersion index was computed. Only those pixels whose amplitude dispersion index is less than 0.25 were identified as potential PS targets, similar to the Permanent Scatterer Candidates identified by Ferretti et al. [2001]. Based on this condition, a total of 3335 pixels were identified as potential PS targets, which is about 0.1 percent of the total number of pixels and a density of 15 potential PS targets / km<sup>2</sup>. The PSC density achieved in this study was slightly lower but comparable to the 25 PS / km<sup>2</sup> reported by Ferretti et al. [2001].

In addition to the amplitude dispersion index, the stability of the phase of the pixels is also used was determining if a pixel is PSC or not. To determine the phase stability of the identified pixels, phase differences between neighboring potential PS targets were used. The difference between the differential interferometric phase of two potential PS targets at pixel (i) and pixel (j) in the  $k^{th}$  interferogram can be written as:

$$\delta\phi_{DIFF,ij}^k = \phi_{DIFF}^k(i) - \phi_{DIFF}^k(j) = \delta\phi_{DEF,ij}^k + \delta\phi_{TOPO,ij}^k + \delta\phi_{ATM,ij}^k + \delta\phi_{NOISE,ij}^k \quad (5.7)$$

If the two PS targets are in close proximity to each other, it may be assumed that the differences in spatially correlated error terms and the atmospheric phase terms are so small that they can practically be ignored. Equation 5.7 then can be written as:

$$\begin{aligned} \delta\phi_{DIFF,ij}^k &= \beta^k (\Delta z_i - \Delta z_j) + \alpha^k (v_i - v_j) + \delta e_{ij}^k \\ &= \beta^k (\delta\Delta z_{ij}) + \alpha^k (\delta v_{ij}) + \delta e_{ij}^k \end{aligned} \quad (5.8)$$

where  $\delta\Delta z_{ij}$  and  $\delta v_{ij}$  are the differences in DEM errors and velocities, respectively, between pixel i and pixel j. The linear phase residual arising from sources which do not cancel is denoted by  $\delta e_{ij}^k$ . The linear phase residual contains contributions from small differences in atmospheric phase between neighboring pixels, unmodeled nonlinear deformation phase, phase errors due to baseline errors, and other noise sources.

So the problem becomes one of finding  $\delta\Delta z_{ij}$  and  $\delta v_{ij}$  given the measurements  $\delta\phi_{DIFF,ij}^k$ . However, since the phase of the differential interferograms is known only modulo- $2\pi$ , the estimation of parameters  $\delta\Delta z_{ij}$  and  $\delta v_{ij}$  from a stack of interferograms is not a trivial operation. To solve, Ferretti et al. [2000] introduce the multi-image phase coherence  $\gamma$ :

$$\gamma = \left| \frac{1}{N} \sum_{k=1}^N \exp\{j\delta e_{ij}^k\} \right| \quad (5.9)$$

where

$$\delta e_{ij}^k = \delta\phi_{DIFF,ij}^k - \beta^k \delta\Delta z_{ij} + \alpha^k \delta v_{ij} \quad (5.10)$$

and N is the total number of interferograms used in the analysis and  $j = \sqrt{-1}$  (inside the exponential term). In other words, the multi-image phase coherence is the magnitude of the average of the summation of all the complex residual phase vectors in the stack of images.

In this research, a two-dimensional grid search over values of  $\delta\Delta z_{ij}$  and  $\delta v_{ij}$  was carried out to maximize the multi-image phase coherence  $\gamma$ :

$$\hat{\gamma} = \max\{\gamma\}, \text{ for } \delta\Delta\hat{z}_{ij} \text{ and } \delta\hat{v}_{ij} \quad (5.11)$$

The grid search was carried out for all pairs of neighboring potential PS targets. Since the number of parameters to be estimated is directly proportional to the size of the image, to reduce the computational load only a small subset of the SAR image was considered for PS analysis in this study. A window of size  $12.5 \text{ km} \times 17 \text{ km}$ , encompassing the subsidence features in Glendale and Scottsdale, was selected as the study site. The total number of pixels contained in the window was  $3140 \times 850 = 2,669,000$ . PS targets were linked or paired as neighboring PS targets only if they were located within a certain distance from each other. For each potential PS target pixel, a window of size  $1.5 \text{ km} \times 1.5 \text{ km}$  around the pixel was considered, and each pixel was linked with all the other pixels (potential PS targets) located within that window. Velocity values varying from  $-2$  to  $+2$  cm/year in increments of  $0.1$  cm/year were used to search for difference in velocities. Similarly, for the estimation of differences in DEM errors, values varying from  $-25$  to  $25$  meters in increments of  $0.5$  m were searched through. Consequently,  $\gamma$  was calculated 4141 ( $101 \times 41$ ) times for each pair of PS targets that were linked.

A low amplitude dispersion index does not guarantee that a pixel will have a stable phase. Not all the pixels that were identified as potential PS targets (based on their low dispersion index) were indeed found to be PS targets. Potential PS target pairs or links were considered valid only if the maximum estimated multi-image phase coherence for that link is more than a threshold:  $\hat{\gamma} \geq \gamma_0 = 0.75$ . In total, 83,262 links were formed. Also, the interconnectivity of all the links was analyzed so that the links could be combined together into one continuous network for integration of the differences  $\delta\Delta z_{ij}$  and  $\delta v_{ij}$ . Any of the links that were not connected to the network were also discarded.



After this elimination process, a network of 3164 PS targets remained with 41,260 unique links between them.

### 5.2.3 Residual Phase Screen Generation

The goal of this step is to estimate spatially low pass residual phase screens corresponding to each differential interferogram. These residual phase screens can be subtracted from the differential interferograms to obtain the “linearized” differential interferograms.

A weighted least squares algorithm was used to integrate the velocity and DEM error differences estimated from the links. The weight associated with each link was its estimated  $\hat{\gamma}$  value. The integration assumed zero velocity and zero DEM error at a reference PS location and estimated all velocities and DEM errors with respect to the reference PS location. Each link between a pair of PSCs represented the difference in the values at PSC pair locations. Considering all the PSC pairs, a system of linear equations relating the pairs-differences to the actual values of the pixels was created. A matrix was used to relate the known pair-difference values to the unknown values at each PSC. Each row of the matrix represented a unique link or pair of PSC and each column of the matrix represented a unique PSC. All PSCs except the reference PSC were represented in the matrix. In each row, all columns except those corresponding to the pair of PSCs represented by that particular row are set to zero. In all 41,260 unique links were considered resulting in a network of 3164 PSC. A very sparse matrix of size 41,260 unique connections  $\times$  3163 PS targets was used to relate the difference estimates to the integrated estimates of the parameters. The solution of the linear system of equations was the minimum variance estimate of the integrated values at each PSC location. The LSQR algorithm [Paige and Saunders, 1982] to solve sparse linear equations available from

Stanford University was used in the integration (<http://www.stanford.edu/group/SOL/software/lsqr.html>). Similarly, the residual phase differences from the links were integrated to obtain the residual phase over the sparse network of PS targets with respect to the reference PS target. The integrated residual phase is an estimate of the unwrapped residual phase map at the sparse network pixels.

However, the integrated residual phase maps obtained by the weighted least squares integration will not contain the true residual phase. The integrated phase is a minimum variance estimate and will slightly differ from the true unwrapped residual phase. The true unwrapped residual phase is the difference between the unwrapped differential interferometric phase and unwrapped phase contributions of the velocity and DEM errors. To correct the minor deviations in the integrated residual phase maps, they have to be made congruent with the modulo- $2\pi$  or wrapped phase values of the residual phase maps [Pritt, 1997]. The congruence operation was done in the following way:

First, the integrated velocity and DEM error estimates were converted to velocity and DEM phase component maps over the sparse network of PS for each interferogram. The sparse and unwrapped velocity and DEM phase maps were then subtracted, modulo- $2\pi$ , from the differential interferograms to obtain the residual differential interferograms over the sparse network of PS points. Then, the integrated residual phase maps obtained from weighted least squares integrator were made congruent with the residual differential interferograms. A congruence algorithm suggested in Ghiglia and Pritt [1998] was utilized. After the congruence operation, the difference between the unwrapped residual phase values and the wrapped residual differential interferograms at each point of the sparse PS network was an exact multiple of  $2\pi$  radians.

The next processing step is to create a spatially low-pass residual phase maps for all pixels of the study site using a kriging operation. Kriging is a geostatistical procedure

for estimating missing data values using the information from neighboring pixels for which data is available [Deutsch and Journel, 1997]. A kriging algorithm available through the GeoStatistical Library (GSLIB) public-domain software package was used (<http://www.gslib.com/>). The result of the kriging operation was a database of 40 unwrapped residual phase maps wherein each map contained an estimate of the atmospheric phase, unmodeled nonlinear trends, and noise. Since residual phase maps were obtained by interpolating (kriging) on a sparse grid of points, the estimated maps have low spatial resolution and contain only the large spatial wavelength components of the atmosphere and nonlinear deformation trends.

The kriged residual phase maps  $\phi_{RES}^k$  then were subtracted from the 40 differential interferograms (for all pixels of the study site) to obtain the residual-corrected differential interferograms  $\phi_{RES\_COR\_DIFF}^k$  :

$$\phi_{RES\_COR\_DIFF}^k = \phi_{DIFF}^k - \phi_{RES}^k \quad (5.12)$$

#### 5.2.4 Final Pixel-by-Pixel Search

After the removal of the residual phase maps, many more pixels of the image can be identified as PS targets which were not selected in the amplitude based preliminary selection of potential PS targets. The final search for the model parameters, i.e. velocity and DEM error, was done on a pixel-by-pixel basis. The multi-image phase coherence is estimated for each pixel rather than for each PS pair or link. For this final step, the multi-image phase coherence  $\gamma$  is calculated as the phase difference between the estimated model and the residual corrected differential interferograms. If the linear model phase of a PS target in the  $k^{th}$  interferogram is  $\phi_{MODEL}^k$ , and the difference between the model and actual data is  $\Delta\phi_{MODEL}^k$ , then the multi-image phase coherence can be written as:

$$\gamma = \left| \frac{1}{N} \sum_{k=1}^N \exp\{j\Delta\phi_{MODEL}^k\} \right| \quad (5.13)$$

where  $\phi_{MODEL}^k = \beta^k \Delta z_i + \alpha^k v_i$  and  $\Delta\phi_{MODEL}^k = \phi_{RES\_COR\_DIFF}^k - \phi_{MODEL}^k$ .

For every pixel, deformation velocity and DEM error estimates were found by searching on a 2-D grid spanned by DEM error values ranging between -25 and 25 meters at increments of 0.5 meters and velocity values ranging between -2 and +4 cm/year at increments of 0.1 cm/year.

### 5.2.5 Nonlinear Time Series Generation

To summarize the PS technique followed in this study, a block diagram is provided in Figure 5.2. After the successful estimation of velocities and DEM errors for the PS targets, three unwrapped phase components were calculated: the linear velocity component  $\hat{\phi}_{DEF}^k$ , the DEM error component  $\hat{\phi}_{TOPO}^k$ , and the remainder component  $\Delta\hat{\phi}_{MODEL}^k$ , i.e., the difference of the model phase and the actual residual-corrected differential interferogram.

Next the atmospheric phase screens (APS) are computed from the residual phase maps using a cascade of spatial low-pass and temporal high-pass filters. In the original PS algorithm, the APS are generated before the final estimation step and removed from the differential interferograms. In the approach presented here, residual phase maps were removed from the differential interferograms without any filtering. The reason for this

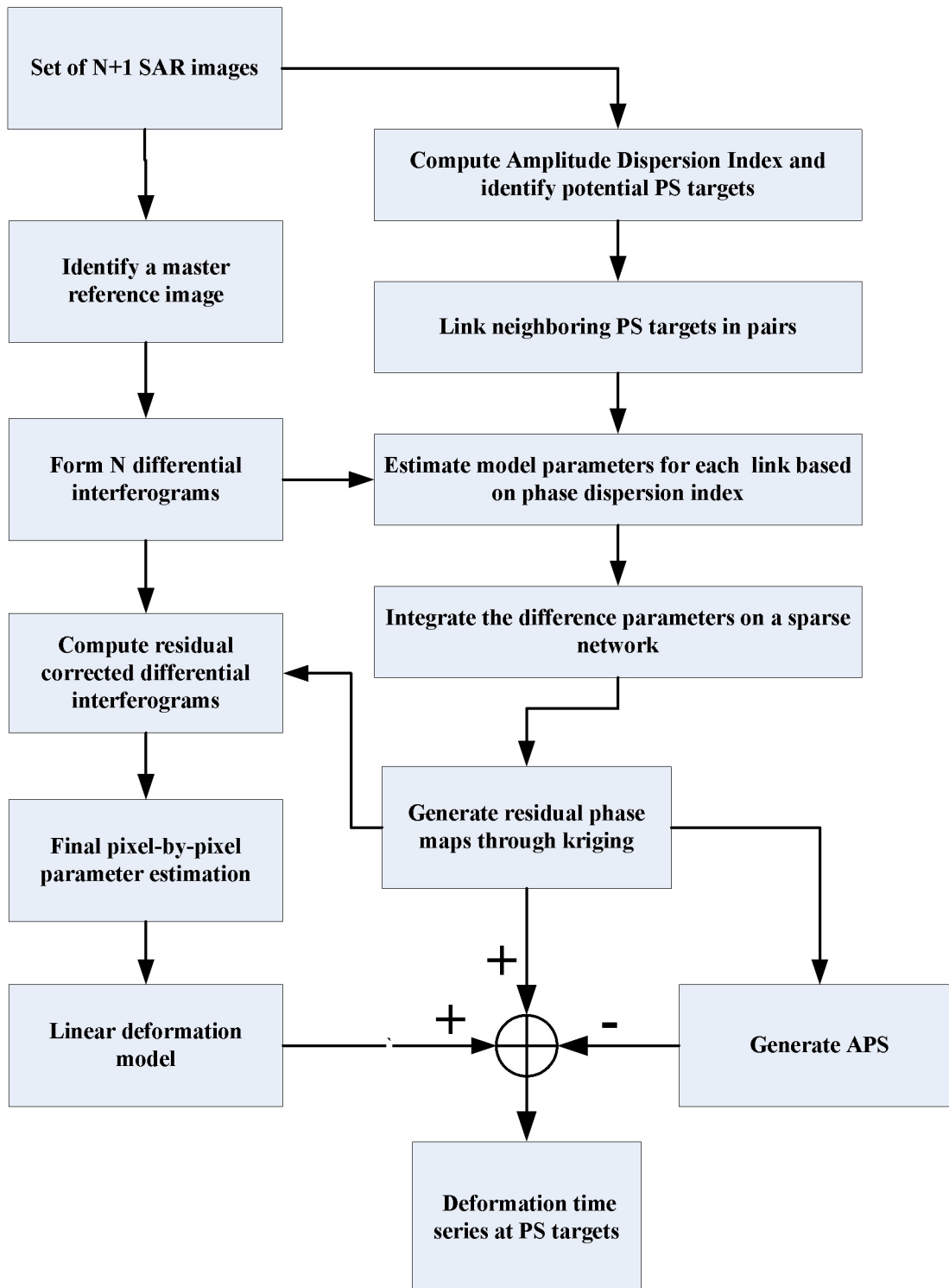


Figure 5.2: Block diagram of the PS technique used in this research.

modification is to make the residual-corrected differential interferograms be as close to the linear velocity model as possible. The residual phase maps remove the APS as well as any spatial low-pass component of the nonlinear motion.

After the final estimation step, a procedure similar to the one used in the SBAS algorithm is used to estimate APS. A moving average low pass spatial filter of size  $2 \text{ km} \times 2 \text{ km}$  and a Kaiser filter designed to remove temporal signals with periods greater than 40 days were used. Atmospheric noise free residual maps were generated by removing the APS from the residual phase maps. Finally, nonlinear deformation time series maps corrected for DEM errors were generated by summing the linear phase component, the remainder component, and the atmosphere-corrected residual phase maps.

#### **5.2.6 Results from stripmap PS analysis**

In the final estimation stage, pixels whose maximum multi-image phase coherence was more than 0.75 were identified as PS targets. Of the 2,669,000 pixels analyzed, 66,501 points were identified as PS targets (Figure 5.3(A)), which is approximately 2.5%. The locations of the PS targets shown in Figure 5.3(A) are approximate as they are placed in the closest pixel in the multi-looked image for visualization purposes. The PS density after the final estimation step was approximately  $312 \text{ PS} / \text{km}^2$ . The PS density obtained in the final step is in agreement with Ferretti et al. [2001] who suggest that in urban areas the PS density is usually greater than  $100 \text{ PS} / \text{km}^2$ .

.From the velocity maps of PS targets (Figure 5.3(B)) the land subsidence features in Glendale and Peoria are clearly identifiable. The velocity field obtained over the cities of Peoria and Glendale from the PS technique is comparable to the velocity field obtained from the SBAS method Chapter 4 (Features A and B in Figure 4.18). Unlike the SBAS

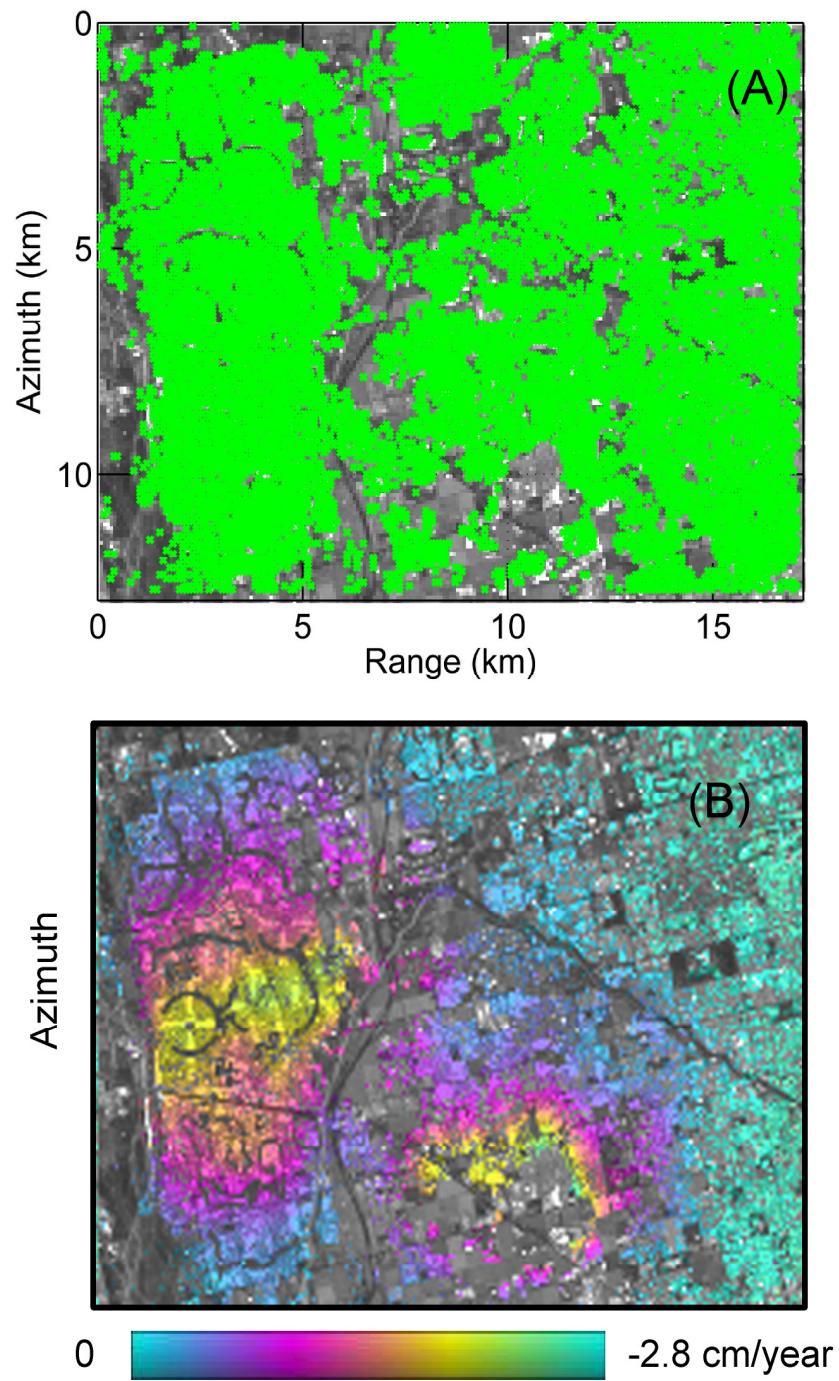


Figure 5.3: (A) Location of PS targets identified in the final estimation step using a multi-image phase coherence threshold of 0.75. (B) PS target line-of-sight deformation velocities.

velocity map which is smooth and continuous, the velocity maps obtained from the PS technique is relatively sparse. If needed, a moving average spatial filter can be applied to the PS velocity map to obtain an average deformation velocity field.

The residual phase maps were passed through a cascade of low-spatial and high-pass spatial filters to obtain the atmospheric phase screens (APSs). After removing the APSs from the residual phase maps, the remainders were then added to the linear velocity estimates to generate the non-linear time series maps. Nonlinear seasonal uplift trends are seen super imposed on long term linear trends at both Peoria (Figure 5.4(A) and Glendale (Figure 5.4 (B)). Uplift or a slowdown in subsidence rate is seen during the fall and winter months of 1992-1993, and 1995-1996. Drop in the levels of groundwater pumpage following the heavy withdrawals in the summer months, allow the aquifer to recharge. This might be the reason for the observed nonlinear trends.

So far the application of the PS technique to stripmap data has been discussed. It has been shown that deformation time series could be generated from interferograms formed without any restrictions placed on the temporal and perpendicular baselines. However, almost all the research in the literature related to the PS technique has been focused on stripmap data analysis. The application of the PS technique to ScanSAR data will enable the use for interferometric purposes over regions where interferograms formed using low-resolution data are expected to decorrelate. By utilizing both the stripmap and the ScanSAR data collected from the same track, stripmap-to-ScanSAR interferograms can be incorporated into the PS analysis. This way, the dates on which stripmap data was not acquired, on account of the sensor being operated in the ScanSAR mode, can be added to the time series. Alternatively, from the perspective of a dedicated ScanSAR mission, the use of PS technique can address the problem of decorrelation in low-resolution data while the wider swath of ScanSAR provides the advantage of shorter



revisit times from adjacent tracks. The next section describes the application of the PS technique to ScanSAR data.

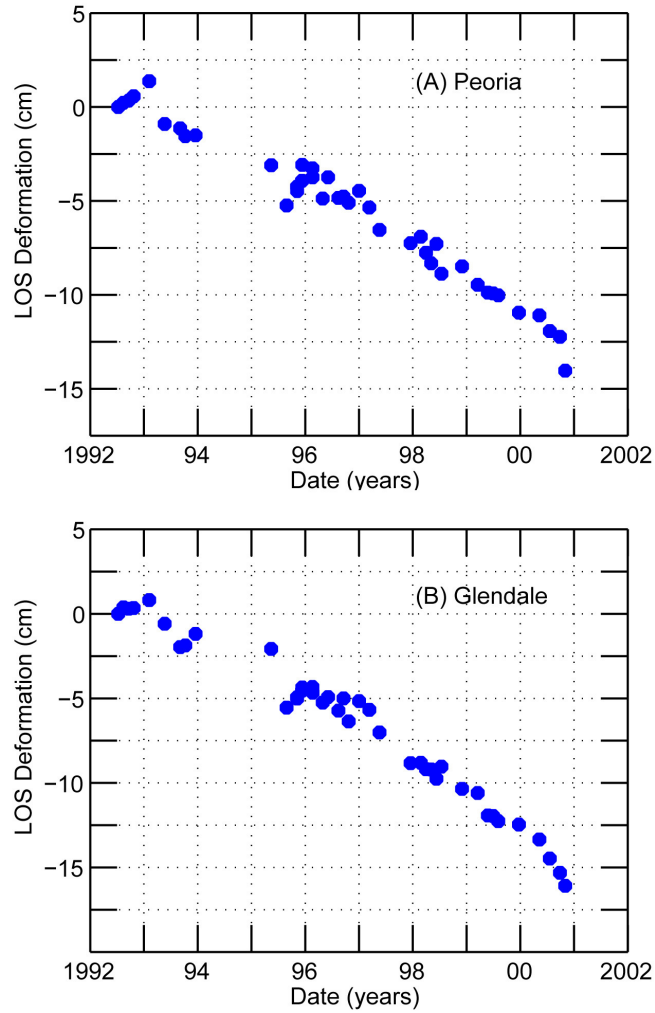


Figure 5.4: DEM error-corrected deformation time series for a PS target located in (A) Peoria and (B) Glendale subsidence features. The time series was computed from stripmap data assuming a single PS target per pixel. Note that the nonlinear deformation trends are added after the removal of the DEM error component

### **5.3 ADAPTED PERMANENT SCATTERER TECHNIQUE AND SINGLE SCATTERER MODEL APPLIED TO SCANSAR DATA**

The goal of the work done as part of this chapter is to investigate the feasibility of performing PS analysis using ScanSAR data. A new functional model called the multiple PS model is formulated to achieve the stated goal. Before describing the derivation of the new model, limitations of a straightforward application of the single target PS technique discussed in the previous sections are detailed.

Increased volumetric decorrelation is expected to result in lesser number of PS targets being detected in ScanSAR data. The basic assumption of the PS technique states that there is a single dominant scatterer per resolution cell. ScanSAR data are at much lower resolution than stripmap SAR data, and larger resolution cells lead to increased volumetric decorrelation. Thus, it is expected that compared to stripmap data, a smaller percentage of pixels in ScanSAR data would be identified as PS targets. Guarnieri [2000] performed a ScanSAR-based PSInSAR feasibility study in which the “survival” of the PS targets was determined from their amplitude or reflectivity. Guarnieri [2000] maps PS targets identified in stripmap data into larger-sized simulated ScanSAR resolution cells and estimates a Signal to Noise Ratio (SNR) for each ScanSAR pixel that is expected to contain a PS target. Guarnieri [2000] defines SNR as the ratio of reflectivity of the stripmap PS target within the ScanSAR pixel to the cumulative reflectivity of all the non-PS targets present within the same ScanSAR pixel. For an SNR threshold of 10 dB, it was estimated that only a small fraction (approximately 5%) of the PS targets detected in the stripmap images would be detectable in ScanSAR images. Furthermore, Guarnieri [2000] concludes that a greater number of PS targets could be detected in ScanSAR data by relaxing the threshold on the SNR.

### 5.3.1 ScanSAR Interferogram Formation

A detailed study is considered here to evaluate the detectability of PS targets in ScanSAR data. Similar to the work described in Chapter Four, burst mode data were simulated from ERS stripmap images. A set of 41 SAR images was used, the same set used earlier for stripmap PS analysis. The same bursting scheme described in Chapter Four is used, i.e. 60 lines per burst and 300 lines per burst cycle. Bursts were generated in such a manner that there was 100% burst overlap between all 41 images. The modified SPECAN algorithm explained in the previous chapter was utilized to process the images. Also, ScanSAR interferograms were generated using the processing chain as explained in Chapter Four. Forty ScanSAR interferograms were formed with respect to the same master reference image as was done with the stripmap data.

A small subset of the burst mode image was considered for PS analysis. A window of size  $12 \text{ km} \times 17.5 \text{ km}$  was chosen, which is aligned with the stripmap interferogram subset. The subset was of size  $157 \text{ azimuth samples} \times 850 \text{ range samples}$ , i.e. a total of 133,450 pixels. The ScanSAR interferogram resolution was 20 times coarser in the azimuth direction than the stripmap data.

### 5.3.2 Preliminary Estimation Process

The first step of the PS technique is the detection of potential PS targets based on the amplitude dispersion index. Using the set of 41 ScanSAR images that have been radiometrically corrected for antenna beam pattern, the amplitude dispersion index was calculated for each pixel. Potential PS targets were identified using a criterion that  $D_A < 0.20$ . Based on this condition a total of 6563 pixels were identified as potential PS targets, which is about 5% of the total pixels. Note that in the case of stripmap data, about 2700

pixels (0.1% of the total pixels) were identified as potential PS targets based on amplitude dispersion index.

The PS technique failed to detect any PS targets from the potential PS target list in the next step. As done in the stripmap case, pairs of potential PS targets were linked based on their proximity to each other. Each PS target was linked to every other target within a  $1.5 \text{ km} \times 1.5 \text{ km}$  window around it. The multi-image phase coherence was maximized for each link by using a 2-D grid search. However, for a selected multi-image phase coherence threshold of 0.75, none of the links were identified as PS targets. The threshold was lowered, which yielded approximately 300 links with  $\hat{\gamma} > 0.60$ . The identified PS targets were too sparse to enable the formation of a network. Lowering the threshold still further might have resulted in the identification of more PS targets, but this would be contradicting the very definition of a PS target, i.e., the presence of phase stability. Thus, the preliminary estimation process failed to detect any PS targets.

One of the reasons for not detecting any PS targets lies in the basic assumption of the PS functional model. It has been assumed that there is only one PS per ScanSAR resolution cell. However, in the case of SAR data having large resolution cells, as seen in ScanSAR data, many PS targets might fall within the same resolution cell. The return signal from these multiple PS targets may interfere with each other in either a constructive or a destructive manner. This interference is similar to the volumetric decorrelation seen in regular InSAR processing.

The ultimate purpose of the preliminary PS detection is the estimation of the residual phase maps. It is concluded here that the existing technique of estimating residual phase screens or atmospheric phase screens is not suitable when ScanSAR data is used. An alternative technique with a change in the functional model of the pixel phase is needed. Although the development of a new preliminary PS target detection method is

beyond the scope of this work, specific ideas in this direction are discussed in the last chapter of this document. To enable the continuation of this feasibility study and the final estimation process, residual phase maps were generated using the stripmap PS analysis and down-sampled to the ScanSAR image resolution. Residual-corrected differential interferograms were generated by subtracting the stripmap residual phase maps from ScanSAR differential interferograms.

### **5.3.3 Final Estimation Process**

Similar to the stripmap PS analysis, the final search for the model parameters was done on a pixel-by-pixel basis. The PS target DEM error and velocity were determined through a grid search over a range of DEM error values and deformation velocity values. As expected, very few pixels were identified as PS targets based on a multi-image phase coherence threshold of 0.75. For this threshold, a total of 225 points were identified as PS targets (Figure 5.5 (A)), which is less than 0.2% of the total number of pixels. In comparison, 66,501 PS targets were identified in stripmap PS analysis. So, only 0.3% of the PS targets identified in stripmap data were detected in ScanSAR data. Lowering the threshold to 0.65 resulted in approximately 2100 PS targets (Figure 5.5 (B)) in the ScanSAR data, which is a PS target density of  $10 \text{ PS} / \text{km}^2$ , much less than the  $312 \text{ PS} / \text{km}^2$  seen in stripmap data. The PS densities obtained in both cases, i.e. for multi-image phase coherence thresholds of 0.75 and 0.65, are not adequate to characterize the deformation velocities of the study area.

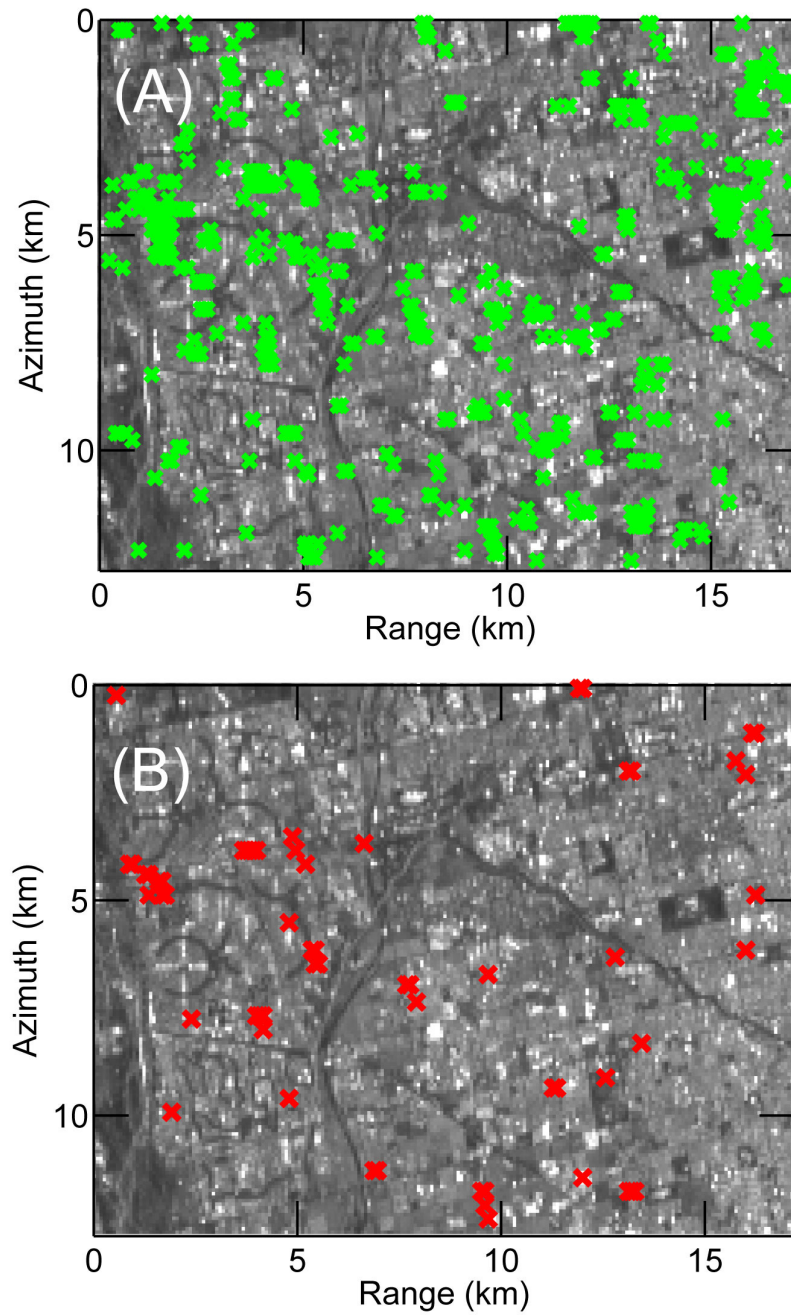


Figure 5.5: Location of PS targets identified in ScanSAR data with the usual PS technique with (A) multi-image phase coherence  $> 0.65$  and (B) multi-image phase coherence  $> 0.75$ . The single PS target per pixel model fails to detect PS targets with reasonable PS density that is required for the estimation of residual phase maps.

This analysis reaffirms the conclusion made in the previous section that the PS technique, with its present functional model, is not suitable for ScanSAR data analysis. In the next section, a multiple PS target model is formulated from the repeat-pass InSAR imaging geometry.

#### **5.4 ADAPTED PERMANENT SCATTERER TECHNIQUE AND MULTIPLE SCATTERER MODEL APPLIED TO SCANSAR DATA**

This section presents the derivation and the results pertaining to an adapted permanent scatterer technique that considers multiple PS targets being present within a single ScanSAR pixel. Starting from the basic principles of SAR backscatter and two-way signal propagation, a functional form for multiple PS model is derived. Then, the model derived in this work is compared with an existing higher-order scattering model proposed by Ferretti et al. [2005]. Finally, results obtained from the application of a two-PS model to simulated ScanSAR data are presented. Before starting into the derivation of the model, a brief discussion on the validity of the assumption that multiple PS targets can be modeled as being present within a single ScanSAR cell is presented.

Stripmap PS targets mapped into ScanSAR pixels revealed that a majority of the stripmap PS targets will be present in ScanSAR pixels having multiple PS targets (Figure 5.6). Since ScanSAR data was simulated from stripmap data, the stripmap PS target locations within the ScanSAR data were already known. Using this information, stripmap PS targets were mapped into the ScanSAR resolution cell. A multi-image phase coherence threshold of 0.75 was used in the stripmap PS analysis. When mapped into ScanSAR pixels, 23% of the PS targets identified in stripmap PS analysis are mapped into ScanSAR pixels containing a single PS target. A slightly larger fraction (25%) of the stripmap PS targets gets mapped into ScanSAR pixels that have exactly two PS targets.

Clearly more than 75% of the stripmap PS targets map into ScanSAR pixels that have multiple PS targets in them, supporting the hypothesis of the multiple PS model. Note that even in the case where only one stripmap PS target is mapped into a ScanSAR pixel, there might be other targets (with marginally lower multi-image phase coherence) within the same resolution cell that might destructively interfere with the PS target response. This is precisely the situation encountered in the single PS model as described in the previous section. For instance, if the multi-image phase coherence threshold is decreased to 0.60, then many more stripmap PS targets would be identified, and the percentage of stripmap PS targets mapping into ScanSAR pixels with multiple PS targets will increase. So, even if only one PS target per ScanSAR pixel is expected, it is worthwhile to search for multiple scatterers.

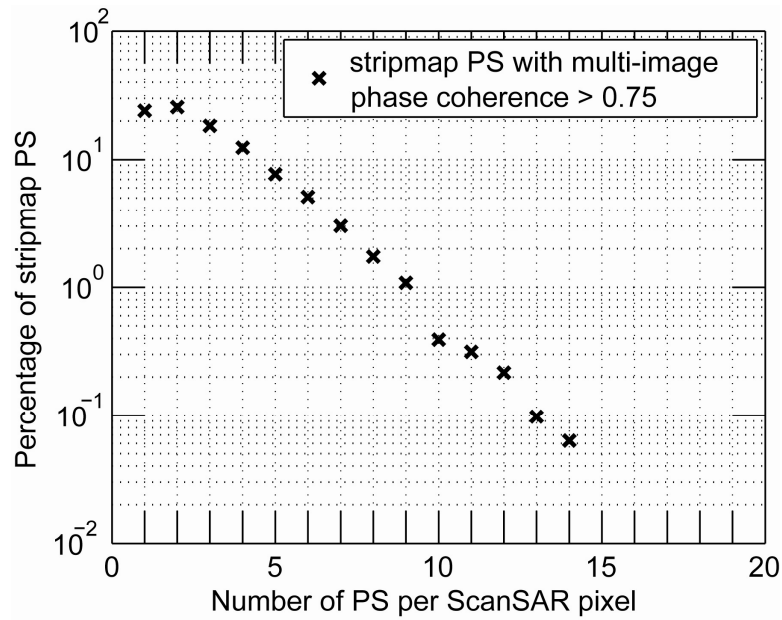


Figure 5.6: Percentage of stripmap PS targets that map into ScanSAR pixels with multiple PS targets. More than 75% of PS targets identified in the stripmap data would be present in ScanSAR pixels with more than one PS target. A multiple PS target model is needed to recover them.



### 5.4.1 Derivation of the Multiple PS Functional Model

Equations for a model expressing the differential interferometric phase of a single resolution cell of an interferogram in terms of the various interferometric parameters (e.g. viewing geometry, temporal and spatial baselines), and PS model parameters (PS target height, and PS deformation velocity) is derived. Equations are derived for a case where two targets per resolution cell are assumed. However, the generalized form of the equations can be extended to any number of PS targets. For the purpose of this derivation, a single resolution cell (represented by a single pixel in the processed image) imaged in the zero-Doppler geometry from the primary orbit is considered (Figure 5.7 (A)). Similar viewing geometry is assumed for a repeat-pass acquisition of the same resolution cell from a secondary orbit (Figures 5.7 (B)). Interferometric phase originating from the combination of the two SAR acquisitions is expressed in terms of the viewing geometry (baseline), elevation of the points representing the resolution cell above a reference surface, and the deformation of the resolution cell observed over time. The points considered here are  $P_0$  and  $P_1$  which represent the center of the resolution cell and a PS target located within the resolution cell, respectively. Although a single PS target  $P_1$  is shown in Figure 5.7 (A), multiple PS targets with similar attributes can be imagined within the same resolution cell.

#### *Interferometric Phase due to the Reference Surface (DEM)*

First the interferometric phase associated with the reference surface  $P_0$  is derived in terms of the baseline and slant range geometry. From Figure 5.6 (B), the look vector  $\vec{\rho}_0$  from  $S_0$  to  $P_0$  in the TCN reference frame can be written as:

$$\vec{\rho}_0 = -\rho_0 \sin \theta_0 \hat{c} - \rho_0 \cos \theta_0 \hat{n} \quad (5.14)$$



Also from Figure 5.6 (B), the baseline vector  $\vec{B}$  from  $S_0$  to  $S_1$ , which is in the zero-Doppler plane, can be written in terms of its components in the  $\hat{c}$  and  $\hat{n}$  axes as:

$$\vec{B} = -B_c \hat{c} - B_n \hat{n} \quad (5.15)$$

Then the parallel baseline  $B_{\parallel 0}$  with respect to  $P_0$  is:

$$B_{\parallel 0} = \hat{\rho}_0 \cdot \vec{B} = B_c \sin \theta_0 + B_n \cos \theta_0 \quad (5.16)$$

The vector  $\hat{l}_0$ , which is perpendicular to the look-vector, can be defined as the cross product between the look-vector  $\hat{\rho}_0$  and the transverse vector  $\hat{t}$ :

$$\hat{l}_0 = \hat{\rho}_0 \times \hat{t} = -\cos \theta_0 \hat{c} + \sin \theta_0 \hat{n} \quad (5.17)$$

Using the  $\hat{l}_0$  vector, the perpendicular baseline  $B_{\perp 0}$  with respect to  $P_0$  can be written as:

$$B_{\perp 0} = \hat{l}_0 \cdot \vec{B} = B_c \cos \theta_0 - B_n \sin \theta_0 \quad (5.18)$$

Now the range vector to  $P_0$  from the secondary satellite position  $S_1$  can be expressed as:

$$\vec{\rho}_{0B} = \vec{\rho}_0 - \vec{B} = (B_c - \rho_0 \sin \theta_0) \hat{c} + (B_n - \rho_0 \cos \theta_0) \hat{n} \quad (5.19)$$

The difference between the range to  $P_0$  from  $S_0$  and the range to  $P_0$  from  $S_1$  is:

$$\begin{aligned}\vec{\rho}_{0B} &= \vec{\rho}_0 - \vec{B} \\ &= (B_c - \rho_0 \sin \theta_0) \hat{c} + (B_n - \rho_0 \cos \theta_0) \hat{n}\end{aligned}\tag{5.20}$$

Then the interferometric phase corresponding to the center for the resolution cell  $P_0$  can be expressed as:

$$\phi_{ref}^{int} = -\frac{4\pi}{\lambda} \delta \rho_0 = -\frac{4\pi}{\lambda} \rho_0 \left( \sqrt{1 - \frac{2B_{||0}}{\rho_0} + \frac{B^2}{\rho_0^2}} - 1 \right)\tag{5.21}$$

### ***Interferometric Baselines with Respect to a PS Target***

Since the interferometric phase is a function of the baseline, the perpendicular and parallel components of the baseline with respect to the PS target location are computed here. Equations for a single PS target  $P_1$  are derived, which can be generalized for any number of targets. The look vector  $\vec{\rho}_1$  from  $S_0$  to  $P_1$  can be written in the TCN reference frame as:

$$\vec{\rho}_1 = \rho_1 \sin \theta_{sq1} \hat{t} - \rho_1 \sqrt{1 - \sin^2 \theta_{sq1} - \cos^2 \theta_1} \hat{c} - \rho_1 \cos \theta_1 \hat{n}\tag{5.22}$$

where  $\theta_{sq1}$  is the squint angle between the slant range vector to target  $P_1$  and the zero-Doppler plane (Figure 5.6(B)). The parallel baseline component with respect to  $P_1$  is:

$$B_{||1} = \hat{\rho}_1 \cdot \vec{B} = B_c \sqrt{1 - \sin^2 \theta_{sq1} - \cos^2 \theta_1} + B_n \cos \theta_1\tag{5.23}$$

As in the case of Equation 5.18, the perpendicular baseline component with respect to point  $P_1$  can be derived as:

$$B_{\perp 1} = B_c \cos \theta_1 - B_n \sqrt{1 - \sin^2 \theta_{sq1} - \cos^2 \theta_1} \quad (5.24)$$

### ***Interferometric Phase due to two PS Targets***

Now consider the case of multiple PS targets present in the same resolution cell. Suppose there are two targets  $P_1$  and  $P_2$  in the same resolution cell with complex backscatter coefficients  $C_1$  and  $C_2$ , respectively. The complex backscatters can be expressed in terms of the real valued backscatter amplitudes ( $A_{bs1}, A_{bs2}$ ) and phases ( $\psi_{bs1}, \psi_{bs2}$ ) as:

$$C_1 = A_{bs1} \exp\{-j\psi_{bs1}\} \quad (5.25a)$$

$$C_2 = A_{bs2} \exp\{-j\psi_{bs2}\} \quad (5.25b)$$

The received response associated with the two-way propagation of the radar signal to the resolution cell in the master scene can be written as:

$$R_1 = C_1 \exp\left\{-j\frac{4\pi}{\lambda}\rho_1\right\} + C_2 \exp\left\{-j\frac{4\pi}{\lambda}\rho_2\right\} \quad (5.26)$$

Similarly, the received response in the secondary scene can be written as:

$$R_2 = C_1 \exp\left\{-j\frac{4\pi}{\lambda}(\rho_{1B} + \mu_1)\right\} + C_2 \exp\left\{-j\frac{4\pi}{\lambda}(\rho_{2B} + \mu_2)\right\} \quad (5.27)$$

where  $\rho_{1B}$  and  $\rho_{2B}$  are the slant ranges to the targets  $P_1$  and  $P_2$ , respectively, from the secondary satellite position  $S_1$ , and  $\mu_1$  and  $\mu_2$  are the displacements of the scatterers in

the radar line of sight in the time spanned by the two scenes. If it is assumed that all scatterers present in a single resolution cell move by the same amount, then:

$$\mu_1 = \mu_2 = \mu \quad (5.28)$$

Using this assumption, the raw interferogram  $I$  formed from the two return signals can be written as:

$$\begin{aligned} I &= R_1 R_2^* \\ &= \left( C_1 \exp\left\{-j \frac{4\pi}{\lambda} \rho_1\right\} + C_2 \exp\left\{-j \frac{4\pi}{\lambda} \rho_2\right\} \right) \cdot \times \\ &\quad \cdot \left( C_1^* \exp\left\{j \frac{4\pi}{\lambda} \rho_{1B}\right\} + C_2^* \exp\left\{j \frac{4\pi}{\lambda} \rho_{2B}\right\} \right) \exp\left\{j \frac{4\pi}{\lambda} \mu\right\} \\ &= \left[ C_1 C_1^* \exp\left\{-j \frac{4\pi}{\lambda} (\rho_1 - \rho_{1B})\right\} + C_1 C_2^* \exp\left\{-j \frac{4\pi}{\lambda} (\rho_1 - \rho_{2B})\right\} + \right. \\ &\quad \left. C_2 C_1^* \exp\left\{-j \frac{4\pi}{\lambda} (\rho_2 - \rho_{1B})\right\} + C_2 C_2^* \exp\left\{-j \frac{4\pi}{\lambda} (\rho_2 - \rho_{2B})\right\} \right] \exp\left\{-j \frac{4\pi}{\lambda} \mu\right\} \end{aligned} \quad (5.29)$$

Since all targets are located in the same resolution cell, it is assumed that the two targets,  $P_1$  and  $P_2$ , are at the same slant range which is equal to the slant range to the center of the resolution cell in the master scene:

$$\rho_1 = \rho_2 = \rho_0 \quad (5.30)$$

With this assumption, the interferometric signal  $I$  can be written as:

$$I = \left[ \xi_1 \exp\left\{-j \frac{4\pi}{\lambda} (\rho_0 - \rho_{1B})\right\} + \xi_2 \exp\left\{-j \frac{4\pi}{\lambda} (\rho_0 - \rho_{2B})\right\} \right] \exp\left\{-j \frac{4\pi}{\lambda} \mu\right\} \quad (5.31)$$

where

$$\xi_1 = (C_1 C_1^* + C_2 C_1^*) \quad (5.32a)$$

$$\xi_2 = (C_1 C_2^* + C_2 C_2^*) \quad (5.32b)$$

and  $\xi_1$  and  $\xi_2$  are, in general, complex-valued. From the interferometric signal shown in Equation 5.31, the interferometric phase contribution due to the center of the resolution cell  $\phi_{ref}^{int}$  (Equation 5.21) is removed. Then the resulting differential interferometric signal

$D$  can be expressed as:

$$\begin{aligned} D &= (R_1 R_2^*) \exp\{-j \phi_{ref}^{int}\} \\ &= \left[ \xi_1 \exp\left\{-j \frac{4\pi}{\lambda} (\rho_0 - \rho_{1B})\right\} + \xi_2 \exp\left\{-j \frac{4\pi}{\lambda} (\rho_0 - \rho_{2B})\right\} \right] \times \\ &\quad \exp\left\{-\frac{4\pi}{\lambda} \delta \rho_0\right\} \exp\left\{-j \frac{4\pi}{\lambda} \mu\right\} \end{aligned} \quad (5.33)$$

The differential interferometric signal in Equation 5.33 can be written in terms of the difference between the differential path delays as:

$$D = \left[ \xi_1 \exp\left\{j \frac{4\pi}{\lambda} (\delta \rho_1 - \delta \rho_0)\right\} + \xi_2 \exp\left\{j \frac{4\pi}{\lambda} (\delta \rho_2 - \delta \rho_0)\right\} \right] \exp\left\{-j \frac{4\pi}{\lambda} \mu\right\} \quad (5.34)$$

where,

$$\delta\rho_1 = \sqrt{\rho_0^2 + B^2 - 2\rho_0 B_{\parallel 1}} - \rho_0 = \rho_0 \left( \sqrt{1 - \frac{2B_{\parallel 1}}{\rho_0} + \frac{2B^2}{\rho_0^2}} - 1 \right) \quad (5.35a)$$

$$\delta\rho_2 = \sqrt{\rho_0^2 + B^2 - 2\rho_0 B_{\parallel 2}} - \rho_0 = \rho_0 \left( \sqrt{1 - \frac{2B_{\parallel 2}}{\rho_0} + \frac{2B^2}{\rho_0^2}} - 1 \right) \quad (5.35b)$$

Note that we can make use of the binomial expansion:

$$\sqrt{1 + \varepsilon} = 1 + \frac{\varepsilon}{2} + \dots \quad (5.36)$$

where

$$\varepsilon = \frac{B^2 - 2\rho_0 B_{\parallel 0}}{\rho_0^2} < 1 \quad (5.37)$$

since  $B_{\parallel 0}, B \ll \rho_0$ . The difference between the differential path lengths can be written as:

$$(\delta\rho_1 - \delta\rho_0) = \rho_0 \left[ 1 + \frac{1}{2} \left( -\frac{2B_{\parallel 1}}{\rho_0} + \frac{B^2}{\rho_0^2} \right) + \dots \right] - \rho_0 \left[ 1 + \frac{1}{2} \left( -\frac{2B_{\parallel 0}}{\rho_0} + \frac{B^2}{\rho_0^2} \right) + \dots \right] \quad (5.38)$$

A similar expression can be written for  $\delta\rho_2 - \delta\rho_0$ . If we ignore higher order terms, then

Equation 5.38 (and its counterpart for the second target) can be written as:

$$(\delta\rho_1 - \delta\rho_0) \cong (B_{\parallel 0} - B_{\parallel 1}) \quad (5.39a)$$

$$(\delta\rho_2 - \delta\rho_0) \cong (B_{\parallel 0} - B_{\parallel 2}) \quad (5.39b)$$



Based on the expressions for the parallel baseline components as written in Equations 5.16 and 5.23, the right hand sides of Equations 5.39a and 5.39b can be written as:

$$(B_{\parallel 0} - B_{\parallel 1}) = (B_c \sin \theta_0 + B_n \cos \theta_0) - B_c \sqrt{(1 - \sin^2 \theta_{sq1} - \cos^2 \theta_1)} - B_n \cos \theta_1 \quad (5.40a)$$

$$(B_{\parallel 0} - B_{\parallel 2}) = (B_c \sin \theta_0 + B_n \cos \theta_0) - B_c \sqrt{(1 - \sin^2 \theta_{sq2} - \cos^2 \theta_2)} - B_n \cos \theta_2 \quad (5.40b)$$

The squint angles  $(\theta_{sq1}, \theta_{sq2})$  caused by the sub-pixel azimuth location of the scatterers are very small, i.e.,  $\theta_{sq1}, \theta_{sq2} \ll 1$ . In the case of a typical ERS geometry, if the sub-pixel azimuth location of the PS target is about 50 meters from the center of the pixel, then the squint angle is  $6 \times 10^{-5}$  radians. In such cases,  $\sin^2 \theta_{sq1}$  can be considered as negligible. Thus, ignoring the squint angle terms, Equations 5.40a and 5.40b can be simplified as:

$$(B_{\parallel 0} - B_{\parallel 1}) = (B_c \sin \theta_0 + B_n \cos \theta_0) - B_c \sin \theta_1 - B_n \cos \theta_1 \quad (5.41a)$$

$$(B_{\parallel 0} - B_{\parallel 2}) = (B_c \sin \theta_0 + B_n \cos \theta_0) - B_c \sin \theta_2 - B_n \cos \theta_2 \quad (5.41b)$$

Also, the difference in the look angle between  $\theta_0$  and  $\theta_1$  and between  $\theta_0$  and  $\theta_2$  is very small:

$$\theta_1 = \theta_0 + \delta\theta_1 \quad (5.42a)$$

$$\theta_2 = \theta_0 + \delta\theta_2 \quad (5.42b)$$

where  $\delta\theta_1, \delta\theta_2 \ll 1$ . Consequently, the following relations are valid:

$$\sin \theta_1 = \sin(\theta_0 + \delta\theta_1) \cong \sin \theta_0 + \cos \theta_0 \delta\theta_1 \quad (5.43a)$$

$$\cos \theta_1 = \cos(\theta_0 + \delta\theta_1) \cong \cos \theta_0 - \sin \theta_0 \delta\theta_1 \quad (5.43b)$$

Similar trigonometric relations can be written for  $\theta_2$ . Substituting Equations 5.43a and 5.43b in Equations 5.41a, the difference in baselines can be written as:

$$\begin{aligned} (B_{\parallel 0} - B_{\parallel 1}) &\cong (B_c \sin \theta_0 + B_n \cos \theta_0) - B_c (\sin \theta_0 + \cos \theta_0 \delta\theta_1) - B_n (\cos \theta_0 - \sin \theta_0 \delta\theta_1) \\ &= [-B_c (\cos \theta_0) + B_n (\sin \theta_0)] \delta\theta_1 \\ &= -B_{\perp 0} \delta\theta_1 \end{aligned} \quad (5.44a)$$

Similarly:

$$(B_{\parallel 0} - B_{\parallel 2}) = -B_{\perp 0} \delta\theta_2 \quad (5.44b)$$

The change in look angle can be related to change in elevation above the reference surface (DEM) as:

$$\delta\theta_1 = \frac{\Delta z_1}{\rho_0 \sin \theta_0} \quad (5.45a)$$

$$\delta\theta_2 = \frac{\Delta z_2}{\rho_0 \sin \theta_0} \quad (5.45b)$$

where  $\Delta z_1$  and  $\Delta z_2$  are the heights of the targets at  $P_1$  and  $P_2$ , respectively, above the reference point  $P_0$ . Using Equations 5.35, 5.39, 5.44 and 5.45, and by making appropriate substitutions, the equation for differential interferometric signal is obtained:

$$D = \left[ \xi_1 \exp \left\{ -j \frac{4\pi}{\lambda} B_{\perp 0} \frac{\Delta z_1}{\rho_0 \sin \theta_0} \right\} + \xi_2 \exp \left\{ -j \frac{4\pi}{\lambda} B_{\perp 0} \frac{\Delta z_2}{\rho_0 \sin \theta_0} \right\} \right] \exp \left\{ -j \frac{4\pi}{\lambda} \mu \right\} \quad (5.46)$$

Thus, the differential interferometric phase in the  $k^{th}$  interferogram can be expressed using the model:

$$D^k = [\xi_1 \exp\{j\beta^k \Delta z_1\} + \xi_2 \exp\{j\beta^k \Delta z_2\}] \exp\{j\alpha^k v\} \quad (5.47)$$

The two PS per pixel model derived here can be generalized as an M number of PS per pixel model in a straightforward way as:

$$D^k = \sum_{m=1}^M \xi_m \exp\{j(\beta^k \Delta z_m + \alpha^k v)\} \quad (5.48)$$

#### 5.4.2 Comparison with a Previous Higher-order Scatter Model

The PS functional model derived in the previous section is similar to the one proposed by Ferretti et al. [2005] where multiple PS targets are assumed at different sub-range locations. However, there are certain differences between the assumptions made in the derivation of the two models.

Ferretti et al. [2005] assume that the multiple PS targets are located at different sub-pixel range locations, in the slant range direction, within the same resolution cell. Ferretti et al. [2005] search for multiple PS targets contained within the same resolution cells of stripmap data. In stripmap data, resolution in range is lower than the resolution in azimuth which validates the assumption of having multiple targets distributed along the

slant range direction. Furthermore, Ferretti et al. [2005] assume a linear relationship between the PS target sub-pixel range location and the PS target height error. Ferretti et al. [2005] conclude that use of a two PS model instead of a single scatterer model resulted in a 20% increase in the detection of PS targets in stripmap data.

In the model derived as part of this research, it is assumed that all the PS targets are at the same slant range. No specific assumption is made about the PS target sub-pixel range and sub-pixel azimuth locations. In other word, PS targets are assumed to be located on a spherical surface whose radius is equal to the slant range to the pixel and within the confines of the azimuth extent of the pixel. In this study, the multiple PS model is applied to ScanSAR data in which the azimuth resolution is much lower than the slant range resolution. So the chances of having multiple PS targets at different sub-pixel azimuth location are much higher. However, it was found that the derived model is not sensitive to the azimuth sub-pixel location of the PS target.

### 5.4.3 Estimation of Model Parameters

The problem of solving for the various model parameters of Equation 5.48 is a problem of nonlinear estimation. In Equation 5.48,  $\xi_m$ ,  $\Delta z_m$  and  $v$  are the parameters that are to be estimated, while  $\beta^k$  and  $\alpha^k$  are the constants of proportionality that relate the interferometric phase to the estimated parameters. For a model that has M PS targets, a total of 4M+1 real-valued parameters have to be estimated. These include a 2 real valued parameters corresponding to the complex coefficient ( $\xi_m$ ) for each scatterer, the DEM error ( $\Delta z_m$ ) of each scatterer, and a deformation velocity  $v$  that is same for all targets.

A nonlinear least squares method provided in [Stoica and Moses, 1997] and utilized by Ferretti et al. [2005] is used for the estimation of the various parameters of the

model presented here. Since the functional model of the model derived in this study is similar to the one proposed by Ferretti et al. [2005], the same estimation approach was deemed applicable. The approach of estimating unknown parameters using nonlinear least squares method involves the minimization of an objective function. The objective function is defined as the summation over all data samples of the squares of the differences between the estimated model and data. For an M PS model, the objective function  $J$  for each pixel can be defined as:

$$J = \sum_{k=1}^N \left| y_k - \sum_{m=1}^M \xi_m \exp\{j(\beta^k \Delta z_m + \alpha^k v)\} \right|^2 \quad (5.49)$$

where  $y_k$  is the complex-valued pixel data in the  $k^{th}$  interferogram, M is the number of targets within a resolution cell, and N is the number of interferograms. Note that the same velocity  $v$  has been assumed for all targets in the resolution cell. The following part of the derivation is borrowed from [Stoica and Moses, 1997] and adapted to the problem relevant to this research. The notation similar to that used by Stoica and Moses [1997] is adapted here to represent the model parameters and the data in matrix notation:

$$\underline{x} = [\xi_1 \quad \xi_2 \quad \cdot \quad \cdot \quad \xi_M]^T \quad (5.50)$$

$$\underline{\underline{A}} = \begin{bmatrix} \exp\{\beta^1 \Delta z_1 + \alpha^1 v\} & \exp\{\beta^1 \Delta z_2 + \alpha^1 v\} & \cdot & \cdot & \exp\{\beta^1 \Delta z_M + \alpha^1 v\} \\ \exp\{\beta^2 \Delta z_1 + \alpha^2 v\} & \cdot & \cdot & \cdot & \cdot \\ \cdot & \cdot & \cdot & \cdot & \cdot \\ \cdot & \cdot & \cdot & \cdot & \cdot \\ \exp\{\beta^N \Delta z_1 + \alpha^N v\} & \cdot & \cdot & \cdot & \exp\{\beta^N \Delta z_M + \alpha^N v\} \end{bmatrix} \quad (5.51)$$

$$\underline{Y} = [y_1 \quad y_2 \quad \cdot \quad \cdot \quad y_N]^T \quad (5.52)$$

The objective function can now be written using matrix notation as:

$$J = (\underline{Y} - \underline{\underline{A}}\underline{x})^H (\underline{Y} - \underline{\underline{A}}\underline{x}) \quad (5.53)$$

where H represents a complex transpose operation. The rank of the matrix  $\underline{\underline{A}}$  is equal to M under the conditions that  $M < N$  and  $\Delta z_p \neq \Delta z_q$  for  $p \neq q$ . In such circumstances the inverse of the matrix  $(\underline{\underline{A}}^H \underline{\underline{A}})$  exists, and the objective function can be re-written as [Stoica and Moses, 1997]:

$$J = \left[ \underline{x} - (\underline{\underline{A}}^H \underline{\underline{A}})^{-1} \underline{\underline{A}}^H \underline{Y} \right]^H (\underline{\underline{A}}^H \underline{\underline{A}}) \left[ \underline{x} - (\underline{\underline{A}}^H \underline{\underline{A}})^{-1} \underline{\underline{A}}^H \underline{Y} \right] + \left[ \underline{Y}^H \underline{Y} - \underline{Y}^H \underline{\underline{A}} (\underline{\underline{A}}^H \underline{\underline{A}})^{-1} \underline{\underline{A}}^H \underline{Y} \right] \quad (5.54)$$

For every set of chosen parameters  $\underline{p} = [\Delta z_1, \Delta z_2, \dots, \Delta z_M, v]$  of the model contained in matrix  $\underline{\underline{A}}$ , parameters in  $\underline{x}$  can be chosen in a manner so as to make the first term (inside the square brackets) of the objective function in Equation 5.54 equal to zero. Although the objective function is dependent on the parameters in  $\underline{x}$  as well as the parameters in  $\underline{\underline{A}}$ , the “nuisance parameters” in  $\underline{x}$  can be separated in the following way. The vectors  $\underline{x}$  and  $\underline{p}$  that minimize the objective function are:

$$\hat{\underline{p}} = \arg \max_{\underline{p}} [\underline{Y}^H \underline{\underline{A}} (\underline{\underline{A}}^H \underline{\underline{A}})^{-1} \underline{\underline{A}}^H \underline{Y}] \quad (5.55a)$$

$$\hat{\underline{x}} = (\underline{\underline{A}}^H \underline{\underline{A}})^{-1} \underline{\underline{A}}^H \underline{Y} \Big|_{\underline{p}=\hat{\underline{p}}} \quad (5.55b)$$

While estimation of all the parameters is necessary, it is desirable to separate the estimation of the phase related parameters ( $\Delta z_m$  and  $v$ ) from the complex backscatter

related parameters ( $\xi_m$ ). The two-step process of estimation, shown in Equations 5.55a and 5.55b, is helpful in reducing the number of parameters that have to be searched in a grid search based technique. In the first step, a grid search is used to maximize the new objective function as defined in (Equation 5.55a). Next, the solution that maximizes the objective function in Equation 5.55a is used to calculate the complex coefficients in 5.55b.

For a model with two PS targets per pixel, i.e.  $M=2$ , a total of 7 real-valued parameters have to be estimated. They include 3 real-valued parameters  $\Delta\hat{z}_1, \Delta\hat{z}_2, \hat{v}$  and 4 backscatter parameters corresponding to the 2 complex-valued backscatter coefficients  $\hat{\xi}_1$  and  $\hat{\xi}_2$ . Based on Equations in 5.55, the estimation process can be divided into two steps. First a three-dimensional grid search is carried to estimate the parameters that maximize the new objective function defined in 5.55a. Then based on the estimated real-valued parameters  $\hat{p}$ , the complex-valued parameters  $\hat{x}$  are estimated using Equation 5.55b. Using the 7 real-valued parameters, the model phase is calculated as:

$$\hat{y}_k = \hat{\xi}_1 \exp\{j(\beta^k \Delta\hat{z}_1 + \alpha^k \hat{v})\} + \hat{\xi}_2 \exp\{j(\beta^k \Delta\hat{z}_2 + \alpha^k \hat{v})\} \quad (5.56)$$

Then the new multi-image phase coherence for this model is defined as [Ferretti et al., 2005]:

$$\gamma_{II} = \left| \frac{1}{N} \sum_{k=1}^N \exp\{j\angle y_k\} \exp\{-j\angle \hat{y}_k\} \right| \quad (5.57)$$

where  $y_k$  is the complex valued data corresponding to the  $k^{th}$  interferogram,  $\hat{y}_k$  is the estimated complex-valued value of the  $k^{th}$  interferogram from the model, and

$\angle$  represents the phase of a complex number. Equation 5.57 is basically an average of the summation over the stack of the interferograms of the complex vector phase differences between the data and the model. Note that the multi-image phase coherence of the two PS model is analogous to the single PS target model. The reason for considering only the phase dispersion and not the complex-valued differences in the estimated model is that the emphasis of the technique is on accurately detecting the deformation phase and not the amplitude of the PS targets [Ferretti et al., 2005].

For every pixel of ScanSAR image subsets, deformation velocity and DEM error estimates were found by searching on a 3-D grid. Two axes of the 3-D grid were spanned by the DEM error values ranging between -25 and 25 meters, and the third axis was spanned by velocity values ranging between -2 and +4 cm/year. DEM error values were searched at an interval of 0.5 meters, and velocities were searched at intervals of 0.1 cm/year. Since it has been assumed that  $\Delta z_p \neq \Delta z_q$ , the corresponding cases were skipped while performing the grid search.

### ***Computational Considerations***

The computational requirements for estimating the parameters of multiple PS model can be huge, even for a basic case of two PS targets per pixel. The number of  $\gamma_{II}$  evaluations per pixel for the 3 parameter search were  $((101 \times 101 - 1) \times 61) = 616,100$ . In comparison, the 2-D search for a single PS target per pixel required  $101 \times 61 = 6161$  evaluations of  $\gamma_{II}$  at each pixel location. Clearly, as the complexity of the model increases, i.e., as the number of PS targets per cell increases, the computational requirements increase geometrically where the geometric ratio is the number of search steps per parameter. For a small subset of the interferogram, which is  $12.5 \text{ km} \times 17 \text{ km}$  in size, the total number of  $\gamma_{II}$  evaluations is on the order of  $10^9$ . Also, compared to the



single PS model, the multiple PS model has an additional step where the complex backscatter coefficients (Equation 5.55b) are estimated. This additional step which, is performed after the grid search, increases the time requirements of the estimation process in the multiple scatterer model.

The time required to complete a grid search based estimation process is dependent on the speed of the processor. On a dual processor machine (CPU speed 2391 MHz) dedicated for SAR processing located at the Center for Space Research (CSR), a 3-parameter search took approximately 8 days to compute. Evidently, increasing the order of the search to 4 parameters will make the grid search last for months on the same machine. Since the objective of this work is to study the feasibility of PSInSAR analysis and the derivation of a new functional model, actual implementation of the model for a case with a large number of PS targets per cell was considered beyond the scope of this work. Parallel processing methods that utilize multi-node processors can be used to speed up the search. Also, novel estimation algorithms can be utilized to improve the efficiency of the parameter search.

#### **5.4.4 Results from the Multiple PS Model**

In the section, velocity and DEM error estimates for PS targets identified in ScanSAR data using the multiple PS model are presented. Also, the validation of the results from a two PS model using the results from single scatterer PS analysis of stripmap data is discussed. Before presenting the results, some important aspects of the processing steps are revised.

The model derived as part of this research address the feasibility of performing a pixel-by-pixel PS analysis of ScanSAR data. This model is applicable to the final search step of the original PS algorithm used in stripmap PS analysis. The multiple PS model

does not address the process of generating residual phase screens or atmospheric phase screens directly from ScanSAR data. Residual phase screens generated from stripmap PS analysis were down-sampled and used in ScanSAR PS analysis.

PS targets in ScanSAR data were detected using the basic version of the multiple-PS model. The two PS model and the estimation process described in the previous two sections were applied to the stack of 40 ScanSAR interferograms. It was assumed that there are exactly two PS per ScanSAR pixel. The two PS model might not be applicable to all pixels of the interferogram. However, for the purpose of evaluating the feasibility of this model, and due to computational considerations, the two PS model was adapted. In general, there can be a variable number of PS targets per ScanSAR resolution cell depending on the size of the cell.

It is observed that the multi-image phase coherence is much higher for the two PS model than for the single PS model. Figure 5.8 shows a map of pixels identified as PS targets using the two PS model from ScanSAR interferograms. Notice that many more ScanSAR pixels were identified as PS targets using the two PS model compared to the single PS model (Figure 5.5). For a threshold of  $\hat{\gamma}_{II} > 0.75$ , 7% of the total pixels in the subset of the ScanSAR image were identified as PS targets. The PS target density was 44 PS / km<sup>2</sup>. When the threshold was lowered to 0.65, 20% of the total pixels were identified as PS targets. In this case, a PS target density of 120 PS / km<sup>2</sup> was observed, which is a reasonable density required for estimating residual phase maps. Compared to results of one scatterer model applied to ScanSAR data, there is a 110% increase in the PS density.

Velocity maps (Figures 5.9 (A) and 5.9 (B)) are generated for pixels identified in the ScanSAR interferograms as PS targets using the two PS model with criteria  $\hat{\gamma}_{II} > 0.75$  and  $\hat{\gamma}_{II} > 0.65$ , respectively. By lowering the threshold on the multi-image phase coherence, a significantly higher number of PS pixels (and their velocities) were

identified. However, this comes at the risk of accepting pixels with larger phase dispersion.

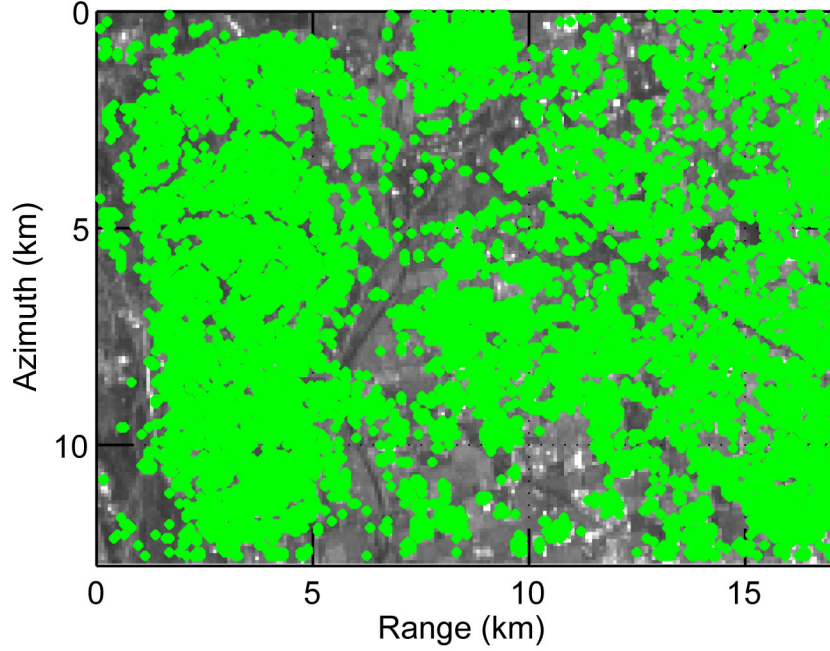


Figure 5.8: PS targets identified in ScanSAR data using two PS targets per pixel model. All pixels with multi-image phase coherence  $> 0.75$  are considered PS targets.

Multi-image phase coherence obtained from the multiple PS model is not an absolute measure of phase dispersion. If parameter estimation through both a single PS model and a multiple PS model result in a high multi-image phase coherence, then a simple comparison of the multi-image phase coherence is not sufficient to determine which model is more appropriate. In other words, it is not necessarily true that if  $\hat{\gamma}_H > \hat{\gamma} > \gamma_0$ , then the two PS model is a better fit than a single PS model. If the two models provide comparable multi-image phase coherence, then the actual standard deviation in phase dispersion should be calculated.

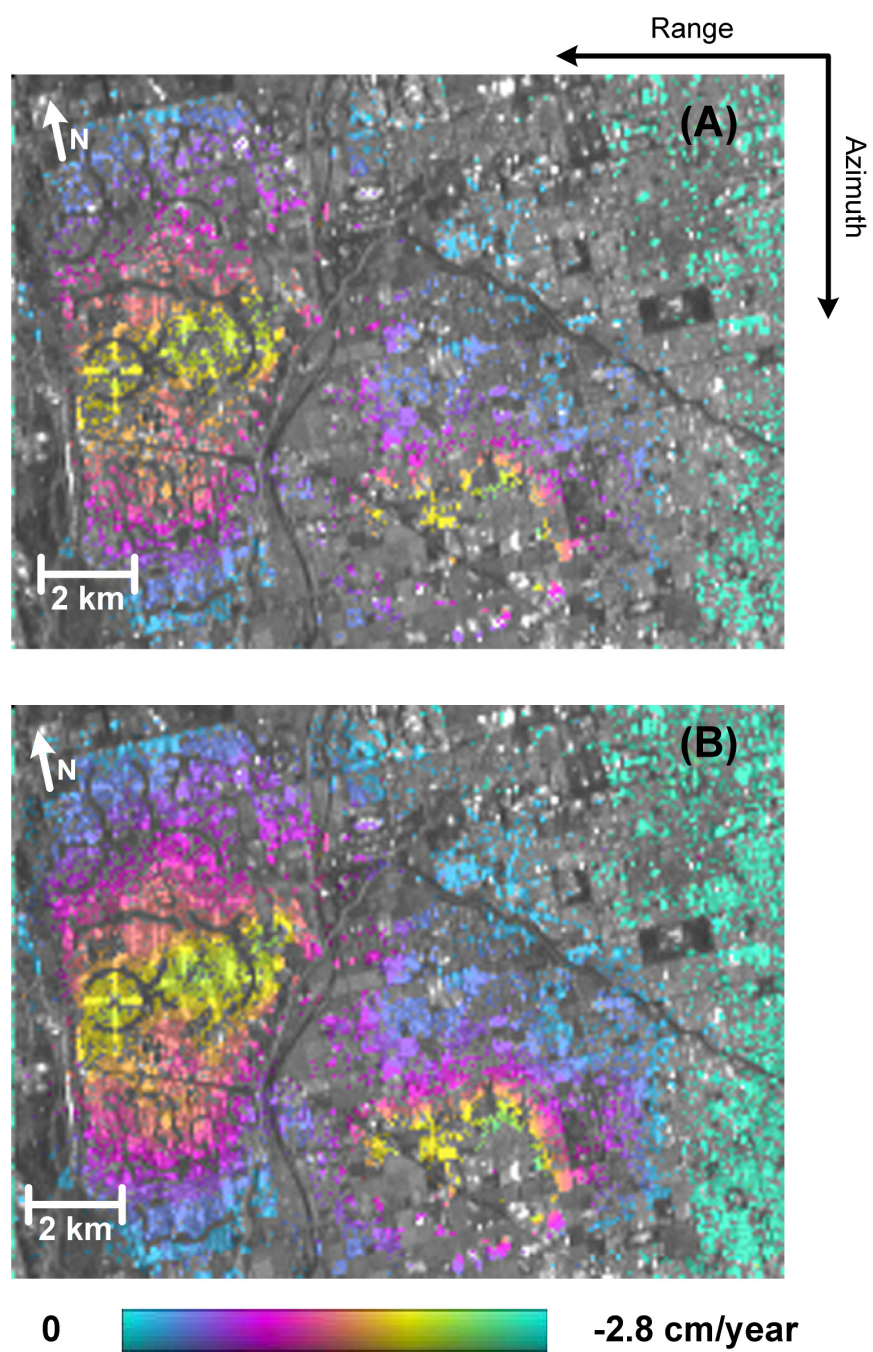


Figure 5.9: ScanSAR PS line-of-sight velocity maps for pixels identified with two PS targets per pixel using (A) a multi-image phase coherence  $> 0.75$  (B) a multi-image phase coherence  $> 0.65$ .

To validate the results of the two PS model, PS velocities obtained from ScanSAR interferograms were compared with PS velocities obtained from the single target model stripmap PS analysis. ScanSAR pixels that were expected to contain exactly two stripmap PS targets in them were considered for validation purposes. In the case of ScanSAR PS analysis, it was assumed that both PS targets within a pixel move at the same velocity. If two stripmap PS targets having different velocities are mapped into a single ScanSAR pixel, then the average stripmap velocity of the two targets was considered for comparison. If the two stripmap velocities being averaged are fairly difference, then it means that the basic assumption of all targets in the pixel having the same velocity is not valid. In such a case, large deviations in velocity and DEM errors may be expected. While comparing the DEM errors, estimated values from stripmap PS analysis and ScanSAR PS analysis were arranged in descending order, i.e., the smaller estimated DEM errors were compared with each other.

To quantify the validation, histograms showing the differences between ScanSAR PS velocities obtained from the two PS model and the stripmap PS velocities obtained from single PS mode were computed (Figures 5.10 (A) and (B)). Similar histograms were computed showing the differences in estimated DEM errors (Figures 5.11 (A) and (B)) Since the velocities of PS targets were searched at 0.1 cm intervals, velocity differences can be measured only in steps of 0.1 cm/year. So a bin spacing of 0.1 cm/year was used. Similarly, for histograms of the DEM error differences (Figure 5.11), a bin spacing of 0.5 meters was used.

### ***Discussion***

A significant percentage (40%) of the PS target velocity differences are in the zero-difference bin of the histograms (Figures 5.10). More than 93% of the velocity

differences seen in the case of  $\hat{\gamma}_{II} > 0.75$  are within one search step interval, indicating that there is a reasonably good agreement between stripmap and ScanSAR PS velocities. The percentage of ScanSAR PS targets having larger velocity variations with respect to stripmap PS velocities increases marginally when the threshold on  $\hat{\gamma}_{II}$  is lowered to 0.65 (Figure 5.10 (B)).

Validation of the DEM error estimates obtained from the ScanSAR two PS model revealed that the accuracy of the estimates was relatively low. From the histograms in Figures 5.11 (A) and (B), it is clear that the DEM error differences are distributed about the zero mean but with a large variation. The deviations between ScanSAR and stripmap PS DEM errors suggest that DEM error estimates are not as satisfactory the velocity estimates. The standard deviation in the DEM error differences are 7.1 meters ( $\hat{\gamma}_{II} > 0.75$ ) and 7.2 meters ( $\hat{\gamma}_{II} > 0.65$ ). From these results, it appears that the two PS model is not estimating the DEM error values accurately.

However, the process of validation (comparison of stripmap and ScanSAR PS models and taking differences) considered above is not infallible. Some key assumptions are identified here that make the validation process less than ideal. For the purpose of validation, it has been assumed that there are exactly two dominant PS targets present in the ScanSAR pixel. The validity of this assumption is not guaranteed even if the estimated multi-image phase coherence is higher than the threshold. Also, it is assumed that the ScanSAR and stripmap images are perfectly co-aligned. However, small errors in the co-registration of the ScanSAR to stripmap images can create a mismatch in the mapping of stripmap PS targets into ScanSAR resolution cells. In other words, some of the stripmap PS targets were not mapped to their correct ScanSAR pixel. Hence, for these targets a comparison of stripmap and ScanSAR estimates will not be valid. For example, based on the low resolution of ScanSAR data, it is estimated that 20 pixels of stripmap

data map into a single ScanSAR pixel. Even a small offset error of 1/20 of a ScanSAR pixel between stripmap and ScanSAR images may result in the mismatch of the targets being compared. This is especially true for targets that are present at the edge of a large ScanSAR resolution cell.

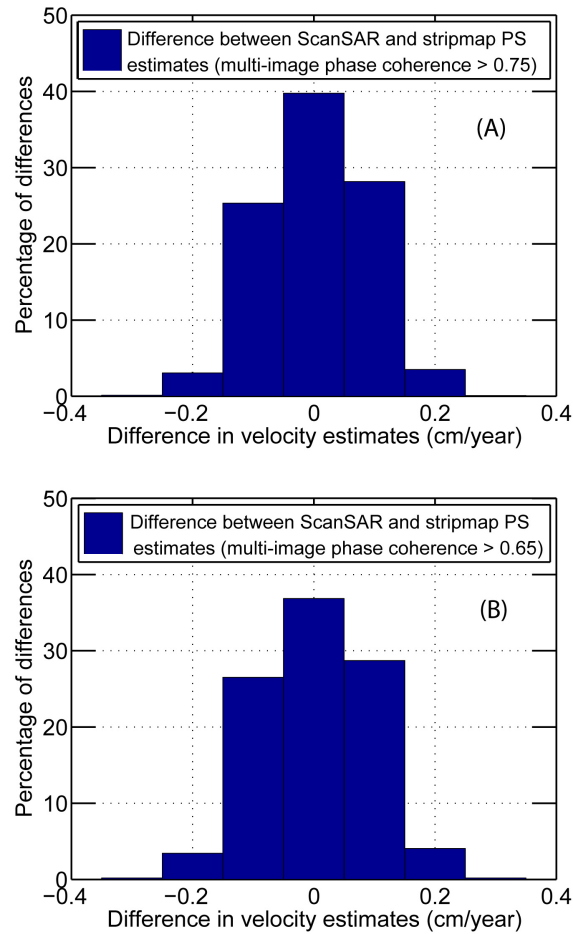


Figure 5.10: Histogram showing differences between ScanSAR and stripmap PS velocity estimates for (A) a multi-image phase coherence > 0.75 (B) a multi-image phase coherence > 0.65.

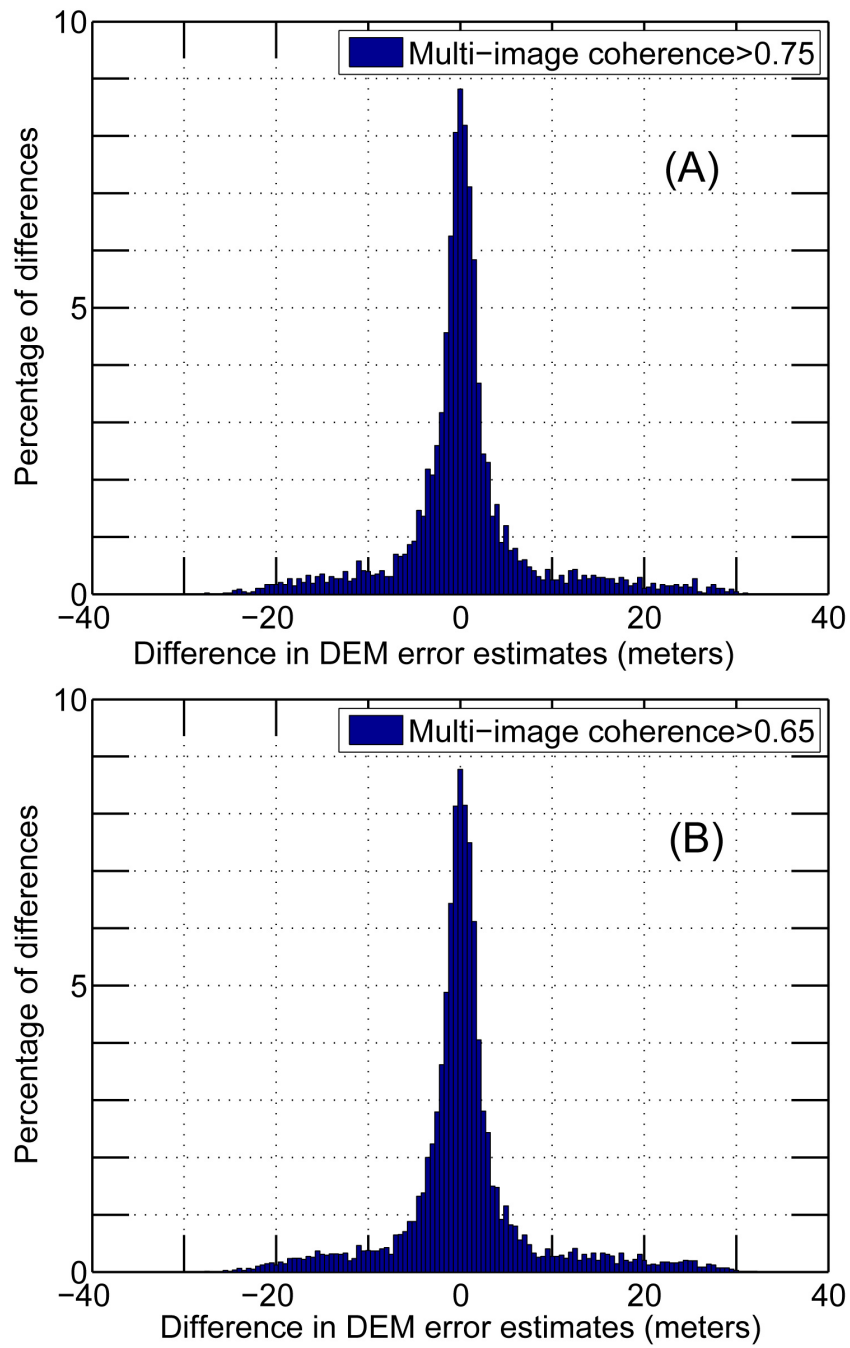


Figure 5.11: Histogram showing difference between ScanSAR and stripmap PS DEM error estimates for (A) a multi-image phase coherence  $> 0.75$  (B) a multi-image phase coherence  $> 0.65$ .



Also, in deriving the equations of the simplified two PS model, it was assumed that all PS targets present within a resolution cell are at the same slant range. In performing the ScanSAR PS analysis, this assumption might not be a limitation. But for the purpose of comparing stripmap and ScanSAR PS parameter estimates, the assumption of all PS targets being at the same slant range, is not insignificant. A PS target that is in the same slant range bin in both stripmap and ScanSAR images may have different azimuth location. In ScanSAR data, it is highly likely that the stripmap PS targets are truly at different slant ranges but within the resolution limits. Since the model considered in this study does not account for the variation in slant ranges, the phase originating from the sub-pixel location of the PS target might cause an incorrect estimation of the DEM error values. Also, to simplify the model, it has been assumed that both the targets in a ScanSAR pixel have the same velocity. If the true velocities of the two PS targets (in the same pixel) are different, then the estimated model parameters might be erroneous. The aforementioned assumptions limit the accuracy of the DEM error estimates.

However, use of a more sophisticated model does not always ensure a better accuracy of the estimated parameters. It is important that collected data should be able to support the estimation of all the modeled parameters. In other words the parameter should be sensitive to the variations in the observed data and should not be correlated to other parameters of the model. Kampes [2006] suggests that the estimation of the sub-pixel azimuth location of a PS target might be “cumbersome” using SAR data with very little Doppler centroid variations. The interferometric phase contribution caused by the PS target sub-pixel azimuth location is correlated to the difference in the Doppler centroid frequencies of the interfered SAR images. There is little variation in the Doppler centroid frequencies of data collected exclusively from either ERS-1 or ERS-2. Furthermore, there is a systematic offset between the Doppler Centroid frequencies of data collected from

ERS-1 and ERS-2. Thus, it may not be possible to estimate PS target sub-pixel azimuth location using SAR data from ERS-1 and ERS-2. ERS-2 SAR images collected after the year 2000, when problems with the yaw-steering of the satellite resulted in large variations in Doppler centroid frequencies, are more suitable for the estimation of the sub-pixel azimuth location. Kampes [2006] also notes that the estimation of the PS target sub-pixel range location is possible when the SAR images are acquired with different radar carrier wavelengths. For example, SAR data collected from Envisat and ERS-2 provide an opportunity to implement a model where the PS target sub-pixel range location can be estimated. Small difference in the radar center frequency of the two sensors enables cross-platform PS interferometry using ERS-Envisat data as discussed in Arrigoni et al. [2003].

As a final comment, it is noted that the preliminary PS estimation step has been omitted in the implementation of the multiple PS model. The multiple PS model presented in this chapter can, in theory, be modified and extended to the preliminary estimation process where pairs of PS targets are linked. However, the formulation of a new “difference multiple PS model” can be complex. Another important thing to consider in estimating difference parameters from PS target pairs is the selection of the model order, i.e. number of PS targets per ScanSAR pixel. Since the initial selection of the potential PS targets based on the amplitude dispersion index is not feasible, conceivably each ScanSAR pixel should be linked to every neighboring pixel. If a basic case of 2 PS per pixel is assumed, then the difference between neighboring pixels will require a grid search through 5 parameters, i.e. 4 differences in DEM height pairs and 1 difference in velocity. The computational requirements for a grid search of 5 or more parameters per each PS target link for possibly millions of PS links can be enormous, even for a small study area of  $5 \text{ km} \times 5 \text{ km}$ .

## 5.5 CONCLUSIONS

PSInSAR analysis of ScanSAR data has been studied. A functional model to detect multiple PS targets present within the same resolution cell was proposed as part of the study. Due to the large resolution cell size of the low resolution ScanSAR data, there is a greater chance of more than one PS target being present in the same ScanSAR resolution cell.

Contradictory to the expectations of an earlier ScanSAR PSInSAR feasibility study by Guarnieri [2000] it has been concluded that it is nearly impossible to detect PS targets based on the assumption that there is only a single dominant PS target per ScanSAR pixel. It has been shown that where the usual PS technique failed to detect any stable PS targets in ScanSAR data, the two PS model performs significantly better in detecting the PS targets. The PS density detected by the two PS model is sufficient for generating residual phase maps and atmospheric phase screens.

Results obtained from the application of the two PS model to ScanSAR data were validated using the results from stripmap PS analysis. Generally, there is a good agreement between the PS velocities estimated from the two models. The estimated velocities were reasonably accurate (standard deviation of 0.02 cm/year with respect to stripmap velocities). However, the differences between ScanSAR and stripmap DEM error estimates had large variations. The standard deviation of the DEM error differences was 7 meters with respect to stripmap DEM errors. The large variation in DEM error estimates is attributed to some of the assumptions made in the validation process of the two PS model. Small offsets in the alignment of ScanSAR and stripmap images may have resulted in an incorrect mapping of some of the stripmap PS targets into ScanSAR pixels which lead to invalid comparisons of parameter estimates. Also, slight differences in the

true slant range to the PS targets in stripmap and ScanSAR data can lead to large differences in the DEM errors estimates.

Efficient parameter search methods have to be adapted to speed up the estimation process.

## **CHAPTER SIX**

### **CONCLUSIONS AND FUTURE WORK**

This research has demonstrated that ScanSAR radar interferometry can be utilized for deformation monitoring. InSAR time series results were generated from synthesized ScanSAR data using advanced processing techniques. Burst mode data over Phoenix, Arizona were simulated from C-band ERS-1/2 SAR raw data. The bursting scheme and the simulated burst synchronization scenario mimicked the configuration of the Envisat ScanSAR Wide Swath Mode. Specifically, this research considered two InSAR time series methods: the Small Baseline Subsets (SBAS) technique and an adaptation of the Permanent Scatterer technique. The SBAS technique is suitable when the study site and the interferometric baselines are conducive for interferometry. In a more general case where the repeat-pass orbits result in large InSAR baselines and decorrelation is present, a variation of the Permanent Scatterer (PS) technique is used. To address the problem of higher decorrelation due to lower resolution of ScanSAR data compared to stripmap data, a PS model with multiple scatterers present within a resolution was proposed. The results obtained from the application of the SBAS and PS methods to simulated ScanSAR data positively support the idea of performing ScanSAR interferometry on a routine basis for the purpose of deformation monitoring.

#### **6.1 CONCLUSIONS**

##### **6.1.1 Effect of Burst Overlap on Phase Coherence**

The effect of burst overlap on the interferometric phase coherence in ScanSAR interferograms was analyzed qualitatively and quantitatively. ScanSAR

interferograms with varying burst overlap percentages were generated using burst mode data simulated from the same pair of stripmap map images. A number of study sites that vary in terms of land surface characteristics as well as in the scale and magnitude of the deformation were considered. These include (1) Phoenix Arizona – Land subsidence due to groundwater withdrawal (2) Hector mine, California,- Co-seismic deformation (3) Yellowstone, Wyoming, - Deformation due to magmatic fluid migration (4) London, U.K., - Land subsidence due to tunnel excavation, and (5) Houston, Texas – Land subsidence due to groundwater pumping. In each of the cases, profiles taken through the deformation phase maps obtained from the ScanSAR interferograms were compared to the deformation profiles taken through the stripmap formed at the same location. It is seen that in arid regions like Phoenix, Arizona and Hector Mine, California it is possible to retrieve meaningful interferometric phase with 60% burst overlap using a bursting scheme that is similar to Envisat Wide Swath mode. In urban areas that are heavily vegetated like London and Houston, performing ScanSAR interferometry can be challenging and is limited to pairs of ScanSAR images that have very good burst overlap.

#### **6.1.2 SBAS Time Series Analysis using ScanSAR Data**

The SBAS algorithm was applied to a large database of ScanSAR interferograms formed from a collection of simulated burst mode images, and a deformation time series was obtained. The deformation time series were generated for two scenarios: an ideal scenario where there was 100% burst overlap between all the ScanSAR images, and a realistic scenario where there was at least 50% burst overlap between all pairs of ScanSAR images. In both scenarios, known subsidence features in the Phoenix metropolitan area were clearly identified from the burst mode interferograms.

Phase noise of ScanSAR data relative to stripmap data was quantified using a validation process which involved the comparison of time series results obtained from ScanSAR and stripmap data. SBAS time series results generated from the original ERS-1/2 stripmap data were generated for the purpose of comparison. Difference in velocity estimates between ScanSAR and stripmap were computed at each pixel location that was coherent (i.e. pixels whose correlation is above a threshold) in both ScanSAR and stripmap data. In the case of the realistic burst overlap scenario, the difference between the ScanSAR and stripmap SBAS velocity estimates was  $0.02 \pm 0.02$  cm/year, computed over for all coherent pixels in the image. Similarly, RMS deviation between ScanSAR and stripmap displacements were calculated at each pixel location of the whole SAR image, provided the pixel was coherent. An RMS deviation of  $0.4 \pm 0.3$  cm was calculated from the differences between the ScanSAR and stripmap deformation time series. Slightly lower (better) deviations were observed for the ideal burst overlap scenario. On the whole, there was a good agreement between ScanSAR and stripmap SBAS results. The observed relative errors were within the expected deviations between low-resolution and high-resolution SAR data as reported in an earlier study by Casu et al.[ 2007]

### **6.1.3 PS Analysis using ScanSAR Data**

The feasibility of PS analysis of ScanSAR data was investigated using simulated burst mode data. ScanSAR interferograms were formed with respect to a single master reference image with a 100% burst overlap between each pair of SAR images. Interferograms were formed irrespective of the perpendicular baseline and temporal separation with respect to the reference image.

First, an adapted PS technique was applied to the database of ScanSAR interferograms. The initial step of amplitude dispersion threshold based selection of PS candidates failed to detect any potential PS targets in ScanSAR data. Residual phase maps, which contain the atmospheric noise phase and nonlinear deformation phase associated with each interferogram, could not be estimated as no PS targets were identified in the initial PS search step. Instead, residual phase maps generated from a PS analysis of stripmap data were down-sampled and utilized. The removal of the residual phase maps from the differential interferograms was an important step that adjusts the interferograms to be closer to the liberalized deformation model. The final step of pixel-by-pixel PS detection, which is based on the application of a threshold on the multi-image phase coherence, revealed very few PS targets. It was concluded that the existing PS model of one scatterer per resolution cell is not suitable for ScanSAR PS analysis. Due to the large size of a ScanSAR resolution cell, it is highly likely that there is more than one PS target per ScanSAR resolution cell.

A functional model which assumed multiple PS targets located within a single resolution cell was proposed. A two PS per pixel model was implemented, applied to ScanSAR data, and found to perform significantly better than the one PS model. The PS density of 120 PS/km<sup>2</sup> for a multi-image phase coherence threshold of 0.65 was obtained for a portion of the Phoenix metropolitan area.

Similar to the validation of SBAS results of ScanSAR data, results of ScanSAR PS analysis were compared with the results of a stripmap PS analysis. PS target velocities obtained from the single PS model analysis of stripmap data were compared with the two PS model velocity estimates obtained from ScanSAR data. The standard deviation of the difference in ScanSAR and stripmap velocities was 0.02 cm/year while the standard deviation of the difference in DEM error estimates was 7 meters. The large difference



between the DEM error estimates obtained from the stripmap and ScanSAR data are most likely due to the assumptions in the validation process of the two PS model. Small offsets in the alignment of ScanSAR and stripmap images may have resulted in an incorrect mapping of some of the stripmap PS targets into ScanSAR pixels which lead to invalid comparisons of parameter estimates. Also, slight differences in the true slant range to the PS targets in stripmap and ScanSAR data can lead to large differences in the DEM errors estimates.

## **6.2 TOPICS FOR FUTURE WORK**

### **6.2.1 Similar Studies using Synthesized ScanSAR Data from Other SAR Sensors**

Similar to this research, InSAR analyses can be performed using simulated ScanSAR data from other SAR sensors operating at different radar frequencies. ScanSAR modes are currently present on the L-band ALOS PALSAR sensor and the X-band TerraSAR-X sensor. In areas where a considerable amount of vegetation is present, InSAR analysis using L-band SAR data can be utilized to lessen the effects of decorrelation as the L-band signal tends to penetrate through foliage. On the other hand, X-band radar decorrelates much faster but is ideal where high resolution imagery is needed. For example, the ScanSAR mode on TerraSAR-X is expected to give an azimuth resolution of 16 meters.

Studies with simulated burst mode data can not only be used to indicate the feasibility of ScanSAR interferometry using SAR data collected from a particular sensor, but also can be used to determine the burst parameters needed for the design of a future ScanSAR-mode-capable mission. A detailed study should be performed considering various geographical locations and geophysical processes. For each location and process,

the radar frequency and the burst parameters that would give the ideal ScanSAR interferometry results should be evaluated.

### **6.2.2 Developing Persistent Scatterer Analysis Suitable for ScanSAR Data**

The feasibility study of the PS analysis using ScanSAR data performed as part of this research considered a pixel-by-pixel evaluation. A more rigorous multiple PS target analysis can be developed wherein relative DEM errors and relative velocities between neighboring pixels are estimated. A complete start-to-end PS analysis technique that can be performed without any a priori information should be developed. In a general PS model, any number of PS targets per resolution cell can be assumed. However, such an analysis would require estimation of numerous parameters (i.e., DEM errors or differences in DEM errors of neighboring pixels). For example, say there are  $M$  targets in one resolution cell (pixel) and  $N$  targets in a neighboring cell. Assume that all targets present within a cell have the same deformation velocity and consider the difference of the interferometric phase between the two cells. Since the two resolution cells are located close to each other, spatially-correlated noise tends to cancel out. The difference of the two resolution cells can then be modeled in terms of  $NM+1$  number of parameters, i.e.,  $NM$  number of differences between DEM heights of various targets and a difference of velocity. Computational requirements of estimating so many parameters using a simple grid search method would be enormous. To lessen the computational burden and to improve the efficiency, novel techniques of nonlinear parameter estimation should be implemented.

### **6.2.3 Using Real ScanSAR Data and Geophysical Modeling with Derived Time Series**

While most of the current and future SAR missions incorporate the ScanSAR mode, for the near-future, a large database of ScanSAR images will not be available to the scientific community. If ScanSAR data is acquired with reasonable burst overlap and with favorable baselines, ScanSAR-based InSAR techniques implemented as part of this research can be extended to real ScanSAR data.

The biggest advantage of imaging in ScanSAR mode is the shortening of the revisit time of the sensor to a particular study site. With ScanSAR mode, there can be a multi-fold increase in the amount of SAR data being acquired over a study site compared to the amount of data acquired using the stripmap mode over the same duration. It is important to note that although the sensor revisit time in ScanSAR mode is much shorter than a repeat orbit cycle period, the use of ScanSAR mode does not allow for the formation of interferograms with a time span shorter than one repeat orbit cycle. ScanSAR or burst mode data collected from each track or subswath can be used to generate an independent time series result. Multiple deformation time series results, each corresponding to a different satellite track, can be obtained wherein the time series of different tracks are staggered in time with respect to each other. The multitude of time series information can be assimilated into geophysical models that can relate the surface deformation to the underlying geophysical processes.

Alternatively, time series results from different tracks can be combined with each other by making certain assumptions about the observed deformation phenomenon. Since InSAR measures the radar line-of-sight component of the deformation, variations in the look angles of the different tracks imply that each track will measure a different component of the deformation. If it can be assumed that the observed deformation is

entirely vertical, for example, then the line-of-sight components can be converted into vertical deformations using the look angle information.

Denser sampling of SAR images available through ScanSAR mode also can be used to detect specific events such as a sudden onset of a new deformation phenomenon that would otherwise be missed due to the longer revisit periods of the stripmap mode. For example, the lag between a significant event, such as a major rainfall event or a rapid fluid withdrawal from a reservoir, and its impact to the ongoing deformation can be determined more accurately.

## APPENDIX A

### Chirp-Z Transform

Here, an explanation of the CZT is given starting from the definition of the z-transform. The z-transform of a discrete time series  $x(n)$ , for  $n = 0, N-1$ , can be expressed as [Oppenheim et al., 1999]:

$$ZT[x(n)] = X(z) = \sum_{n=0}^{N-1} x(n)z^{-n} \quad (\text{A.1})$$

where  $z$  is a complex variable with an amplitude  $A$  and phase  $\phi$ :

$$z = A \exp\{j\phi\} \quad (\text{A.2})$$

A special case of the z-transform where  $A=1$  and  $\phi = 2\pi k/N$  gives the  $k^{th}$  sample of the Discrete Fourier Transform (DFT). The DFT is a weighted summation of  $N$  equiangular-spaced complex numbers on the unit circle in the complex plane [Rabiner et al., 1969].

$$DFT_{x(n)}[k] = \sum_{n=0}^{N-1} x(n) \exp\left\{-j \frac{2\pi}{N} kn\right\}, \quad k = 0, N-1 \quad (\text{A.3})$$

A more general form of the z-transform can be written where the weighed summation contains any arbitrary number of equiangular-spaced complex numbers located on the unit circle in the complex plane. If  $M$  (need not be equal to  $N$ ) complex numbers that are

equiangular-spaced on the unit circle ( $A=1$ ) are considered, then the z-transform can be written as:

$$X(k) = \sum_{n=0}^{M-1} x(n) \exp\{-j(\Delta\phi)kn\} \quad k = 0, N-1 \quad (\text{A.4})$$

where  $\Delta\phi$  is the constant angular spacing between the complex numbers. This general form of z-transform, although flexible, is not very efficient to compute. To speed up the computation of the z-transform, a trick substitution can be used [Bluestein, 1968]. The substitution is  $nk = (n^2 + k^2 - (n-k)^2)/2$ . The concept of CZT uses this substitution with an aim to utilize the efficiency available through the FFT algorithms. After the substitution, Equation A.4 can be written in terms of “chirp” scaling kernels as:

$$CZT_{x(n)}[k] = \sum_{n=0}^{M-1} x(n) \exp\left\{-j\Delta\phi \frac{k^2}{2}\right\} \exp\left\{-j\Delta\phi \frac{n^2}{2}\right\} \exp\left\{j\Delta\phi \frac{(k-n)^2}{2}\right\},$$

$$k = 0, N-1 \quad (\text{A.5})$$

In the above equation, the last three terms inside the summation are called the “chirp” scaling kernel terms because their phase varies in a quadratic fashion [Rabiner et al., 1969]. Further, Equation A.5 can be re-arranged to show that CZT can be broken down into three steps.

$$CZT_{x(n)}[k] = \exp\left\{-j\Delta\phi \frac{k^2}{2}\right\} \left[ \sum_{n=0}^{M-1} \left[ x(n) \exp\left\{-j\Delta\phi \frac{n^2}{2}\right\} \right] \exp\left\{j\Delta\phi \frac{(k-n)^2}{2}\right\} \right]$$

$$k = 0, N-1 \quad (\text{A.6})$$

The first step of CZT is the multiplication of the data signal ( $x$ ) with the “chirp” scaling kernel term  $\left(\exp\{-j\Delta\phi n^2/2\}\right)$ . This operation is the computation of the first bracketed term inside the summation shown in Equation A.6. The second step is the calculation of the summation itself, which is a convolution operation between the result from the first step and the conjugate of the scaling kernel. The convolution operation can be efficiently performed using the FFT algorithms. Note that to avoid circular convolution effects, the signal data and the chirp term, both have to be extended to a length of at least  $2N_B - 1$ . The last step of CZT, involves the multiplication of the resultant of the second step with the “chirp” phase compensation term which is outside the summation shown in Equation A.6.

This concludes the explanation of the CZT.

## APPENDIX B

### List of SAR Data and Interferograms Used

Table B.1: SAR images used for SBAS and PS InSAR time series techniques.

Scene Number	Date (YYYYMMDD)	Sensor	Doppler Centroid (Hz)	Scene Number	Date (YYYYMMDD)	Sensor	Doppler Centroid (Hz)
1	19920710	ERS1	357	23	19961230 (*)	ERS2	86
2	19920814	ERS1	296	24	19970310	ERS2	147
3	19920918	ERS1	337	25	19970519	ERS2	83
4	19921023	ERS1	339	26	19971215	ERS2	130
5	19930205	ERS1	276	27	19980223	ERS2	64
6	19930521	ERS1	373	28	19980330	ERS2	96
7	19930903	ERS1	308	29	19980504	ERS2	98
8	19931008	ERS1	332	30	19980608	ERS2	106
9	19931217	ERS1	314	31	19980713	ERS2	60
10	19950514	ERS1	402	32	19981130	ERS2	57
11	19950827	ERS1	386	33	19990315	ERS2	157
12	19951105	ERS1	307	34	19990524	ERS2	143
13	19951106	ERS2	30	35	19990628	ERS2	86
14	19951210	ERS1	343	36	19990802	ERS2	68
15	19951211	ERS2	81	37	19991220	ERS2	145
16	19960218	ERS1	316	38	20000508	ERS2	-83
17	19960219	ERS2	60	39	20000717	ERS2	-164
18	19960428	ERS1	329	40	20000925 (#)	ERS2	-116
19	19960603	ERS2	56	41	20001030	ERS2	229
20	19960812	ERS2	25	* Reference image			
21	19960916	ERS2	0	# Image not used in SBAS Analysis			
22	19961021	ERS2	28				



Table B.2: Interferograms formed as part of the SBAS time series analysis.

Scene Number	Interferogram Image Dates (YYYYMMDD)		Temporal baseline (days)	Perpendicular baseline (m)	Burst synchronization in variable burst overlap scenario (%)
	Reference	Secondary			
1	19920710	19930521	315	22	85
2	19920710	19931008	455	-75	97
3	19920710	19950827	1143	-85	78
4	19920814	19930205	175	-22	100
5	19920814	19950514	1003	77	88
6	19920814	19960603	1389	29	93
7	19920918	19951106	1144	-72	83
8	19920918	19951210	1178	70	72
9	19920918	19951211	1179	-120	98
10	19921023	19960812	1389	106	95
11	19930205	19950514	828	98	88
12	19930205	19960603	1214	51	93
13	19930521	19931008	140	-97	82
14	19930521	19950827	828	-107	63
15	19930521	19960916	1214	-4	68
16	19930521	19961230	1319	68	75
17	19930521	19970310	1389	122	63
18	19930521	19970519	1459	30	98
19	19930903	19961230	1214	-94	78
20	19930903	19970310	1284	-40	67
21	19931008	19950827	688	-11	82
22	19931008	19960812	1039	-42	93
23	19931008	19960916	1074	93	87
24	19931008	19970519	1319	127	83
25	19931217	19960218	793	-69	78
26	19931217	19960219	794	-18	80
27	19931217	19960428	863	65	77
28	19931217	19961021	1039	-104	85
29	19950514	19960603	386	-48	82
30	19950514	19980223	1016	-17	92

<b>Scene Number</b>	<b>Interferogram Image Dates (YYYYMMDD)</b>	<b>Temporal baseline (days)</b>	<b>Perpendicular baseline (m)</b>	<b>Burst synchronization in variable burst overlap scenario (%)</b>
31	19950514 19980713	1156	74	100
32	19950827 19960812	351	-32	88
33	19950827 19960916	386	103	95
34	19950827 19980330	946	51	95
35	19950827 19981130	1191	88	97
36	19950827 19990802	1436	104	75
37	19951105 19951210	35	-64	97
38	19951105 19961021	351	104	68
39	19951105 19980608	946	129	95
40	19951106 19951211	35	-47	82
41	19951106 19980504	910	13	90
42	19951106 19990628	1330	-67	88
43	19951210 19980504	876	-130	98
44	19951211 19980504	875	60	72
45	19951211 19990524	1260	-126	65
46	19951211 19990628	1295	-20	70
47	19960218 19960219	1	51	98
48	19960218 19961021	246	-35	63
49	19960218 19980608	841	-9	90
50	19960219 19960428	69	83	97
51	19960219 19961021	245	-86	65
52	19960219 19980608	840	-60	92
53	19960603 19980223	630	31	90
54	19960603 19980713	770	122	82
55	19960812 19971215	490	-101	73
56	19960812 19980330	595	83	83
57	19960812 19981130	840	121	92
58	19960916 19961230	105	72	93
59	19960916 19970310	175	126	95
60	19960916 19970519	245	34	70

<b>Scene Number</b>	<b>Interferogram Image Dates (YYYYMMDD)</b>	<b>Temporal baseline (days)</b>	<b>Perpendicular baseline (m)</b>	<b>Burst synchronization in variable burst overlap scenario (%)</b>
61	19960916 19980330	560	-53	90
62	19960916 19981130	805	-15	98
63	19960916 19990802	1050	0	80
64	19960916 19991220	1190	55	100
65	19961021 19980608	595	25	73
66	19961021 20000508	1295	38	70
67	19961230 19970310	70	54	88
68	19961230 19970519	140	-38	77
69	19961230 19980330	455	-124	83
70	19961230 19981130	700	-87	92
71	19961230 19990315	805	125	92
72	19961230 19990802	945	-71	87
73	19961230 19991220	1085	-17	93
74	19961230 20001030	1400	51	97
75	19970310 19970519	70	-92	65
76	19970310 19990315	735	71	80
77	19970310 19990524	805	118	97
78	19970310 19990802	875	-125	75
79	19970310 19991220	1015	-71	95
80	19970310 20001030	1330	-3	85
81	19970519 19980330	315	-87	60
82	19970519 19981130	560	-49	68
83	19970519 19990802	805	-33	90
84	19970519 19991220	945	21	70
85	19970519 20001030	1260	89	80
86	19971215 20000717	945	-128	73
87	19980223 19980713	140	91	92
88	19980330 19981130	245	37	92
89	19980330 19990802	490	53	70
90	19980330 19991220	630	108	90

<b>Scene Number</b>	<b>Interferogram Image Dates (YYYYMMDD)</b>	<b>Temporal baseline (days)</b>	<b>Perpendicular baseline (m)</b>	<b>Burst synchronization in variable burst overlap scenario (%)</b>
91	19980504 19990628	420	-80	98
92	19980608 20000508	700	12	97
93	19981130 19990802	245	16	78
94	19981130 19991220	385	70	98
95	19990315 19990524	70	47	77
96	19990315 20001030	595	-74	95
97	19990524 19990628	35	106	95
98	19990524 20001030	525	-121	82
99	19990802 19991220	140	54	80
100	19990802 20001030	455	122	90
101	19991220 20001030	315	68	90

## REFERENCES

- Adam, N., B. Kampes, M. Eineder, J. Worawattanamateekul, and M. Kircher, The development of a scientific permanent scatterer system, *Proc. of ISPRS Hannover Workshop*, Hannover, Germany, October 2003.
- Amelung, F., D. L. Galloway, J. W. Bell, H. A. Zebker, and R. J. Laczniaik, Sensing the ups and downs on Las Vegas: InSAR reveals structural control of land subsidence an aquifer-system deformation, *Geology*, 27(6), 483-486, 1999.
- Arrigoni, M., C. Colesanti, A. Ferretti, D. Perissin, C. Prati, and F. Rocca, Identification of the location phase screen of ERS-ENVISAT permanent scatterers, *Third International Workshop on ERS SAR Interferometry FRINGE03*, 1-3, Frascati, Italy, December 2003.
- Bamler, R., Doppler Frequency Estimation and the Cramér-Rao Bound, *IEEE Trans. Geosci. Remote Sens.*, 29(3), 385-390, 1991.
- Bamler R., Optimum Look Weighting for Burst-Mode and ScanSAR Processing, *IEEE Trans. Geosci., Remote Sens.*, 33(3), 722-725, 1995.
- Bamler R., and M. Eineder., ScanSAR Processing Using Standard High Precision SAR Algorithms, *IEEE Trans. Geosci. Remote Sens.*, 34(1), 1996.
- Bamler R., D. Geudtner, B. Schattler, P.W. Vachon, U. Steinbrecher, J. Holzner, J. Mittermayer, H. Breit, and A. Moreira, RADARSAT ScanSAR Interferometry, *Proc. International Geosci. Remote Sens. Symposium*, vol. 3, 1517-1521, Hamburg, Germany, 1999.
- Berardino, P., G. Fornaro, R. Lanari, and E. Sansoti, A new algorithm for surface deformation monitoring based on small baseline differential SAR interferograms, *IEEE Trans. Geosci. Remote Sens.*, 40(11), 2375-2383, 2002.
- Bluestein, L. I., A linear filtering approach to the computation of the discrete Fourier transform, *Northeast Electronics Research and Engineering Meeting Record 10*, 218-219, 1968.
- Buckley, S. M., *Radar Interferometry Measurements of Land Subsidence*, Ph.D. Dissertation, The University of Texas at Austin, 2000.

- Caputi, W. J., Stretch: A Time-Transformation Technique, *IEEE Trans. Aerospace and Electronic Systems*, AES-7, 269-278, 1971.
- Casu, F., M. Manzo, and R. Lanari, A quantitative assessment of the SBAS algorithm performance for surface deformation retrieval from DInSAR data, *Remote Sens. Environment.*, 102(3-4), 195-210, 2006.
- Casu, F., M. Manzo, A. Pepe, G. Mazzarella, and R. Lanari, On the capability of the SBAS-DInSAR Technique to investigate deformation phenomena of large areas with low resolution data, *Proc. Envisat Symposium 2007*, ESA SP-636, Montreux, Switzerland, April 2007.
- Chang, C. Y., M. Y. Jin, Y.L. Lou, and B. Holt, First SIR-C ScanSAR Results, *IEEE Trans. Geosci. Remote Sens.*, 34(5), 1278-1281, 1996.
- Chen, C. W., and H. A. Zebker, Network approaches to two-dimensional phase unwrapping: intractability and two new algorithms, *J. Opt. Society America A*, 17(3), 401-414, 2000.
- Constantini, M., A Phase Unwrapping Method Based on Network Programming, *FRINGE'96 Workshop on ERS SAR Interferometry*, Zürich, Switzerland, September-October, 1996.
- Constantini, M., A Novel Phase Unwrapping Method Based on Network Programming, *IEEE Trans. Geosci. Remote Sens.*, 36(3), 813-821, 1998.
- Colesanti, C., A. Ferretti, C. Prati, and F. Rocca, Monitoring landslides and tectonic motions with the permanent scatterers technique, *Engg. Geology*, 68(1-2), 3-14, 2003a.
- Colesanti, C., A. Ferretti, F. Novali, C. Prati, and F. Rocca, SAR monitoring of progressive and seasonal ground deformation using the Permanent Scatterer Technique, *IEEE Trans. Geosci. Remote Sens.*, 41(7), 1685-1701, 2003b.
- Cumming, I. G., and J. Lim, *The Design of a Digital Breadboard Processor for the ESA Remote Sensing Satellite Synthetic Aperture Radar*, Technical report, MacDonald Dettwiler, Richmond, BC, 1981.
- Cumming, I. G., and F. H. Wong, *Digital Processing of Synthetic Aperture Radar Data: Algorithms and Implementation*, Arctech House Inc., Norwood, Massachusetts, 2005.
- Curlander, J. C., and R. N. McDonough, *Synthetic Aperture Radar: Systems and Signal Processing*, Wiley, New York, 1991.

- Desnos, Y. L., C. Buck, J. Guijarra, J. L. Suchail, R. Torres, and E. Attema, ASAR – Envisat’s Advanced Synthetic Aperture Radar: Building on ERS Achievements towards Future Earth Watch Missions, *ESA Bulletin*, 102, 91-101, 2000.
- Deutsch, C. V., and A. G. Journel, *GSLIB: Geostatistical Software Library and user’s guide*, Oxford University Press, New York, 1997.
- Farr, T. G., P. A. Rosen, E. Caro, R. Crippen, R. Duren, S. Hensley, M. Kobrick, M. Paller, E. Rodriguez, L. Roth, D. Seal, S. Shaffer, J. Shimada, J. Umland, M. Werner, M. Oskin, D. Burbank, and D. Alsdorf, The Shuttle Radar Topography Mission, *Reviews of Geophy.*, 45, RG2004, 2007.
- Ferretti, A., C. Prati, and F. Rocca, Nonlinear subsidence rate estimation using permanent scatterers in differential SAR interferometry, *IEEE Trans. Geosci. Remote Sens.*, 38(5), 2202-2212, 2000.
- Ferretti, A., C. Prati, and F. Rocca, Permanent Scatterers in SAR Interferometry, *IEEE Trans. Geosci. Remote Sens.*, 39(1), 8-20, 2001.
- Ferretti, A., M. Bianchi, C. Prati, and F. Rocca, Higher-Order Permanent Scatterers Analysis, *EURASIP Journal on Applied Signal Processing*, 2005(20), 3231-3242, 2005.
- Flynn, T. J., Two-dimensional phase unwrapping with minimum weighted discontinuity, *J. Opt. Society America A*, 14, 2692-2701, 1997.
- Galloway, D., K. Hudnut, S. Ingebritsen, S. Phillips, G. Peltzer, F. Rogez, and P. Rosen, Detection of aquifer system compaction and land subsidence using interferometric synthetic aperture radar, Antelope Valley, Mojave Desert, California, *Water Resources Research*, 34(10), 2573-2586, 1998.
- Gabriel, A. K., R. M. Goldstein, and H. A. Zebker, Mapping Small Elevation Changes Over Large Areas: Differential Radar Interferometry, *J. Geophys. Res.*, 94(B7), 9138-9191, 1989.
- Gatelli F., A. M. Guarnieri, F. Parizzi, P. Pasquali, C. Prati, and F. Rocca, The Wavenumber Shift in SAR Interferometry, *IEEE Trans. Geosci. Remote Sens.*, 32(4), 855-865, 1994.
- Ghiglia, D. C., and M. D. Pritt, *Two-dimensional phase unwrapping: theory, algorithms, and software*, John Wiley and Sons, Inc., New York, 1998.
- Goldstein, R. M., H. Engelhardt, B. Kamb, and R. M. Frolich, Satellite Radar Interferometry for Monitoring Ice Sheet Motion: Application to an Antarctic Ice Stream, *Science*, 262(5139), 1525-1530, 1993.

- Goldstein, R. M., H. A. Zebker, and C. L. Werner, Satellite radar interferometry: Two-dimensional phase unwrapping, *Radio Science*, 23(4), 713-720, 1988.
- Goldstein, R. M., and C. L. Werner, Radar Interferogram Filtering for Geophysical Applications, *Geophys. Res. Letters*, 25(21), 4035-4038, 1998.
- Guarnieri A. M., C. Prati, and F. Rocca, Interferometry with ScanSAR, *Proc. International Geosci. Remote Sens. Symposium*, vol. 1, 550-552, Firenze, Italy, July, 1995.
- Guarnieri, A. M., and C. Prati, ScanSAR Focusing and Interferometry, *IEEE Trans. Geosci. Remote Sens.*, 34(4), 1029-1038, 1996.
- Guarnieri, A. M., ScanSAR interferometric monitoring using the PS technique, *Proc. ERS/ENVISAT Symposium*, Gothenburg, Sweden, October 2000.
- Guarnieri, A. M., P. Guccione, P. Pasquali, and Y. L. Desnos, Multi-mode ENVISAT ASAR interferometry: techniques and preliminary results, *IEEE Proc. Radar, Sonar, and Navigation*, 150(3), 193-200, 2003.
- Guccione P., Interferometry with ENVISAT Wide Swath ScanSAR Data, *IEEE Geosci. Remote Sens. Letters*, 3(3), 377-381, 2006
- Gudipati. K., S. M. Buckley, and C. R. Wilson, Temporal Variations in Phoenix Arizona Subsidence Revealed by Radar Interferometry, Poster, *IEEE International Geosci. Remote Sens. Symposium*, Anchorage, Alaska, September 2004.
- Hanssen, R. F., *Radar Interferometry: Data Interpretation and Error Analysis*, Kluwer Academic Publishers, Dordrecht, The Netherlands, 2001.
- Holzner J., and R. Bamler, Burst-Mode and ScanSAR Interferometry, *IEEE Trans. Geosci. Remote Sens.*, 40(9), 1917-1934, 2002.
- Honeycutt, B. L., Spaceborne Imaging Radar-C Instrument, *IEEE Trans. Geosci. Remote Sens.*, 27(2), 164-169, 1989.
- Hooper, A, H. A. Zebker, P. Seagall, and B. Kampes, A New Method for Measuring Deformation on Volcanoes and Other Natural Terrains Using InSAR Persistent Scatterers, *Geophys. Res. Letters*, 31, L23611, 2004.
- Johnson, W. T. K., Magellan Imaging Radar Mission to Venus, *Proc. of IEEE*, 79(6), 777-790, 1991.
- Kampes, B. M., *Radar Interferometry: Persistent Scatterer Technique*, Springer, Dordrecht, The Netherlands, 2006.



- Lanari, R., S. Hensley, and P. Rosen, Modified SPECAN algorithm for ScanSAR Data Processing, *Proc. of International Geosci. Remote Sens. Symposium*, vol. 2, 636-638, Seattle, Washington, July 1998.
- Lanari, R., O. Mora, M. Manunta, J. J. Mallorqui, P. Berardino, E. Sansosti, A small-baseline approach for investigating deformations on full-resolution differential SAR interferograms, *IEEE Trans. Geosci. Remote Sens.*, 42(7), 1377-1386, 2004.
- Leung, K., M. Jin, C. Wong, and J Gilbert, SAR Data Processing for the Magellan Prime Mission, *Proc. International Geosci. Remote Sens. Symposium*, 606-609, Clear Lake, Texas, May 1992.
- Leung, K., M. Chen, J. Shimada, and A. Chu, RADARSAT Processing System at ASF, *Proc. International Geosci. Remote Sens. Symposium*, vol. 1, 43-47, Lincoln, Nebraska, July 1996.
- Li, F. K., and R. M. Goldstein, Studies of Multibaseline Spaceborne Interferometric Synthetic Aperture Radars, *Proc. of International Geosci. Remote Sens. Symposium*, 1545-1550, Ann Arbor, Michigan, May 1987.
- Li, F. K., and R. M. Goldstein, Studies of Multibaseline Spaceborne Interferometric Synthetic Aperture Radars, *IEEE Trans. Geosci. Remote Sens.*, 28(1), 88-97, 1990.
- Massonnet, D., M. Rossi, C. Carmona, F. Adragna, G. Peltzer, K. Feigl, and T. Rabaute, The Displacement Field of Landers Earthquake Mapped by Radar Interferometry, *Nature*, 364, 138-142, July 8, 1993.
- Massonnet, D., P. Briole, and A. Arnaud, Deflation of Mount Etna Monitored by Spaceborne Radar Interferometry, *Nature*, 375, 567-570, June 15, 1995.
- Massonnet, D., and K. Feigl, Radar interferometry and its application to changes in the Earth's surface, *Reviews of Geophy.*, 36(4), 441-500, 1998.
- Mora, O., J. J. Mallorqui, and A. Broquetas, Linear and Nonlinear Terrain Deformation Maps From a Reduced Set of Interferometric SAR Images, *IEEE Trans. Geosci. Remote Sens.*, 41(10), 2243-2253, 2003.
- Moore, R. K., J. P. Claassen, and Y. H. Lin, Scanning Spaceborne Synthetic Aperture Radar with Integrated Radiometer, *IEEE Trans. Aerospace and Electronic Systems*, AES-17, 410-421, 1981.
- Moreira, A., J. Mittermayer, and R. Scheiber, Extended chirp scaling algorithm for air and spaceborne SAR data processing in stripmap and ScanSAR imaging modes, *IEEE Trans. Geosci. Remote Sens.*, 34(5), 1123-1136, 1996.

- Oppenheim, A. V., R. W. Schaffer, and J. R. Buck, *Discrete-Time Signal Processing*, 2<sup>nd</sup> edition, Prentice-Hall, Upper Saddle River, New Jersey, 1999.
- Ortiz, A. B., and H. A. Zebker, ScanSAR-to-Stripmap Mode Interferometry Processing Using ENVISAT/ASAR Data, *IEEE Trans. Geosci. Remote Sens.*, 45(11), 2007.
- Paige, C. C., and M. A. Saunders, LSQR: An Algorithm for Sparse Linear Equations and Sparse Least Squares, *ACM Trans. Mathematical Software*, 8(1), 43-71, 1982.
- Pritt, M. D., Congruence in least-squares phase unwrapping, *Proc. International Geosci. Remote Sens. Symposium*, vol. 2, 875-877, Ontario, Canada, August 1997.
- Raney, R. K., A. P. Luscombe, E. J. Langham, and S. Ahmed, RADARSAT, *Proc. of the IEEE*, 79(6), 839-849, 1991.
- Rabiner, L., R. Schaffer, and C. Rader, The Chirp Z-transform Algorithm and Its Applications, *The Bell Systems Technical Journal*, 48(5), 1249-1291, 1969.
- Rosich B., A. M. Guarnieri, D. D'Aria, I. Navas, B. Duesmann, C. Cafforio, P. Guccione, S. Vazzana, O. Barois, O. Colin, and E. Mathot, ASAR Wide Swath Interferometry: Optimisation of the Scan Pattern Synchronization, *Proc. Envisat Symposium 2007*, ESA SP-636, 593602, Montreux, Switzerland, April 2007.
- Schmidt, D. A., and R. Bürgmann, Time dependent land uplift and subsidence in Santo Claravalley, CA, from a large interferometric synthetic aperture radar data set, *J. Geophys. Res.*, 108(B9), ETG 4-1 – ETG 4-13, 2003.
- Stoica, P., and R. L. Moses, *Introduction to Spectral Analysis*, Prentice-Hall, Upper Saddle River, New Jersey, 1997.
- Tomiyasu, K., Conceptual Performance of a Satellite Borne, Wide Swath Synthetic Aperture Radar, *IEEE Trans. Geosci. Remote Sens.*, 19(2), 108-116, 1981.
- Usai, S., *A new approach for long term monitoring of deformations by differential SAR interferometry*, PhD Dissertation, Delft University, The Netherlands, 2001.
- Werner, C., U. Wegmuller, T. Strozzi, and A. Wiesmann, Interferometric point target analysis for deformation mapping, *Proc. International Geosci. Remote Sens. Symposium*, vol. 7, 4362-4364, July 2003.
- Wiesmann, A., C. Werner, M. Santoro, U. Wegmuller, and T. Strozzi, ScanSAR Interferometry for Land Use Applications and Terrain Deformation, *Proc. International Geosci. Remote Sens. Symposium*, 3103-3106, 2006.
- Zebker, H. A., and J. Villasenor, Decorrelation in Interferometric Radar Echoes, *IEEE Trans. Geosci. Remote Sens.*, 30(5), 950-959, 1992.

- Zebker, H. A., P. A. Rosen, R. M. Goldstein, A. K. Gabriel, and C. L. Werner, On the derivation of coseismic displacement fields using differential radar interferometry: The Landers earthquake, *J. Geophys. Res.*, 99(B10), 19,617-19,634, 1994.
- Zebker, H. A., P. A. Rosen, S. Hensley, and P. J. Mouginis-Mark, Analysis of active lava flows on Kilauea volcano, Hawaii, using SIR-C radar correlation measurements, *Geology*, 24, 495-498, 1996.
- Zebker, H. A., P. A. Rosen, and S. Hensley, Atmospheric effects in interferometric synthetic aperture radar surface deformation and topographic maps, *J. Geophys. Res.*, 102(B4), 7547-7563, 1997.
- Zebker, H. P. Shankar, and A. Hooper, InSAR Remote Sensing over Decorrelating Terrains: Persistent Scattering Methods, *IEEE Radar Conference 2007*, 717-722, Boston, MA, 2007.
- Ziemer, R. E., and W. H. Tranter, *Principles of Communications: Systems, Modulation, and Noise*, Wiley, New York, 1995.

## **VITA**

Krishna Vikas Gudipati was born to Shantaram Gudipati and Nagasree Gudipati on November 08, 1979, in Hyderabad, India. He received a Bachelor of Technology degree in civil engineering from the Indian Institute of Technology Bombay. He started his graduate studies in the Department of Geological Sciences at the University of Texas at Austin in July, 2001. He was awarded a Master of Science degree in geological sciences from the University of Texas at Austin in December 2003.

Permanent address: H.No. 12-13-174, Siddhartha Nagar, Tarnaka,  
Hyderabad, Andhra Pradesh, India 500017

This dissertation was typed by Krishna Vikas Gudipati.